COUPLED MODELLING OF TURBIDITY CURRENTS OVER ERODIBLE BEDS

Peng Hu

Submitted for the degree of Doctor of Philosophy

Heriot-Watt University

School of the Built Environment

May 2012

ABSTRACT

Turbidity currents are significant due to their role in dictating reservoir sedimentation, the safety of deep sea facilities and the formation of submarine morphological features and turbidites. Interactions exist between turbidity current, sediment transport, bed topography and deformation. However, existing mathematical models have ignored these interactions either partly or completely. Therefore these models can be referred to as decoupled or partially coupled models. Uncertainties arising from these simplifications remain unclear. To help address this, the present study advances modelling capability and understanding of turbidity currents in three areas. First, the significance of the interactions is analysed theoretically. Second, a fully coupled mathematical model, which incorporates explicitly the interactions between turbidity current, sediment transport, bed topography and deformation, is developed and tested. Third, the model is applied to submarine turbidity currents and reservoir turbidity currents. It is demonstrated that the model is a viable tool for effective reservoir sediment management and facilitates an improved understanding of the formation of submarine morphological features.

Three issues need to be carefully dealt with in turbidity current modelling: 1) the internal hydraulic jumps, 2) the moving current front, -and 3) the irregular topographies in the field. These necessitate a mathematical model being well-balanced and capable of automatically capturing shock waves and tracking the wet/dry front. But to the writer's knowledge, these aspects have so far not been simultaneously implemented in existing models of turbidity currents. In this study, the finite volume method is used to solve the governing equations and the slope limited centred scheme (SLIC) is employed to estimate the numerical fluxes, rendering the model capable of automatically capturing shock waves. The weighted surface depth gradient method (WSDGM) is implemented in the SLIC scheme, making the model well-balanced and thus applicable to both regular and irregular topographies. The well-balanced property is demonstrated by successful reproduction of an initially subaqueous static turbidity volume over an irregular hump, as well as the successful application of the model to a real reservoir. The experimentally observed internal hydraulic jump is satisfactorily reproduced by the model, suggesting the ability of the model to accurately capture shock-waves. The accuracy of the model in reproducing key current variables is also demonstrated as against experimental data.

The significance of fully coupled modelling is investigated theoretically using the multiple-time-scale theory. This is complemented by numerical simulations of self-accelerating turbidity currents. Fully coupled modelling is shown to be critical for refined quality of turbidity current modelling, especially for those cases featuring rapid bed deformation. Decoupled and partially coupled models may be approximately applicable only to turbidity currents with mild bed deformation.

Existing understanding of the formation of submarine morphological features is based mainly on indirect back-estimations, which cannot resolve the physical process. Applying the fully coupled model, the formation processes of canyons, channel-levees and lobes are numerically resolved. It is demonstrated that appropriate bed slope and sediment particle size may favour the formation of channel-levee morphology over submarine fans, as larger Richardson number does.

Turbidity currents have been generated in a series of water-sediment regulation experiments in the Yellow River, China, aiming to get as much sediment as possible transported to the downstream and therefore reduce reservoir sedimentation. However, post-experiment analyses are mainly in the form of observed data comparisons. Two events of turbidity currents in the Xiaolangdi reservoir are investigated numerically. The advance of the current front and the sediment transport rate are reproduced by the model fairly well. These suggest the present model as a viable tool for determining the timing for operating the bottom outlets, which is critical for effective reservoir sediment management.

ACKNOWLEDGEMENT

First of all, I would like to express my deepest gratitude to my supervisors, Prof. Zhixian Cao and Prof. Gareth Pender, for their contributions to this thesis as well as their expert guidance and continuous supports throughout this research.

I am very proud to be one of the winners of UK Overseas Research Students Awards Scheme (ORSAS) and James Watt Scholarship from Heriot-Watt University, which provide funding to support my study in the last three years. Also thanks go to National Science Foundation of China (Grant No. 10672126), and the Doctoral Program Foundation, Ministry of Education, China (Grant No. 20060486015), which were contracted to Prof. Cao.

I thank all my friends and colleagues from both Heriot-Watt University and Wuhan University, who all give me great help and support during the period of my study.

Finally, I am deeply grateful to my parents and girlfriend Wei Li, for their patience, love and encouragement.

ACADEMIC REGISTRY
RESEARCH THESIS SUBMISSION

Name*:*	PENG HU		
School/PGI:	School of the Built Environment		
Version: *(i.e. First, Resubmission, Final)*	Final	Degree Sought (Award **and** Subject area)	PhD, Civil Engineering

Declaration

In accordance with the appropriate regulations I hereby submit my thesis and I declare that:

1) the thesis embodies the results of my own work and has been composed by myself
2) where appropriate, I have made acknowledgement of the work of others and have made reference to work carried out in collaboration with other persons
3) the thesis is the correct version of the thesis for submission and is the same version as any electronic versions submitted*.
4) my thesis for the award referred to, deposited in the Heriot-Watt University Library, should be made available for loan or photocopying and be available via the Institutional Repository, subject to such conditions as the Librarian may require
5) I understand that as a student of the University I am required to abide by the Regulations of the University and to conform to its discipline.

* *Please note that it is the responsibility of the candidate to ensure that the correct version of the thesis is submitted.*

Signature of Candidate*:*		Date:	8 May 2012

Submission

Submitted By *(name in capitals):*	PENG HU
Signature of Individual Submitting:	
Date Submitted:	8 May 2012

For Completion in the Student Service Centre (SSC)

Received in the SSC by *(name in capitals):*			
Method of Submission *(Handed in to SSC; posted through internal/external mail):*			
*E-thesis Submitted (**mandatory for final theses)***			
Signature:		Date:	

CONTENT

LIST OF TABLES

LIST OF FIGURES

GLOSSARY

FCM Fully coupled model, in which the interactions between the turbidity current, sediment transport and bed topography are explicitly accounted for

PCM Partially coupled model, which differs from the FCM in that the feedback impacts of bed deformation are ignored

TEM Three equation model developed by Fukushima *et al*. (1985) and Parker *et al*. (1986)

FCMK A model based on the FCM, yet the bed drag coefficient is linked to a turbulent energy constraint proposed by Parker *et al*. (1986)

PCMK A model based on the FCM, yet the bed drag coefficient is linked to a turbulent energy constraint proposed by Parker *et al*. (1986)

FEM Four equation model developed by Fukushima *et al*. (1985) and Parker *et al*. (1986)

SLIC Slope-limited Centred scheme, used for estimating numerical flux (Toro 2001)

DGM Depth gradient method, involved in the first step of the SLIC scheme;

WSDGM Weighted surface depth gradient method, involved in the first step of the SLIC scheme; well-balanced property of the model can be achieved if WSDGM is applied

NOTATIONS

Symbol	*Definition*	*First use*
$\mathbf{U}$	vector of conservative variables	Section 2.3
$\mathbf{F}$, $\mathbf{G}$	vectors of fluxes	Section 2.3
$\mathbf{S}_b$, $\mathbf{S}_f$	vectors of the source terms	Section 2.3
$\mathbf{E}$	$=(\mathbf{F},\mathbf{G})$	Section 2.3
$\mathbf{n}$	outward unit vector normal to L	Section 2.3
$\mathbf{r}$	vector for the ratio of the consecutive variations of the conservative variable	Section 2.3
$\mathbf{L}^1, \mathbf{L}^2, \mathbf{L}^3, \mathbf{L}^4$	left eigenvectors of the matrix $\mathbf{A}$	Section 4.1
$\mathbf{Q}$	vector of variables in Eq. (2.29)	Section 2.3
$\boldsymbol{\varphi}$	vector slope limiter in Eq. (2.30)	Section 2.3
$\mathbf{W}$	vector for primitive variables in Eq. (4.2)	Section 4.1
$\mathbf{R}$	vector of source terms in Eq. (4.2)	Section 4.1
$\mathbf{A}$	matrix in Eq. (4.2)	Section 4.1
$\mathbf{I}$	unit matrix	Section 4.1
Superscripts $n,*$	representation of time step	Section 2.3

Superscripts L, R	left and right of an edge of two neighbouring cells	Section 2.3
Subscripts i, j	spatial nodes	Section 2.3
Upper bar $\bar{}$	cell-averaged	
A	area of a computational cell	Section 2.3
a	parameter in Eq. (2.24)	Section 2.3
b	width of the inlet boundary for submarine turbidity currents	Section 5.2
c	volumetric sediment concentration	Section 2.1
c_b	local near bed sediment concentration	Section 2.2
c_D	bed drag coefficient	Section 2.2
c_{D*}	bed drag coefficient under equilibrium condition	Section 2.2
Cr	Courant number	Section 2.3
d	sediment particle diameter;	Section 2.1
D / M_0	deposition density	Section 3.4
E_s	sediment entrainment coefficient	Section 2.2
E_w	water entrainment in the upper interface	Section 2.1
e_w	water entrainment coefficient	Section 2.1
E , D	sediment entrainment and deposition	Section 2.1

	fluxes	
Fr_p	densimetric Froude number at the plunging point	Section 1.4
Fr_0	densimetric Froude number at the inlet boundary	Section 4.2
g	gravitational acceleration	Section 1.4
g'	submerged gravitational acceleration	Section 2.1
H	total thickness of the turbidity current layer and the ambient fluid layer	Section 6.1
h	turbidity current thickness	Section 2.1
$h_{\lim}$	threshold current thickness	Section 2.3
$h_0,\ u_0,\ v_0,\ c_0$	current thickness, velocities and concentration at the inlet boundary	
$h_p,\ u_p,\ c_p$	water depth, flow velocity and sediment concentration at the plunging point	Section 1.4
k	turbulent energy	Section 2.2
$k_1,\ k_2$	coefficients in Eq. (3.1)	Section 3.4
L	boundary of the control volume or computational cell Ω	Section 2.3.1
p	bed sediment porosity	Section 2.1
R	submerged specific gravity of sediment;	Section 2.1

R_1, R_2, R_3, R_4	Components of the vector $\mathbf{R}$	Section 4.1
R_w	Relative density difference between the water and the water-sediment mixture	Section 2.1
R_0	Relative density difference between the sediment bed and the water-sediment mixture	Section 2.1
r_b	ratio of the near-bed concentration and the layer-averaged concentration	Section 2.2
r_w	empirical coefficient representing the ratio of the upper-interface resistance to the bed resistance	Section 2.2
Ri	bulk Richardson number	Section 2.2
$Ri_{\lim}$	critical bulk Richardson number in Eq. (2.39)	Section 2.3
R_{hu}	parameter in Eq. (4.4c)	Section 4.1
R_{ep}	particle Reynolds number	Section 2.2
R_{tx}	contribution ratio of temporal change to spatial change	Section 4.2
S_{bx}, S_{by}	bed slopes in the x - and y -directions	Section 2.1
t	time	Section 2.1
T_σ	time scale of the physical quantity σ	Section 4.1
T_b	time scale of bed deformation	Section 4.1

T_b / T_h	relative time scale of bed deformation	Section 4.1
T_h	time scale of the current thickness	Section 4.1
T_u	time scale of the current velocity	Section 4.1
TC_t	constitute contribution of temporal change	Section 4.2
TC_x	constitute contribution of spatial change	Section 4.2
u , v	layer-averaged velocities in the x - and y - directions	Section 2.1
U	total velocity	Section 2.1
u_*, v_* =	bed shear velocities in the x - and y - directions	Section 2.2
U_*	total bed shear velocity	Section 2.2
x , y	horizontal coordinates	Section 2.1
x_0	location of lock gate in lock-exchange experiments	Section 3.4
z	bed elevation	Section 2.1
Z_m	parameter in Eq. (2.19a)	Section 2.2
α	coefficient in Eq. (2.14)	Section 2.2
β	parameter in Eq. (2.37)	Section 2.3
ϕ	weighting parameter in Eq. (2.33)	Section 2.3

ε_0	dissipation rate	Section 2.2
η	upper current surface elevation	Section 2.3
$\lambda_1, \lambda_2, \lambda_3, \lambda_4$	celerities/eigenvalues of the matrix **A**	Section 4.1
$\lambda_{x\max}$, $\lambda_{y\max}$	maximum celerities in Eq. (2.27)	Section 2.3
ν	kinematic viscosity of water	Section 2.2
π	= 3.1415926	Section 2.3
ρ_S	density of sediment particle	Section 1.4
ρ_f	density of the ambient fluid	Section 1.4
ρ_w	density of water free of sediment	Section 2.1
ρ	density of water-sediment mixture	Section 2.1
ρ_0	density of the saturated bed;	Section 2.1
σ	physical quantity in Eq. (4.1)	Section 4.1
τ_{bx} , τ_{by}	bed shear stresses in the x - and y - directions	Section 2.1
τ_{ux} , τ_{uy}	shear stresses in the upper current surface in the x - and y -directions	Section 2.1
ω	settling velocity of a single particle in tranquil water;	Section 2.2
ξ	Vertical coordinate in Eq. (6.1)	Section 6.1

ψ_p	coefficient of correction in Eq. (2.19a)	Section 2.2
ψ_z	coefficient of correction in Eq. (2.19b)	Section 2.2
Δx , Δy	spatial steps	Section 2.3
Δt	time step	Section 2.2
$\Delta\rho$	density difference between the fluid and sediment phase	Section 2.2
Θ	time variation rate of the physical quantity in Eq. (4.1)	Section 4.1
Ω	control volume or computational cell	Section 2.3.1

LIST OF PUBLICATIONS

Publications relevant to this thesis

1. **Hu, P**., Cao, Z., Pender, G., Tan, G.M. (2012). Numerical Modelling of Turbidity Currents in Xiaolangdi Reservoir, Yellow River, China. *Journal of Hydrology*, Elsevier, moderate revision submitted on 17 April 2012.
2. **Hu, P**., Cao, Z., and Pender, G. (2012). Well-balanced 2D coupled modelling of submarine turbidity currents and their morphological effects. *Maritime Engineering*, Institution of Civil Engineers UK, proofread on 31 Jan 2012.
3. **Hu, P**., and Cao, Z. (2009). Fully coupled mathematical modelling of turbidity currents. *Advances in Water Resources*, Elsevier, 32(1), 1-15.
4. **Hu, P**. (2009). Coupled modelling of turbidity currents over erodible beds. IAHR UK Section Annual Technical Meeting. September, Warrington, UK.
5. **Hu, P**., and Cao, Z. (2008). Numerical modelling of hyperconcentrated turbidity currents. *The 8th International Conference on Hydroscience & Hydraulic Engineering*, September 8-12, Nagoya, Japan.
6. **Hu, P**., and Cao, Z. (2008). Multiple time scales of turbidity currents and their implications for mathematical modelling. *3rd Sino-American Workshop on Advanced Computational Modelling in Hydroscience & Engineering*, May 10-15, Hawaii, USA.

Other publications

7. **Hu, P.,** Cao, Z., and Pender, G. (2012). Surface-based formulation for graded sediment transport in alluvial rivers. To be submitted to *Journal of Hydraulic Research*, IAHR.
8. Cao, Z., **Hu, P**., and Pender, G. (2012). Non-capacity transport of graded bed load sediment transport in alluvial rivers. Submitted to *Journal of Geophysical Research-Earth Surface*.
9. Cao, Z., Li, Z., Pender, G., and **Hu, P**. (2012). Non-capacity versus capacity model for fluvial sediment transport. *Water Management*, Institution of Civil Engineers UK, 165, 193-211.
10. Cao, Z., **Hu, P**., Pender, G., and Liu, H. (2011). Multiple time scales of fluvial processes with bed load sediment and their implications for mathematical modelling. *Journal of Hydraulic Engineering*, ASCE, 137(3), 267-276.
11. Cao, Z., Pender, G., and **Hu, P**. (2011). Multiple time scales of fluvial processes - theory and applications. *Theoretical & Applied Mechanics Letters*, Chinese Society of Theoretical and Applied Mechanics, 1, DOI:10.1063/2.1105201.
12. Cao, Z., **Hu, P**., and Pender, G. (2010). Reconciled bed load sediment transport rates in ephemeral and perennial rivers. *Earth Surface Processes and Landforms*, Wiley, 35(14), 1655-1665.
13. Cao, Z., and **Hu, P**. (2008). Comment on 'Long waves in erodible channels and morphodynamic influence' by Stefano et al. *Water Resources Research*, AGU, 44(W06601), DOI: 10.1029/2006WR005829.

CHAPTER 1. INTRODUCTION

1.1 Phenomenon Clarification

Sediment transport, i.e., the movement of sedimentary solid particles, due to the effects of the gravity of the particles and the forces exerted by the moving fluid (i.e., the transporting agent) is commonly seen in natural environments and has profound morphological effects (e.g., Inman *et al*. 1976; Qian and Wan 1983; Mulder and Cochonat 1996; Parsons *et al*. 2007; Talling *et al*. 2007). In terms of the specific transporting agent, there are fluvial or marine sediment transport (by water flow) and aeolian sediment transport (by wind) (Lu *et al*. 2005). This thesis is concerned with turbidity currents, a type of subaqueous sediment transport process driven by water flow.

There are many ambiguities in the literature with regard to the definition and classification of turbidity currents (Simpson 1997; Kneller and Buckee 2000). In this thesis, the term 'turbidity current' refers to the phenomenon of subaqueous sediment-laden flows driven by negative buoyancy forces. Specifically, turbidity currents are masses of water-sediment mixture moving along a loose boundary (i.e., a river bed or a seafloor) and beneath a layer of less dense ambient fluid. The negative driving force arises from the bulk density excess of the moving water-sediment mixture, as compared to the ambient fluid. Before proceeding, the following clarifications are made for improved understanding of this thesis.

First, only suspended sediment is considered in the simulation of turbidity currents in this study. This is because bed load sediment transport by turbidity current is rarely observed or reported. Nevertheless, the possibility of bed load (as coarse as cobble sizes) by turbidity current has been indicated by the results of the surveys of modern sea floor and turbidite outcrops (Sequeiros *et al*. 2010b), and produced in the laboratory over four bed conditions: plane bed, dune, upstream-migrating antidune and downstream-migrating antidune (Sequeiros *et al*. 2010b). However, turbidity currents carrying bed load sediment are

reserved for future study. Second, the present study follows the perspective of Kneller and Buckee (2000) that both low concentration and high concentration turbidity currents can be regarded as turbidity currents. This excludes the view proposed by Shanmugan (1996, 2002) that sediment in turbidity currents should be supported only by fluid turbulence. At high concentrations, turbidity currents may give rise to hindered settling and dispersive pressure. Third, the buoyancy force for turbidity currents is *negative* (i.e., towards the bed). This indicates that turbidity current should be attached to the loose bottom boundary. This distinguishes turbidity currents from positive (or reversed) buoyancy force-driven subaqueous sediment-laden flows (Sequeiros *et al*. 2009b; Gladstone and Pritchard 2010). Fourth, not all subaqueous negative buoyancy force-driven flows are turbidity currents. Turbidity currents, of which the density excess is due to sediment, are only a subset of subaqueous negative buoyancy force-driven flows, for which the density excess may come from agents such as salinity, temperature etc (Simpson 1997; Huppert 2006). In this regard, turbidity currents have sometimes been simply referred to as density currents or gravity currents. The primary characteristic of turbidity current is its non-conservative nature, because sediment may deposit out or be entrained into the current (Qian and Wan 1983; Simpson 1997), which may reduce or increase the density and driving force of the current. Nevertheless, understanding of saline density currents may also shed insight on that of turbidity currents (Garcia and Parker 1993; Adduce *et al*. 2011). For example, experimental saline density currents were released to an erodible bed by Garcia and Parker (1993) to investigate the potential of sediment entrainment and thereby derive empirical relationship.

Since the 1880s when turbidity currents were recognized for the first time in Lake Geneva by Forel (Qian and Wan 1983; Meiburg and Kneller 2010), their occurrences have been noted in numerous man-made and natural water bodies such as reservoirs (e.g., Fan 1986; Alavian *et al*. 1992; Fan and Morris 1992a, b), river mouths (Mulder and Syvitsski 1995; Mulder *et al*. 1998) and submarine deep water environments (Inman *et al*. 1976; Talling *et al*. 2007). Accordingly, it has been recognized that turbidity currents play a significant role in the global sediment cycle and local sediment redistribution (e.g., Garcia 1992; Middleton 1993; Mulder and Cochonat 1996; Simpson 1997; Talling *et al.* 2007; Meiburg and Kneller 2010). Due to their non-conservative nature, turbidity currents can be either depositional or erosional. Depositional turbidity currents may be responsible for reservoir sedimentation

(e.g., De Cesare *et al*. 2001, 2006; Oehy and Schleiss 2007; YRCC 2007), Gilbert delta development in river mouths (Wright *et al*. 1988), submarine and morphological features such as channel-levee morphology (Nakajima and Satoh 2001; Lamb *et al*. 2008) and sediment waves (Wynn *et al*. 2000; Wynn and Stow 2002). Furthermore, these submarine morphological features have been also termed turbidites that can be an indicator of hydrocarbon reserves (Weimer and Link 1991). Erosional turbidity currents may sculpt submarine canyons, cause dramatic damaging effects on marine facilities (cables and pipes etc) and transport large amounts of sediment over thousands of km before deposition (e.g., Inman *et al*. 1976; Piper *et al*. 1992; Xu *et al*. 2004; Talling *et al*. 2007). Not surprisingly, the understanding of turbidity currents has received much attention in various fields including sedimentary geology, geomorphology, hydraulic engineering, environmental engineering and petroleum engineering etc.

Turbidity currents tend to be erosional over relatively steep slopes, and depositional over relatively mild slopes. Interactions exist between the turbidity current, sediment transport and the bottom bed topography, which determine the turbidity current development and the resultant morphological evolution. These interactions constitute a category of physical problems of significant interest and are fundamental to the understanding of turbidity currents.

1.2 Interactions between Turbidity Current, Sediment Transport and Topography

A primary feature of turbidity currents is that sediment may deposit or be entrained into the current. While propagating downslope of a relatively steep bed slope with given bed texture, turbidity currents tend to be swift with a relatively higher velocity and higher sediment transport capacity. In this case, a net sediment entrainment is likely to happen. The consequence is an increase in the sediment concentration and accordingly an increase in the driving force. The enlarged driving force would lead to further increases in the current velocity, and thus induce more sediment entrainment, in a self-reinforcing cycle (Fukushima *et al*. 1985; Parker *et al*. 1986). This is the phenomenon of self-accelerating turbidity currents, which has been confirmed in the field (Inman *et al*. 1976; Piper *et al.* 1999) and in the laboratory (Sequeiros *et al*. 2009c) and by numerical case studies

(Fukushima *et al*. 1985; Parker *et al*. 1986). In contrast to self-accelerating turbidity currents, turbidity currents over a relatively mild slope would be decelerating and finally dissipating. As sediment deposits, the sediment concentration and the density excess decrease, reducing the driving force. Consequently the current becomes weak, giving rise to more deposition, in the reverse to self-accelerating turbidity currents. The interactions between the turbidity current, sediment transport and topography are clear from the above two distinct destinies of turbidity currents.

There have been many literature reviews on turbidity currents, which partly reflect previous research efforts. Most existing reviews deal with turbidity currents that occur in a specific environment, see for example the reviews about reservoir turbidity currents (Fan and Morris 1992a, b), submarine turbidity currents (e.g., Middleton 1993; Shanmugam 1996; Parsons *et al*. 2007) and turbidity currents in river mouths (Mulder *et al*. 2003). Few of these put a focus on the interactions between the turbidity current, sediment transport and the bed topography. In the following sections, previous studies are first briefly reviewed in terms of the research methods, with a special focus on how the interactions are considered. Based on the present survey of the research methods, the layer-averaged mathematical modelling approach is chosen as the methodology in this thesis and the first two objectives are identified. Then submarine turbidity currents and reservoir turbidity currents are identified for numerical investigations. Finally the structure of this thesis is summarized.

1.3 Survey on Research Methodologies

Previous research methodologies for the investigation of turbidity currents mainly include field observations, laboratory experiments and numerical modelling, which have been used either independently or combined.

1.3.1 Field observations

Field observation is the most direct and straightforward way of studying natural phenomenon. Significant knowledge of the behaviour of turbidity currents has been derived from field observations. The existence of turbidity currents was first established by field

observations in Lake Geneva (Qian and Wan 1983; Meiburg and Kneller 2010), for which it was postulated that a subaqueous canyon had been created by sediment-laden underflows from the Rhone River (Meiburg and Kneller 2010). Though rarely observed directly in submarine environments, the occurrence of submarine turbidity currents were continuously confirmed by the analyses of the resultant submarine morphological features (e.g., Allen 1991; Pirmez and Imran 2003; Amy and Talling 2006). Finally, knowledge of the destructive effects of turbidity currents was obtained from the field observations that submarine pipes were broken by turbidity currents (e.g., Inman *et al*. 1976; Parker *et al*. 1986; Piper *et al*. 1992, 1999).

Nevertheless, the total number of direct field observations of turbidity currents remains relatively few, though reported in the Zaire submarine valley (Khripounoff *et al*. 2003), in the Monterey Submarine Canyon (Xu *et al*. 2004; Xu 2010), and in reservoirs of the Yellow River, China (YRCC 2007) etc. These observations are usually event-specific. More importantly, information from these field observations is very limited. It is difficult to derive any systematic understandings from these observations. This is understandable as there are several factors that make this method challenging. The first factor relates to the nature of turbidity currents as the underwater measurement of sediment-laden flow requires a high dependency on technology, which is expensive in deep hostile water environments. Moreover, the occurrence of turbidity currents is unpredictable. Even if they are directly observed, the observations are likely to be incomplete (Xu *et al*. 2004; YRCC 2007). Third, the highly destructive effects of turbidity currents may damage the measuring facilities (Xu *et al*. 2004; Xu 2010). For example, a 2.5-cm-diameter steel rod 3 m above the bed in about 44 m water depth was bent by 90^{o} due to the passage of turbidity currents (Inman *et al*. 1976).

Field surveys of the resultant morphological features (e.g., seismic profiles, outcrops etc) by turbidity currents are viable, which have been used to back-estimate the current characteristics that shaped those morphological features. For example, analyses of field outcrops have shown that obstacles in the bottom topography may induce current nonuniformity and thus affect deposition (Kneller and McCaffrey 1999, 2003; Kneller and Buckee 2000). Weirich (1988) has speculated the existence of submerged (internal)

hydraulic jumps for turbidity currents by analyzing the deposits in a reservoir. A bedform-velocity matrix has been estimated by Stow *et al*. (2009) to assess the velocity and accordingly the destructive powers of turbidity currents. The formation of many submarine morphological features (canyons, fans, gullies, channel-levee morphology and sediment waves) has been attributed to turbidity currents. While much qualitative understanding can be obtained from these analyses, further progress largely depends on the improvement of deep-sea sampling techniques. More importantly, it has been argued that there has been no standard criterion to reliably interpret transport mechanisms from the depositional records, because different mechanisms are often derived from the same depositional record by different researchers (Shanmugam 1996, 2002).

1.3.2 Laboratory experiments

Laboratory experiment provides a well-controlled way to understand systematically natural phenomena. Numerous laboratory experiments have been undertaken to study turbidity currents.

There are two classical ways of generating turbidity currents in the laboratory: 1) lock-release (exchange) turbidity currents with a finite volume of water-sediment mixture; and 2) continuous turbidity currents featuring an increasing volume of water-sediment mixture with time. In both configurations, a reservoir of static clear water (free of sediment) is first established. Water-sediment mixture is then introduced into the reservoir, either by withdrawal of the lock gate or by feeding water-sediment mixture continuously. The use of a reservoir of static clear water as ambient fluid in the two configurations may be based on the observation that natural environments prone to the occurrence of turbidity currents (i.e. reservoirs and submarine deep water environments) are all characterized by relatively static water bodies. However, it should be noted these water bodies are not totally static. They may be characterized by small flow velocities, especially in river mouths dominated by tides.

Experimental continuous turbidity currents have been mainly used to investigate the depositional and evolutional characteristics of turbidity currents in one-dimension (e.g.,

Altinakar *et al*. 1990; Lee and Yu 1997; Yu *et al*. 2000; Alexander and Mulder 2002) and two-dimension (e.g., Imran *et al*. 2002; Baas *et al*. 2004; Alexander *et al*. 2008; Rowland *et al*. 2010; Cantelli *et al*. 2011); the vertical structure of the current and sediment (e.g., Altinakar *et al*. 1996; Choux *et al*. 2005; Gray *et al*. 2005; Eggenhuisen and McCaffrey 2011; Nourmohammadi *et al.* 2011); and the effects of turbulence structure on sediment distribution (Baas *et al.* 2005). Experimental lock-exchange turbidity currents are mainly deployed to understand their depositional characteristics and the propagation rate of the current front (e.g., Bonnecaze *et al*. 1993, 1995; Dade and Huppert 1995; De Rooij and Dalziel 2001); and the durations and features of the three stages of lock-exchange turbidity currents themselves (Simpson 1997).

Many of these laboratory experiments have clearly demonstrated the interactions between the turbidity current, sediment transport and the bottom topography. Experimental efforts by Kneller and his collaborators have revealed the considerable impacts of topography on the evaluation of the current, sediment deposition and the vertical structure of the current (e.g., Kneller *et al.* 1991; Alexander and Morris 1994; Brunt *et al.* 2004). Kneller *et al*. (1991) suggested a mechanism for the generation of internal solitary waves for turbidity currents encountering an oblique ramp. Experimental turbidity currents through a slope break in topography have been demonstrated to be characterized by abrupt decrease in current velocity and concentration and increase in bed deposition and current thickness, with and without an internal hydraulic jump (e.g., Garcia and Parker 1989; Garcia 1993, 1994; Mulder and Alexander 2001; Toniolo *et al*. 2006a, b). In an experimental investigation of how the observed submarine sediment waves are formed by turbidity currents, more deposition in the upstream side of a mound is consistently observed (Kubo and Nakajima 2002). Moreover, a series of experimental turbidity currents entering small minibasins were reported. Different inflow conditions (surging vs. continuous inflow) were used, and different initial minibasin morphologies (width and height) were created (e.g., Brunt *et al*. 2004; Lamb *et al.* 2004, 2006; Violet *et al.* 2005; Toniolo *et al*. 2006a, b). These experiments clearly show different depositional patterns. The interactions of the current, sediment transport in meandering or sinuous channels have also been intensively studied experimentally in the past decades to understand submarine channel-levee morphologies (e.g., Peakall *et al.* 2007; Kane *et al*. 2008, 2010; Straub and Mohrig 2008;

Straub *et al*. 2008, 2011). In Sequeiros *et al.* (2010a), a set of 74 experiments on turbidity currents flowing over a mobile bed is reported, by which the effects of plane bed condition and bed form on the vertical profiles of velocity and concentration are revealed under conditions of both subcritical and supercritical flow regimes. For example, in the case of a plane bed, it features a higher vertical location for the peak velocity for subcritical flow regime than the supercritical flow regime.

In addition to the direct use of water-sediment mixture, saline/brine density currents have also been generated to shed insight on the understanding of turbidity currents, such as the vertical velocity profiles (Kneller *et al*. 1997, 1999; Sequeiros *et al*. 2010a) and current structure in meandering and sinuous channels (Keevil *et al*. 2006, 2007), sediment entrainment estimation (Garcia and Parker 1993), water entrainment estimation (Hallworth *et al.* 1993), evolution mechanism of lock-exchange turbidity currents (Huppert and Simpson 1980; Amy *et al*. 2005a) etc. These investigations are reasonable because recent experiments seem to indicate that the shear stress distribution and structure for experimental density and turbidity currents are similar (Cossu and Wells 2011), thus it is possible to derive some understanding of turbidity current from saline/brine density current.

Although laboratory experiments contribute greatly to the understanding of turbidity currents and the associated interactions, experimental investigations largely hinge on high-resolution measurement techniques. Accurate simultaneous measurements of the current velocity and sediment concentration have proven to be a difficult task for turbidity currents (McCaffrey *et al.* 2003; Felix *et al*. 2005). Notably, for turbidity currents, it is always difficult to identify its upper interface with the ambient fluid, thus vertical profiles of current velocity or sediment concentration have been used to derive the current thickness and accordingly the current surface (Parker *et al*. 1987; Garcia and Parker 1993). The insufficient accuracy of field measurements may lead to appreciable errors in the estimated current surface and current thickness. Furthermore, laboratory experiments are constrained by the small flume scale and thus greatly limit its potential for comprehensive understanding (Middleton 1993).

1.3.3 Numerical modelling

In comparison to field observations and laboratory experiments, mathematical numerical modelling provides a good alternative to aid the development of a comprehensive understanding of turbidity currents. Mathematical numerical models of turbidity currents have been developed under distinct frameworks ranging from models based on classical fluid dynamics principles to new methods that have emerged from alternative computational paradigms such as the cellular automata technique.

The cellular automata technique has been recently deployed to simulate turbidity currents (Salles *et al.* 2007). In this technique, the dynamic system of turbidity currents is subdivided into elementary parts, and simulated by updating each elementary part. Yet this technique is still in its infancy for turbidity current simulation.

In an effort to understand the abundant experimental data from lock-exchange turbidity currents, a category of box model has been developed to fit the observed run out distance against time and the deposition depth, which appears satisfactory (e.g., Huppert 1998; Chowdhury and Testik 2010; Meiburg and Kneller 2010). Yet, empirical relations between the current velocity and the Froude number are usually applied at the current front to capture the run out distance against time (Bonnecaze *et al*. 1993, 1995; Gladstone and Woods 2000). Application of box models to field conditions has rarely been reported. Moreover, the applicability of box models to other configurations (say, for continuous turbidity currents) is very limited.

Mathematical modelling based on classical fluid dynamics has been widely used in sediment transport modelling, not only for subaqueous turbidity currents but also for sediment-laden open channels (e.g., Cunge *et al.* 1980; Wu 2007; Fasolato *et al*. 2009; Chowdhury and Testik 2010; Meiburg and Kneller 2010). These models can be classified into two categories: depth-resolving models and layer-averaged models (Meiburg and Kneller 2010). Depth-resolving models include vertical 2D and full 3D models, and commonly involve turbulence closures (e.g., Farrell and Stefan 1988; Eidsvik and Brors 1989; Choi and Garcia 2002b; Felix 2002; Huang *et al*. 2005, 2007, 2008; Khan and Imran 2008; Firoozabadi *et al.* 2009; Sequeiros *et al*. 2009b; Yam *et al*. 2011) or are formulated

on the basis of direct numerical simulation (Necker *et al*. 2002, 2005; Blanchette *et al*. 2005; Mahdinia *et al*. 2011). The application of direct numerical simulations is mainly limited to small scale lock-exchange turbidity currents with low Reynolds number. Turbulence closure-based models are capable of resolving the current and sediment structures along the depth. Yet they are theoretically limited because the physics of turbulence remains poorly understood, on which turbulence closures are based. It remains far from clear how to incorporate the effects of sediment into turbulence closure models, even for steady and uniform sediment-laden flows in open channels (Cao *et al*. 2003). Thus very low sediment concentration is usually assumed in these models so that the impact of sediment on turbulence can be negligible. In this connection, sediment is indeed a passive constituent that has negligible impact on the current. Furthermore, most of these models use a fixed grid system and thus ignore the effects of morphological change (i.e., change of the bottom boundary). In the case of rapid bed morphological changes, an adaptive grid system may be required for vertical 2D and full 3D modelling (Huang *et al.* 2005), which may reduce considerably the computational efficiency. Nevertheless, some adaptive grid systems have been shown to be efficient for depth-averaged shallow water modelling, such as the quadtree adaptive grids by Rogers *et al*. (2001, 2003).

Layer-averaged models, which do not involve turbulent closures and feature a sensible balance between theoretical rigour and applicability to practical cases, can provide accurate evaluations of current thickness, layer-averaged velocity and concentration, morphological changes and run out distance (Huppert 1998; Kneller and Buckee 2000). L*ayer-averaged* refers to the fact that the physical quantities (velocity and sediment concentration) are averaged along the thickness of the concerned layer (Parker *et al*. 1986).

As the turbidity current propagates and spreads beneath a layer of ambient fluid, there are two kinds of layer-averaged models: a category of two-layer model that resolves the evolution of both the turbidity current layer and the ambient fluid layer, and a category of one-layer model resolving only the turbidity current layer. In one-layer models, the impact of the ambient fluid layer is incorporated through a water exchange flux between the two layers. One-layer models have been widely used since the 1980s (Fukushima *et al*. 1985; Parker *et al*. 1986) and provide a reasonable representation of turbidity current

development and morphological changes (Huppert 2006). Two-layer models have also been developed (Bonnecaze *et al*. 1995), which deploy two sets of layer-averaged equations describing the turbidity current layer and the ambient fluid layer, respectively. For two-layer models, the computational cost is twice that of a one-layer model because of the doubled number of equations to be solved. Furthermore, the two-layer model theory requires to be improved as some unrealistic phenomena may be produced during the simulations. For example, internal waves were computed when simulating an experimental turbidity current by a two-layer model, which were not observed in experiments (Bonnecaze *et al*. 1995). In the present investigation, the widely used one-layer model theory is adopted. In the following, all models refer to the one-layer model.

Many one-dimensional (1D) and two-dimensional (2D) layer-averaged models have been developed under the framework of the one-layer model theory. In most existing layer-averaged models of turbidity currents, the interactions between the turbidity current, sediment transport and bed topography are not properly accounted for. They are either decoupled in that bed deformation is not considered at all (Fukushima *et al.* 1985; Parker *et al*. 1986), or only partially coupled in that the feedback impacts of morphological changes are ignored, though bed deformation is tracked (Bonnecaze *et al.* 1995; Zeng and Lowe 1997a, b; Choi 1998, 1999; Imran *et al*. 1998; Bradford and Katopodes 1999a, b; Choi and Garcia 2002a; Fildani *et al*. 2006; Sequeiros *et al*. 2009a). Mathematically, they are based on simplified governing equations, which are not in accordance with the complete conservation laws. Physically, they are built upon the presumption that the current involves no or only weak sediment transport and mild bed deformation. In reality, however, turbidity currents of practical interests are often characterized by rapid morphological changes and thus active sediment transport, of which the interactions between the turbidity current, sediment transport and topography may be considerable.

Using a three equation model without considering bed deformation at all by Parker *et al.* (1986), physically unrealistic solutions were obtained for self-accelerating turbidity currents. Parker *et al.* (1986) proposed that this was due to an imbalanced supply of the turbulent energy to maintain the sediment, and introduced a constraint for the turbulent energy, which essentially constrains the magnitude of bed shear stress and thus the

sediment entrainment. This leads to a four equation model, which also ignores bed deformation completely. Although realistic solutions were obtained using the four equation model, it is very likely that considerable uncertainties are introduced at the same time. This is because the basis of the turbulent energy constraint, i.e., the physics of turbulence for turbidity currents remains far from clear. Not surprisingly, the four equation model as well as the turbulent energy constraint is now rarely used (Pratson *et al*. 2001; Fildani *et al*. 2006). Physically, the unrealistic solutions by the three equation model are probably due to the complete neglect of bed deformation, though the steady flow assumption may also contribute to it.

There are three aspects that need to be carefully dealt with for layer-averaged turbidity current modelling. The first is due to the possibility of the occurrence of an internal hydraulic jump (Weirich 1988), which transforms supercritical turbidity currents into a subcritical flow regime and thus necessitates a model capable of capturing shock waves. The second is concerned with the reproduction of the propagation and spreading of turbidity currents, i.e., tracking the current front. The third is associated with the applicability of the model to irregular topographies typical of field applications.

Layer-averaged models have been pursued as early as 1980s for turbidity currents and accordingly a variety of numerical algorithms have been available to solve the governing equations. In the early steady three-equation models, the standard step method was applied and no attention was paid to tracking the current front. Such models are only approximately applicable to flat topography. The reproduction of the internal hydraulic jump needs to be accomplished with the help of an empirical relation (Garcia 1994). Later the steady current assumption was relaxed, and several partially coupled unsteady models were proposed using different numerical algorithms including the two-step Lax-Wendroff method (Bonnecaze *et al*. 1993, 1995); the dissipative-Galerkin based finite element method (Choi 1998); the Beam and Warming alternate direction implicit method (Imran *et al*. 1998); and the staggered grid approach (Pratson *et al*. 2001). In these models, the issue of the wet/dry front is well tackled. For example, empirical relations between the Froude number and the current velocity at the current front are applied (Bonnecaze *et al*. 1993, 1995). The concept of threshold current thickness is applied in turbidity current modelling (Imran *et al*. 1998),

which was initially proposed for river basin flow modelling (Zhao *et al*. 1994). Yet in most of these models, the ability to capture the internal hydraulic jump and track the current front has not been resolved simultaneously for turbidity currents, until a TVD version of the finite volume method was applied, i.e., the use of the Roe's approximate Riemann solver under the framework of the finite volume method by Bradford and Katopodes (1999a, b).

Further efforts along this line (applying the TVD version of the finite volume method) for turbidity currents are rarely reported. This might be due to the difficulty of TVD algorithms to preserve an approximately static condition over irregular topographies (e.g., Hubbard and Garcia-Navarro 2000; Zhou *et al*. 2001; Rogers *et al*. 2003; Aureli *et al*. 2008; Liang and Marche 2009; Serrano-Pacheco *et al*. 2009). The TVD algorithms need to be carefully designed such that the flux gradients and the geometric source terms can be well-balanced, which is critical for field applications characterized by irregular topographies. Fortunately, in the past decade, the development of well-balanced TVD algorithms has been a very active area of research for open channel flows, which can be essentially extended for the present turbidity current modelling.

The first objective is to develop a fully coupled layer-averaged mathematical model for turbidity currents, which explicitly incorporates the interactions between the turbidity current, sediment transport and topography, and properly deals with the three aspects for layer-averaged modelling. The second objective is to reveal theoretically the significance of the incorporation of the interactions in turbidity current modelling, i.e., the significance of fully coupled modelling.

1.4 Submarine Turbidity Currents and Their Morphological Effects

Submarine turbidity currents are usually initiated by submarine landslide, slump and debris flow due to earthquake, storm surges, volcanic eruptions and volcanically triggered subglacial lake breakouts etc (Pratson *et al.* 2007; Meiburg and Kneller 2010). Although submarine turbidity current activities are rarely observed directly (e.g., Khripounoff *et al*. 2003; Xu *et al*. 2004; Xu 2010), their existence has been well confirmed from the analyses of the resultant morphological features (seismic profiles and outcrops etc) (e.g., Normark

1999; Allen 1991; Pirmez and Imran 2003; Amy and Talling 2006). Accordingly, the formation of many submarine morphological features (submarine channels, levees and sediment waves etc) has been attributed to turbidity current activities and thus attracted much attention from sedimentologists.

Submarine erosional turbidity currents favour high velocity in continental shelf and slopes characterized by relatively steep bed topographies, suitable for generating self-accelerating turbidity currents. These carve into the continental slope and sculpt most submarine canyons. Depositional examples include the sinuous channel in the Amazon fan (Hiscott *et al.* 1997; Pirmez and Imran 2003); the channel-levee complex in the Monterey canyon and fan (Normark 1999; Fildani *et al*. 2006); the channel-levee complex in the Japan sea (Nakajima *et al*. 1998; Nakajima and Satoh 2001); an Upper Cretaceous channel-levee complex in the Rosario formation, Mexico (Kane *et al*. 2007, 2009; Dykstra and Kneller 2008) and a channel in Polar North Atlantic (Cofaigh *et al.* 2006) etc. The deposited turbidites also form an important class of hydrocarbon reservoirs (Weimer and Link 1991; Meiburg and Kneller 2010).

There have been many laboratory experiments looking at the incipient channel formation by turbidity currents (Imran *et al*. 2002; Baas *et al*. 2004; Toniolo *et al.* 2004; Alexander *et al*. 2008; Cantelli *et al*. 2011). The common point of these experiments is to see how submarine channels are formed when turbidity currents are fed into an unconfined flat open space. The results differ from each other. Small-scale channels are formed in some of these investigations (Imran *et al.* 2002; Baas *et al*. 2004), yet most produce deposited lobes or elongated ridges (e.g., Baas *et al.* 2004; Toniolo *et al.* 2004; Alexander *et al*. 2008; Sangster *et al*. 2010). There have been also investigations on evolution of turbidity currents in established channel systems (e.g., Kane *et al*. 2008, 2010; Straub *et al.* 2008, 2011; Straub and Mohrig 2008). More recently, Rowland *et al.* (2010) indicated experimental investigations of channel formations by turbidity currents are limited due to the small scales involved.

Most research on submarine turbidity current focuses on back-calculation of current variables from the channel-shape properties along with grain size and sediment-volume data from the deposition (e.g., Komar 1969, 1971; Shanmugam 1996, 2002). Komar (1969)

proposed a relation to back-calculate the current hydrodynamic variables by taking the differences in levee asymmetry as a proxy for current superelevation. Later, experimental measurement of turbidity currents in a sinuous channel by Straub *et al.* (2008) suggested that the relation by Komar (1969) may underestimate current superelevation and thus overestimate current velocity, due to the ignorance of current overspill. More recently, Cossu *et al*. (2010) attributed the current velocity overestimation to the neglect of the Coriolis force (Cossu and Wells 2010, 2011). Obviously, the basis of the back-calculations remains an open question. Moreover, the approach of back-calculation cannot resolve the process of the formation of morphological features by turbidity currents. There have been interesting linear stability analyses to examine the formation of submarine morphological features. For the formation of channel morphology, Hall *et al*. (2008) suggest that the vertical sediment concentration needs to decay more slowly away from the bed than the shear stress inside the current. Izumi (2004) concludes that submarine gully spacing is of the order of 150-8000 m. While linear stability analyses provide some qualitative knowledge, they also cannot resolve how the current and morphology evolve and interact symbiotically. Birman *et al*. (2009) propose a conceptual model for transverse levee morphology based on the steady conservation of sediment in the lateral direction. Yet uniform flow in the mainstream direction is assumed, which precludes downstream variation.

Existing numerical modelling deploys decoupled or partially coupled models (Imran *et al*. 1998, 2002; Bradford and Katopodes 1999b). The application of the present coupled model is therefore of significant interest. Chapter 5 presents a computational study of submarine turbidity currents and their morphological effects (see Chapter 5).

1.5 Turbidity Currents and Reservoir Sediment Management

When sediment-laden open channel floods enter a river reservoir, they may plunge and propagate along the bottom of the reservoir in the form of turbidity currents. By field observations and laboratory experiments, a critical condition for the plunging phenomenon has been established: the densimetric Froude number ($Fr_p = u_p / \sqrt{(\rho_s - \rho_f)/\rho_f g c_p h_p}$, with

h_p, u_p and c_p = water depth, flow velocity and sediment concentration at the plunging point) needs to be around 0.6 (e.g., Qian and Wan 1983; Fan 1986; Fan and Morris 1992a, b; Lee and Yu 1997; Nokes *et al.* 2008). This condition can be used as a rough criterion. Field observations and experimental studies also indicate that higher sediment concentration, lower flow discharge favours the plunging phenomena. Another direct indicator for the plunging phenomenon is the appearance of floating debris on the water surface, of which the location is usually the plunging point (e.g., Qian and Wan 1983; Fan 1986; Fan and Morris 1992a, b). Once plunged, turbidity currents take responsibility for the sediment transport and flushing. If the turbidity current can arrive at the dam, it will be possible to flush sediment out of the reservoir. Otherwise, severe sedimentation in the reservoir and bed scour downstream of the dam will occur. It is not surprising to see numerous reports that sediment deposition by turbidity currents is responsible for much of reservoir sedimentation in the world (e.g., Fan 1986; Farrell and Stefan 1988; Fan and Morris 1992a, b; De Cesare *et al.* 2001, 2006; Oehy and Schleiss 2007). Apparently, turbidity currents play a critical role in effective sediment and reservoir management in alluvial rivers. Enhanced understanding of turbidity currents is critical for effective sediment and reservoir management, flood mitigation and fish habitat recovery. There have been numerous investigations on how to make use of the turbidity current phenomenon to reduce reservoir sedimentation, see for example the reviews by Fan (1986) and Fan and Morris (1992a, b) on the efforts of Chinese engineers and scientists, and the depth-resolving turbulence-closure based modelling efforts in Switzerland (e.g., De Cesare *et al*. 2001, 2006; Oehy and Schleiss 2007); and many other theoretical analyses conducted in America (e.g., Kostic *et al*. 2002; Kostic and Parker 2003a, b; Parker and Toniolo 2007; Toniolo *et al.* 2007; Toniolo 2009).

Especially in the Yellow River of China that is well known due to its very high sediment concentrations (as also indicated by its name *Yellow* River), the issue of reservoir sedimentation has received much attention (e.g., Li 2004; Li *et al*. 2006; Xu *et al*. 2007; YRCC 2007). As seen in Figure 1.1, many reservoirs have been built on the Yellow River. The average annual sediment load of the Yellow River, was estimated to be as high as 1.6 billion tonnes in relation to the average annual runoff of about 43.2 billion m^3 (Qian and Wan 1983). Alternatively, the average volumetric sediment concentration is over 0.014 (or

37 kg/m^3), probably the highest worldwide. Most notably, these sediment loads are usually transported in a few hyper-concentrated sediment-laden flood events in the flood season each year. Turbidity currents have been frequently observed in the Yellow River, giving rise to a high awareness of making use of turbidity currents to reduce reservoir sedimentation (YRCC 2007).

The present study is concerned with turbidity currents in the Xiaolangdi reservoir in the lower Yellow River (Figure 1.1), about 130 km downstream of the Sanmenxia reservoir. The construction of the Xiaolangdi reservoir is a key project in the Yellow River as it controls an drainage area of about 0.7 million km^2 (92.3% of the total basin area of the Yellow River) and almost 100% sediment load of the Yellow River. It was completed in 2001 with the main purpose of mitigating flood risk. Large amounts of sediment have settled in the reservoir and its downstream reach, reducing its water storage capacity and the conveyance capacity of the downstream reach (Li 2004). To reduce sedimentation or preferably generate bed scour, a series of field scale water-sediment regulation experiments have been undertaken since 2002 by the Yellow River Water Resources Commission, involving mainly the Xiaolangdi, Sanmenxia and Wanjiazhai reservoirs (e.g., Li 2004; Li *et al*. 2006; Qu *et al*. 2006; Xu *et al*. 2007; YRCC 2007). Turbidity currents were observed in the Xiaolangdi reservoir and believed to be the major means of flushing sediment through the reservoir. Much field hydrological data has been obtained. However, most of post-experimental analyses are based on simple empirical relations (e.g., Li 2004; Li *et al*. 2006; Qu *et al*. 2006; Xu *et al*. 2007; YRCC 2007), which cannot resolve the current evolution and provide sufficient support for design of future experiments. There has been a lack of quantitative analyses of these hydrological data on turbidity currents using process-resolving models. It remains unclear how and to what extent physically based numerical models can resolve current evolution as compared against field observations. A computational study of turbidity currents in the Xiaolangdi Reservoir, Yellow River is presented in Chapter 6.

Figure 1. 1 Sketch of the Yellow River.

1.6 Summary

In this thesis, a layer-averaged two-dimensional fully coupled mathematical model will be developed and applied for turbidity currents over erodible beds. The model explicitly accounts for the interactions between the current, sediment transport and topography and features a new well-balanced algorithm to deal with the three challenging issues.

The governing equations, the empirical closures and the numerical algorithm for the fully coupled model are presented in Chapter 2.

In Chapter 3, the fully coupled model is tested against a series of idealized and experimental turbidity currents in terms of its performance in tackling the three modelling issues and its accuracy in reproducing key current variables.

In Chapter 4, the importance of the fully coupled modelling is demonstrated through the multiple-time-scale-theory complemented by numerical case studies of the self-accelerating turbidity currents representative of those occurring in the Submarine Scripps Canyon.

Chapter 5 presents a numerical study of the morphological effects of submarine turbidity currents. Two cases of submarine turbidity currents, i.e., a submarine canyon-fan transition

and the incipient formation of channel-levee morphology over submarine fans, are numerically simulated using the fully coupled model. The effects of three key factors dictating the formation of channel-levee morphology are systematically examined.

Chapter 6 presents the application of the fully coupled model to the turbidity currents in the Xiaolangdi Reservoir in the lower Yellow River. Two events of turbidity currents are numerically revisited to calibrate and validate the model. Special attention is paid to the current front advancing and the sediment transport rate.

Conclusions and discussions are presented in Chapter 7.

Chapter 2. MATHEMATICAL FORMULATIONS

Summary:

- Interactions between the current, sediment transport and topography are explicitly incorporated in the governing equations
- Three challenging issues for numerical modelling of turbidity currents are resolved by the numerical algorithm
- Differences between the present coupled model with several previous models are highlighted

Mathematical formulations are presented for layer-averaged turbidity current modelling, including the governing equations, the auxiliary relationships and the numerical algorithm. A comparison of the FCM with previous decoupled and partially coupled models is presented.

2.1 Layer-averaged Governing Equations

2.1.1 One-dimensional governing equations

Layer-averaged modelling of turbidity currents has been pursued for several decades (e.g., Fukushima *et al.* 1985; Parker *et al.* 1986; Bonnecaze *et al*. 1995; Zeng and Lowe 1997a, b; Choi 1998, 1999; Imran *et al*. 1998; Bradford and Katopodes 1999a, b; Choi and Garcia 2002a; Fildani *et al*. 2006; Sequeiros *et al*. 2009a). Parker *et al*. (1986) provide a detailed derivation of layer-averaged conservation equations for turbidity current. Yet the

interactions between turbidity current, sediment transport and bed topography are not fully accounted for in the governing equations presented in Parker *et al*. (1986). Important assumptions are as follows in relation to the 1D turbidity current sketched in Figure 2.1, which depicts a longitudinal 1D turbidity current over an erodible bed that is composed of sediment with particle diameter d . First, the ambient fluid is assumed to be sufficiently thick and well-mixed without stratification. Second, hydrostatic pressure assumption is made within the turbidity current layer. Third, the horizontal convection velocities for the water and sediment phases are the same. Fourth, assumption of similarity is made for the vertical profiles of current velocity and sediment concentration so that shape coefficients in the vertical integrations are equal to unity.

Pantin (1979) proposes a set of complete layer-averaged mass and momentum conservation equations for the turbidity current, but bed deformation is not considered at all. Based on Pantin (1979)'s work and by incorporating the mass conservation of bed material (i.e., the well-known bed deformation equation), the complete mass and momentum conservation equations for 1D turbidity current read

$$\frac{\partial(\rho h)}{\partial t}+\frac{\partial(\rho hu)}{\partial x}=\rho_0\frac{E-D}{1-p}+\rho_w E_w \tag{2.1}$$

$$\frac{\partial(\rho hu)}{\partial t}+\frac{\partial[\rho hu^2+(\rho-\rho_w)gh^2/2]}{\partial x}=(\rho-\rho_w)ghS_{bx}-(\tau_{bx}+\tau_{ux}) \tag{2.2}$$

$$\frac{\partial(hc)}{\partial t}+\frac{\partial(huc)}{\partial x}=E-D \tag{2.3}$$

$$(1-p)\frac{\partial z}{\partial t}=D-E \tag{2.4}$$

where t = time, x = horizontal coordinate, h = current thickness, u = layer-averaged velocity, E and D is the sediment entrainment and deposition fluxes from and onto the erodible bed respectively, p = bed sediment porosity, $\rho=\rho_s c+\rho_w(1-c)$ = density of the water-sediment mixture, $\rho_0=\rho_s(1-p)+\rho_w p$ = density of the saturated bed sediment, c = layer-averaged volumetric sediment concentration, ρ_w and ρ_s = densities of water and

sediment respectively, ρ_w = 1000 kg/m^3, $E_w = e_w u$ is water exchange (entrainment or detrainment) in the upper current surface, e_w= water exchange coefficient, τ_{bx} and τ_{ux} = shear stresses in the x-direction in the bottom and upper current surface respectively, $S_{bx} = -\partial z / \partial x$ is the bed slope in the x-direction, z = bed elevation.

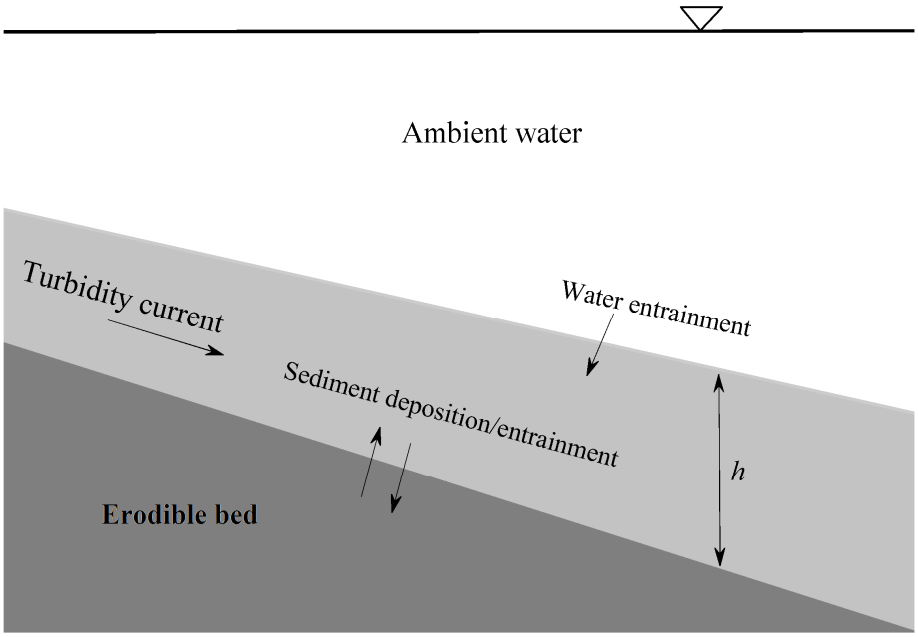

Figure 2. 1 One-dimensional sketch for turbidity current.

Eqs. (2.1) and (2.2) are recast so that the densities ρ and ρ_w do not appear on the Left-Hand-Side (LHS), in a similar way to Cao *et al*. (2006) for sediment-laden open channel flow modelling. Through mathematical manipulations, the following are obtained

$$\frac{\partial h}{\partial t} + \frac{\partial (hu)}{\partial x} = E_w + \frac{E - D}{1 - p} \tag{2.5}$$

$$\frac{\partial hu}{\partial t} + \frac{\partial (hu^2 + g' h^2 / 2)}{\partial x} = g' h S_b - \frac{\tau_b + \tau_u}{\rho} - R_w u E_w - R_0 u \frac{E - D}{1 - p} \tag{2.6}$$

where $g' = Rgc$ is the submerged gravitational acceleration, $R = (\rho_s - \rho_w)/\rho$ is the submerged specific gravity of the sediment, $R_w = (\rho_w - \rho)/\rho$, $R_0 = (\rho_0 - \rho)/\rho$ denote the

relative difference of densities of water and saturated bed, respectively, in relation to the density of the water-sediment mixture.

2.1.2 Two-dimensional (2D) governing equations

It is straightforward to extend the 1D governing equations to 2D condition. They are

$$\frac{\partial h}{\partial t}+\frac{\partial (hu)}{\partial x}+\frac{\partial (hv)}{\partial y}=e_w U+\frac{E-D}{1-p} \tag{2.7}$$

$$\frac{\partial hu}{\partial t}+\frac{\partial (hu^2+g'h^2/2)}{\partial x}+\frac{\partial (huv)}{\partial y}=g'hS_{bx}-\frac{\tau_{bx}+\tau_{ux}}{\rho}-R_w e_w Uu-R_0\frac{E-D}{1-p}u \tag{2.8}$$

$$\frac{\partial hv}{\partial t}+\frac{\partial (huv)}{\partial x}+\frac{\partial (hv^2+g'h^2/2)}{\partial y}=g'hS_{by}-\frac{\tau_{by}+\tau_{uy}}{\rho}-R_w e_w Uv-R_0\frac{E-D}{1-p}v \tag{2.9}$$

$$\frac{\partial (hc)}{\partial t}+\frac{\partial (huc)}{\partial x}+\frac{\partial (hvc)}{\partial y}=E-D \tag{2.10}$$

$$(1-p)\frac{\partial z}{\partial t}=D-E \tag{2.11}$$

where v = current velocity in the y -direction, $U=\sqrt{u^2+v^2}$ is the magnitude of the layer-averaged velocity vector, τ_{by} and τ_{uy} = shear stresses in the x -direction in the bottom and upper current surface respectively, $S_{bx}=-\partial z/\partial y$ is the bed slope in the y -direction. Other symbols in the above equations have the same meanings as those in the 1D Eqs. (2.1-2.6).

2.2 Auxiliary Relationships

A set of physical variables are involved in the governing equations, which need to be determined empirically to close the equations. These include the water exchange in the

upper current surface, the sediment exchange (entrainment and deposition) between the current and the loose boundary, the shear stresses in the upper and bottom current surfaces.

2.2.1 Resistance

While propagating downstream, turbidity currents experience resistance from the bottom loose boundary and upper ambient fluid, which can be essentially quantified by the bed shear stresses τ_{bx} , τ_{by} and the shear stresses τ_{ux} , τ_{uy} in the upper interface. A brief review on resistance applied to turbidity currents can be found in Middleton (1966), which suggested that

$$\tau_{ux} = r_w \tau_{bx} \tag{2.12a}$$

$$\tau_{uy} = r_w \tau_{by} \tag{2.12b}$$

where r_w = empirical coefficient. Although the resistance in the upper interface was not considered in many models, a value of 0.43 for r_w was consistently used in others (e.g., Middleton 1966; Fukushima *et al*. 1985; Parker *et al*. 1986; Zeng and Lowe 1997a, b). By definition, the bed shear stresses are computed by

$$\tau_{bx} = \rho u_*^2 = c_D u U \tag{2.13a}$$

$$\tau_{by} = \rho v_*^2 = c_D v U \tag{2.13b}$$

where u_* and v_* = bed shear velocities in the *x*-direction and *y*-direction, c_D = bed drag coefficient. The estimation of the bed drag coefficient is critical as it determines the magnitude of the resistances that the current experiences. Physically, it should be carefully evaluated with reference to bed forms, bed textures, river geometry and other related factors. However, there seems to be no general relationships applicable for c_D in turbidity currents. A widely used practice is to assume a constant value to approximate the value of overall resistance, with its value in the range of [0.002, 0.06] suggested by Bowen *et al.*

(1984) and Parker *et al*. (1987). For large scale turbidity currents in the field, a small value should be used, and vice versa (Bradford and Katopodes 1999a, b).

There has also been an attempt to relate the bed drag coefficient to the turbulent energy and the mean energy of turbidity currents (Parker *et al.* 1986), which reads

$$c_D = \alpha \frac{k}{U^2} \tag{2.14}$$

where k = turbulent energy, α = coefficient. No physical meaning was suggested for the coefficient α, and a value of 0.1 was used in Parker *et al*. (1986). A conservation equation for the turbulent energy was proposed in Parker *et al.* (1986)

$$\frac{\partial hk}{\partial t} + \frac{\partial huk}{\partial x} = u_*^2 u + \frac{1}{2} u^3 e_w - \varepsilon_0 h - Rg\omega ch - \frac{1}{2} Rghuce_w - \frac{1}{2} Rgh(E - D) \tag{2.15}$$

with

$$\varepsilon_0 = \frac{0.5 e_w (1 - Ri - 2c_{D^*}/\alpha) + c_{D^*}}{(c_{D^*}/\alpha)^{3/2}}$$

where ω = sediment settling velocity, ε_0 = dissipation rate, c_{D^*} = bed drag coefficient under the equilibrium condition, $Ri = Rgch/U^2$ is the bulk Richardson number, which is the inverse square of the densimetric Froude number. The magnitude of Richardson number represents the current regime. The current is supercritical if Ri < 1.0, and vice versa

Eqs. (2.14-2.15) actually acts as a turbulent constraint on the bed drag coefficient and thus the sediment entrainment. The equations were introduced by Parker *et al*. (1986) due to the failure of a steady 1D decoupled Three-Equation-Model (TEM, see the model summary at the end of this chapter) to reproduce self-accelerating turbidity currents. In the TEM, the bed drag coefficient was set to be a constant. Parker *et al*. (1986) suggested that TEM overestimated the sediment entrainment, resulting in insufficient turbulent energy to sustain the entrained sediment. Although the incorporation of Eqs. (2.14) and (2.15) led to realistic solutions through the decoupled steady Four-Equation Model (FEM, see the model

summary at the end of this chapter), there are several aspects that remain unjustifiable. First, the failure of the TEM may be attributed to its nature of being decoupled (as steady flow is assumed, and feedback impacts of bed deformation are ignored). Second, the estimation of the sediment entrainment itself is subject to considerable uncertainty (Qian and Wan 1983; Fildani *et al*. 2006).

2.2.2 Mass exchange

While propagating downstream, mass exchange will occur in the lower and upper surface of turbidity current. Due to the upward decreasing trend of vertical sediment concentration profiles, sediment concentration around the upper current surface is usually very small. Thus only mass exchange of water is considered in the upper interface. By laboratory experiments and numerical experiments, water exchange in the upper interface has been demonstrated to be critical for the evolution of turbidity currents (Hallworth *et al.* 1993; Adduce *et al*. 2011) and has been quantified using the bulk Richardson number. Following Parker *et al.* (1986)

$$e_w = \frac{0.00153}{0.0204 + Ri} \tag{2.16}$$

In the bottom surface, mass exchange of sediment and water occurs at known ratio for a fully saturated bed once the sediment porosity is known. If it is assumed that the sediment porosity p = 0.4, the ratio is approximately 6:4. Therefore only the mass exchange of the sediment phase needs to be quantified, which constitutes a fundamental problem for sediment transport investigation (Qian and Wan 1983; Wu 2007). Sediment exchange between the current and the sediment bed involves two distinct mechanisms, i.e., sediment entrainment due to turbulence and sediment deposition due to gravitational action. There is little dispute in the literature that the sediment deposition should be set equal to the product of the sediment settling velocity and the near bed sediment concentration. While the mechanism for sediment entrainment by turbulence remains far from clear, the estimation of sediment entrainment is usually based on the assumption that the entrainment occurs at the same rate as it does under equilibrium conditions. The following equations have been

commonly used to estimate sediment entrainment and deposition fluxes for turbidity currents since Parker *et al*. (1986)

$$E = \omega E_s \tag{2.17a}$$

$$D = \omega c_b \tag{2.17b}$$

where E_s = sediment entrainment coefficient (alternatively, near-bed concentration at approximately capacity condition), $c_b = r_b c$ is the near-bed concentration, r_b = ratio of the near-bed concentration and the layer-averaged concentration. Note that for very fine sediment, high sediment concentration may hinder sediment settling (Qian and Wan 1983). This leads to a hindered settling velocity $\omega(1-c_b)$, yet it is not considered in this study following the common practice of using Eq. (2.17a, b) for turbidity currents (e.g., Parker *et al.* 1986; Imran et al. 1998; Bradford and Katopodes 1999a, b).

Evaluating the near-bed concentration at a distance of $0.05h$ from the bed surface, Parker *et al*. (1987) obtained the following approximate form

$$r_b = 1 + 31.5(\frac{U_*}{\omega})^{-1.46} \tag{2.18}$$

where $U_* = \sqrt{c_D}U$ is the overall bed shear velocity. Also laboratory experiments suggested that the value of r_b can be taken to be constant between 1.5 and 2.0 (Parker *et al.* 1987; Garcia 1993, 1994). While there have been a plethora of empirical formula to estimate the near-bed sediment concentration under capacity condition for sediment-laden open channel flows, for subaqueous turbidity currents, there seems to be only a family of empirical formulae for E_s. It was initially introduced by Parker *et al.* (1986) and later modified by Parker *et al.* (1987) and Garcia and Parker (1993) by experimental saline density currents. This formula is termed the Parker formula and reads

$$E_s = \psi_p \frac{1.3\times10^{-7} Z_m^5}{1+4.3\times10^{-7} Z_m^5} \tag{2.19a}$$

where $Z_m = R_{ep}^{0.5} U_* / \omega$, and $R_{ep} = \sqrt{Rgdd}/\nu$ is the particle Reynolds number, ν = 1E-6 m^2/s is the kinematic viscosity of water. If ψ_p = 1 the original Parker formula is retained. The correction coefficient ψ_p is introduced herein because the Parker formula is derived from experimental turbidity currents with relatively coarse sediments. For turbidity currents with silt and clay, Eq. (2.19a) may over-predict the sediment entrainment flux meaning that ψ_p < 1 for fine sediments (Fildani *et al*. 2006).

As a computational case study of turbidity currents in a real reservoir of the Yellow River is presented in Chapter 6, the Zhang formula, which is well tested and widely used for suspended sediment transport in open channel flows in the Yellow River (Zhang and Xie 1993), is also adapted by incorporating a correction coefficient ψ_z. Following the logarithmic-matching treatment of Guo (2002), it reads

$$E_s = \psi_z \frac{1}{20\rho_s} \frac{[U^3/gh\omega]^{1.5}}{1+[U^3/45gh\omega]^{1.15}} \tag{2.19b}$$

The introduction of the Zhang formula is based on the fact that sediment transport in the Yellow river is dominated by fine silt and clay, which may be not within the range of applicability of the Parker formula. It has been noted that the ratio of the actual sediment concentration of turbidity currents to that computed by capacity formulae of open channel flows in the Yellow River can attain a value as high as 34.5 (Han and Xiang 1981), indicating that the value of ψ_z would be much greater than unity.

The settling velocity is computed by the following empirical relation (Zhang and Xie 1993)

$$\omega = \sqrt{(13.95\frac{\nu}{d})^2 + 1.09Rgd} - 13.95\frac{\nu}{d} \tag{2.20}$$

In this thesis, the values of empirical parameters and coefficients are set according to the above descriptions unless otherwise stated.

2.3 Numerical Algorithm

Here the finite volume method is used to discretisize the governing equations. The SLIC scheme is used to compute numerical fluxes of the finite volume discretization. First, the 2D governing equations are written in a matrix form as follows

$$\frac{\partial \mathbf{U}}{\partial t}+\frac{\partial \mathbf{F}}{\partial x}+\frac{\partial \mathbf{G}}{\partial y}=\mathbf{S}_b+\mathbf{S}_f \tag{2.21}$$

with

$$\mathbf{U}=\begin{bmatrix} h \\ hu \\ hv \\ hc \end{bmatrix},\ \mathbf{F}=\begin{bmatrix} hu \\ hu^2+0.5g'h^2 \\ huv \\ huc \end{bmatrix},\quad \mathbf{G}=\begin{bmatrix} hv \\ huv \\ hv^2+0.5g'h^2 \\ hvc \end{bmatrix}$$

$$\mathbf{S}_b=\begin{bmatrix} 0 \\ g'hS_{bx} \\ g'hS_{by} \\ 0 \end{bmatrix},\ \mathbf{S}_f=\begin{bmatrix} E_w+(E-D)/(1-p) \\ -\dfrac{(\tau_{bx}+\tau_{ux})}{\rho}-R_wE_wu-R_0\dfrac{E-D}{1-p}u \\ -\dfrac{(\tau_{by}+\tau_{uy})}{\rho}-R_wE_wv-R_0\dfrac{E-D}{1-p}v \\ E-D \end{bmatrix}$$

where $\mathbf{U}$ = vector of the conservative variables, $\mathbf{F}$, $\mathbf{G}$ = vectors of fluxes, $\mathbf{S}_b$, $\mathbf{S}_f$ = vectors of source terms.

2.3.1 FVM discretization

Figure 2.2 shows a sketch of a square control volume Ω bounded by the four sides $L=[l_1,l_2,l_3,l_4]$. The integral form of Eq. (2.21) in the control volume is

$$\int_\Omega \frac{\partial \mathbf{U}}{\partial t}d\Omega+\int_\Omega\left(\frac{\partial \mathbf{F}}{\partial x}+\frac{\partial \mathbf{G}}{\partial y}\right)d\Omega=\int_\Omega(\mathbf{S}_b+\mathbf{S}_f)d\Omega \tag{2.22}$$

Applying Green's theorem, Eq. (2.22) becomes

$$\int_{\Omega} \frac{\partial \mathbf{U}}{\partial t} d\Omega + \oint_{L} (\mathbf{E} \cdot \mathbf{n}) dl = \int_{\Omega} (\mathbf{S}_b + \mathbf{S}_f) d\Omega \tag{2.23}$$

where $\mathbf{E} = (\mathbf{F}, \mathbf{G})$, $\mathbf{n}$ = outward unit vector normal to L. Consider the Cartesian grid system as sketched in Figure 2.2, a cell-averaged value is defined as

$$\bar{a} = \frac{1}{A} \int_{\Omega} a d\Omega \tag{2.24}$$

where a = parameter, $A = \Delta x \Delta y$ is the area of a computational cell, Δx and Δy = spatial steps in the x - and y -directions, the upper bar $\bar{}$ means cell-averaged. Therefore Eq. (2.23) can be rewritten as

$$A \frac{\overline{\mathbf{U}}^{n+1} - \overline{\mathbf{U}}^{n}}{\Delta t} = -\sum_{k=1}^{4} \mathbf{E}_k \cdot \mathbf{n}_k dl_k + A(\overline{\mathbf{S}_b} + \overline{\mathbf{S}_f}) \tag{2.25}$$

where the upper script n denotes the time step index. In descriptions below, the upper bar $\bar{}$ is removed for simplicity. Consider an arbitrary cell (i, j), its four sides, an explicit updating algorithm for $\mathbf{U}_{i,j}$ reads

$$\mathbf{U}_{i,j}^{*} = \mathbf{U}_{i,j}^{n} - \frac{\Delta t(\mathbf{F}_{i+1/2,j} \Delta y - \mathbf{F}_{i-1/2,j} \Delta y + \mathbf{G}_{i,j+1/2} \Delta x - \mathbf{G}_{i,j-1/2} \Delta x)}{\Delta x \Delta y} + \Delta t \mathbf{S}_{bi,j}(\mathbf{U}^{*}) \tag{2.26a}$$

$$\mathbf{U}_{i,j}^{n+1} = \mathbf{U}_{i,j}^{*} + \Delta t \mathbf{S}_f(\mathbf{U}^{*}) \tag{2.26b}$$

where the subscripts i and j = the spatial node indexes, $\mathbf{F}_{i+1/2,j}$, $\mathbf{F}_{i-1/2,j}$, $\mathbf{G}_{i,j+1/2}$, $\mathbf{G}_{i,j-1/2}$ are the inter cell numerical fluxes at the four sides of the cell. The time step should be constrained by the CFL condition,

$$Cr = \Delta t \left(\frac{\lambda_{x\max}}{\Delta x} + \frac{\lambda_{y\max}}{\Delta y} \right) < 1 \tag{2.27}$$

where Cr = Courant number, $\lambda_{x\max}$, $\lambda_{y\max}$ = maximum celerities of the Jacobian matrixes $\partial \mathbf{F}/\partial \mathbf{U}$ and $\partial \mathbf{G}/\partial \mathbf{U}$ respectively.

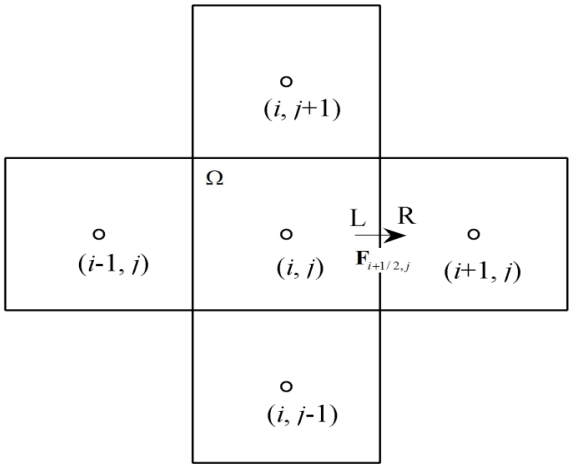

Figure 2. 2 Sketch for the finite volume method.

The bed deformation equation is solved independently from other governing equations. It is discretisized in the control volume by first order discretization,

$$\frac{z_{i,j}^{n+1} - z_{i,j}^{n}}{\Delta t} = \frac{(D-E)_{i,j}^{*}}{(1-p)} \tag{2.28}$$

In this study a second-order discretization has also been applied to the bed deformation equation. Yet numerical comparisons suggest that the difference between the first order method Eq. (2.28) and the second order method is negligible, thus the first-order discretization Eq. (2.28) is presented.

2.3.2 SLIC scheme

The SLIC scheme is used to compute numerical fluxes in Eq. (2.26a), which is total variation diminishing (TVD) and can capture automatically shock waves and contact

discontinuities (Toro 2001). The use of this SLIC follows the suggestion of Prof. Toro (Hu and Cao 2009). The SLIC scheme treats the evaluation of a numerical flux as a Riemann problem. Two states are required for a Riemann problem, i.e., a left state and a right state in the two sides of the edge. Take the edge $x = x_{i+1/2,j}$ between the cell (i, j) and $(i+1, j)$ as an example. The simplest way is to use $\mathbf{U}_{i,j}^{n}$ and $\mathbf{U}_{i+1,j}^{n}$ (cell-averaged variables) as the left and right state variables, which are spatially and temporally only first order accurate. To achieve the second order accurate both spatially and temporally, three steps are involved in the SLIC scheme. The first step aims to achieve spatially second order accuracy. In this step, the left and right state variables of the edge of the two neighbouring cells are interpolated from the cell averaged variables. The second step aims to achieve temporally second order accuracy, which is accomplished by evolution of the interpolated left and right state variables over a half time step. The third step involves the computation of the numerical flux using the evolved left and right state variables.

In this study two versions of the SLIC scheme are introduced, which differ from each other in the reconstruction of the left and right current thickness in the first step. The first one refers to the conventional SLIC scheme, termed Depth Gradient Method (DGM), which uses the spatial gradients of the current thickness. The second one is a revised version, referred to as Weighted Surface Depth Gradient Method (WSDGM), which uses the spatial gradients of both the current thickness and the upper current surface elevation.

With the DGM, the SLIC scheme is robust and stable with small current depth gradients (water depth gradients for shallow water flows) and large current surface gradients typical of regular bed topography. However, for practical situations, bed topographies are usually irregular, which favour large current thickness gradients. In this case, the DGM version of the SLIC scheme does not always permit stable solutions (e.g., Zhou *et al*. 2001; Aureli *et al*. 2008; Liang and Marche 2009), essentially because the source terms and the flux gradients are not balanced, i.e., the C-property is not satisfied. Satisfying the C-property for TVD schemes is critical for practical applications. It is because the application of a TVD scheme that is not well-balanced may produce considerable numerical errors for flows over irregular topographies. In this regard, many well-balanced schemes have been developed (e.g., Hubbard and Garcia-Navarro 2000; Zhou *et al*. 2001; Rogers *et al*. 2003; Rosatti and

Fraccarollo 2006; Aureli *et al*. 2008; Liang and Marche 2009). Zhou *et al*. (2001) proposed the Surface Gradient Method (SGM). While SGM is applicable for currents over irregular topography, it may produce physically unrealistic results over regular bed topography (Aureli *et al*. 2008). Retaining the good capabilities of both DGM and SGM, Aureli *et al*. (2008) have developed the well balanced WSDGM version of the SLIC scheme. Inspired by the need for effective sediment management using turbidity currents and the highly irregular topography in the field, the WSDGM by Aureli *et al*. (2008) version of the SLIC scheme for shallow clear water equations will be extended for modelling turbidity currents over irregular mobile topography. Although the WSDGM by Aureli *et al.* (2008) is limited to irregular fixed beds, the present extension is justified as the bed deformation equation is solved separately from other governing equations. The three steps of the SLIC scheme are introduced below.

Step 1: Spatially second-order accuracy and data interpolation

From above, the primary difference between the DGM and the WSDGM lies in the first step of data interpolation. A new vector of variables is introduced so that the DGM and WSDGM can be distinguished clearly.

$$\mathbf{Q} = \begin{bmatrix} 0 & hu & hv & hc & h & \eta \end{bmatrix}^{\prime} \tag{2.29}$$

where $\eta = h + z$ is the current surface elevation. Setting the first component to vanish here, it will be updated later using the fifth and sixth components in order to obtain different versions of the SLIC scheme. The inter-cell variables $\mathbf{Q}^{L}_{i+1/2,j}$ and $\mathbf{Q}^{R}_{i+1/2,j}$ at the left and right of the inter-cell edge $x = x_{i+1/2}$ are reconstructed as follows

$$\mathbf{Q}^{L}_{i+1/2,j} = \mathbf{Q}^{n}_{i,j} + \boldsymbol{\varphi}^{L}_{i-1/2,j} \frac{\mathbf{Q}^{n}_{i,j} - \mathbf{Q}^{n}_{i-1,j}}{2} \tag{2.30a}$$

$$\mathbf{Q}^{R}_{i+1/2,j} = \mathbf{Q}^{n}_{i+1,j} - \boldsymbol{\varphi}^{R}_{i+3/2,j} \frac{\mathbf{Q}^{n}_{i+2,j} - \mathbf{Q}^{n}_{i+1,j}}{2} \tag{2.30b}$$

where the vector $\boldsymbol{\varphi}$ = slope limiter. The slope limiter is introduced to constrain the magnitude of the differences between the cell-averaged variables and the inter-cell variables. This constraint is to avoid spatial irregularities in the constructed inter-cell variables, so that the scheme is total variation diminishing, which is an important indicator of the robustness of the numerical algorithm (Toro 2001). Many slope limiters have been introduced for TVD schemes, which are all a function of the ratio vector $\mathbf{r}$ of consecutive variations of the conservative variable $\mathbf{Q}$. The vector $\mathbf{r}$ is defined as

$$\mathbf{r}^{L}_{i-1/2,j} = \frac{\mathbf{Q}^{n}_{i+1,j} - \mathbf{Q}^{n}_{i,j}}{\mathbf{Q}^{n}_{i,j} - \mathbf{Q}^{n}_{i-1,j}} \tag{2.31a}$$

$$\mathbf{r}^{R}_{i+3/2,j} = \frac{\mathbf{Q}^{n}_{i+1,j} - \mathbf{Q}^{n}_{i,j}}{\mathbf{Q}^{n}_{i+2,j} - \mathbf{Q}^{n}_{i+1,j}} \tag{2.31b}$$

The VanLeer Limiter is introduced below following Aureli *et al.* (2008)

$$\boldsymbol{\varphi}(\mathbf{r}) = \begin{cases} \dfrac{\mathbf{r} + |\mathbf{r}|}{1 + \mathbf{r}} & \mathbf{r} > 0 \\ 0 & \mathbf{r} \le 0 \end{cases} \tag{2.32}$$

The first components of the reconstructed left and right states are updated as follows

$$\mathbf{Q}^{L}_{i+1/2,j}(1) = \phi[\mathbf{Q}^{L}_{i+1/2,j}(5)] + (1-\phi)[\mathbf{Q}^{L}_{i+1/2,j}(6) - z_{i+1/2,j}] \tag{2.33a}$$

$$\mathbf{Q}^{R}_{i+1/2,j}(1) = \phi[\mathbf{Q}^{R}_{i+1/2,j}(5)] + (1-\phi)[\mathbf{Q}^{R}_{i+1/2,j}(6) - z_{i+1/2,j}] \tag{2.33b}$$

with

$$z_{i+1/2,j} = \frac{z_{i,j} + z_{i+1,j}}{2}$$

where ϕ = weighting factor, $z_{i+1/2}$ = inter cell bed elevation. After updating, the following are obtained

$$\mathbf{U}^{L}_{i+1/2,j} = [\mathbf{Q}^{L}_{i+1/2,j}(1), \mathbf{Q}^{L}_{i+1/2,j}(2), \mathbf{Q}^{L}_{i+1/2,j}(3), \mathbf{Q}^{L}_{i+1/2,j}(4)] \tag{2.34a}$$

$$\mathbf{U}^{R}_{i+1/2,j} = [\mathbf{Q}^{R}_{i+1/2,j}(1), \mathbf{Q}^{R}_{i+1/2,j}(2), \mathbf{Q}^{R}_{i+1/2,j}(3), \mathbf{Q}^{R}_{i+1/2,j}(4)] \tag{2.34b}$$

Step 2: Temporally second-order accuracy and evolution of inter cell variables

The interpolated inter-cell variables are further evolved over a half time step as follows

$$\begin{aligned}\overline{\mathbf{U}}^{L}_{i+1/2,j} = \mathbf{U}^{L}_{i+1/2,j} &- \frac{\Delta t/2}{\Delta x}[\mathbf{F}(\mathbf{U}^{L}_{i+1/2,j}) - \mathbf{F}(\mathbf{U}^{R}_{i-1/2,j})] \\ &- \frac{\Delta t/2}{\Delta y}[\mathbf{G}(\mathbf{U}^{L}_{i,j+1/2}) - \mathbf{G}(\mathbf{U}^{R}_{i,j-1/2})] + \frac{\Delta t}{2}\mathbf{S}_{bi,j}\end{aligned} \tag{2.35a}$$

$$\begin{aligned}\overline{\mathbf{U}}^{R}_{i+1/2,j} = \mathbf{U}^{R}_{i+1/2,j} &- \frac{\Delta t/2}{\Delta x}[\mathbf{F}(\mathbf{U}^{L}_{i+3/2,j}) - \mathbf{F}(\mathbf{U}^{R}_{i+1/2,j})] \\ &- \frac{\Delta t/2}{\Delta y}[\mathbf{G}(\mathbf{U}^{L}_{i+1,j+1/2}) - \mathbf{G}(\mathbf{U}^{R}_{i+1,j-1/2})] + \frac{\Delta t}{2}\mathbf{S}_{bi+1,j}\end{aligned} \tag{2.35b}$$

with

$$\mathbf{S}_{bi,j} = \begin{bmatrix} 0 \\ -\dfrac{g'_{i+1/2,j}(h^{L}_{i+1/2,j} + h^{R}_{i-1/2,j})(z_{i+1/2,j} - z_{i-1/2,j})}{2\Delta x} \\ -\dfrac{g'_{i,j+1/2}(h^{L}_{i,j+1/2} + h^{R}_{i,j-1/2})(z_{i,j+1/2} - z_{i,j-1/2})}{2\Delta y} \\ 0 \end{bmatrix}$$

$$g'_{i+1/2,j} = \frac{g'_{i,j} + g'_{i+1,j}}{2}$$

The inter cell current thickness $h^L_{i+1/2,j}$ and $h^R_{i+1/2,j}$ = first components of $\mathbf{U}^L_{i+1/2,j}$ and $\mathbf{U}^R_{i+1/2,j}$.

Step 3: The Riemann problem (numerical flux estimation)

At the interface $x_{i+1/2,j}$, a pair of constant states ($\overline{\mathbf{U}}^L_{i+1/2,j}, \overline{\mathbf{U}}^R_{i+1/2,j}$) has been obtained from the above two steps. One can now solve the estimate the numerical flux using the FORCE approximate Riemann solver, which is essentially a weighted combination of the Lax-Friedrichs flux and the two-step Lax-Wendroff flux. Therefore (Toro 2001; Toro *et al.* 2009)

$$\begin{aligned}\mathbf{F}_{i+1/2,j} &= \mathbf{F}^{FORCE}(\overline{\mathbf{U}}^L_{i+1/2,j}, \overline{\mathbf{U}}^R_{i+1/2,j}) \\ &= \frac{1}{2}[\mathbf{F}^{LF}(\overline{\mathbf{U}}^L_{i+1/2,j}, \overline{\mathbf{U}}^R_{i+1/2,j}) + \mathbf{F}^{LW2}(\overline{\mathbf{U}}^L_{i+1/2,j}, \overline{\mathbf{U}}^R_{i+1/2,j})]\end{aligned} \tag{2.36}$$

where $\mathbf{F}^{FORCE}$, $\mathbf{F}^{LF}$ and $\mathbf{F}^{LW2}$ = FORCE flux, Lax-Friedrichs flux and two-step Lax-Wendroff flux, respectively. The Lax-Friedrichs flux and the two-step Lax-Wendroff flux are estimated as follows

$$\mathbf{F}^{LF}_{i+1/2,j} = \frac{1}{2}[F(\overline{\mathbf{U}}^L_{i+1/2,j}) + F(\overline{\mathbf{U}}^R_{i+1/2,j})] - \frac{1}{2}\frac{\Delta x}{\beta \Delta t}(\overline{\mathbf{U}}^R_{i+1/2,j} - \overline{\mathbf{U}}^L_{i+1/2,j}) \tag{2.37}$$

$$\mathbf{F}^{LW}_{i+1/2,j} = \mathbf{F}(\mathbf{U}^{LW}_{i+1/2,j}) \tag{2.38a}$$

$$\mathbf{U}^{LW}_{i+1/2,j} = \frac{1}{2}(\overline{\mathbf{U}}^L_{i+1/2,j} + \overline{\mathbf{U}}^R_{i+1/2,j}) - \frac{1}{2}\frac{\beta \Delta t}{\Delta x}(\mathbf{F}(\overline{\mathbf{U}}^R_{i+1/2,j}) - \mathbf{F}(\overline{\mathbf{U}}^L_{i+1/2,j})) \tag{2.38b}$$

Eqs. (2.32) and (2.33) include a parameter β, denoting the dimension of the model: β = 1 for 1D model, β = 2 for 2D model (Toro *et al*. 2009). The evaluation of the FORCE flux is written in relation to the x-direction. Those in the y-direction can be computed similarly.

DGM vs. WSDGM

As mentioned above, the DGM and the WSDGM differ from each other in the first step, which is mathematically defined by the weighting factor ϕ in Eq. (2.33). For DGM, ϕ =1. For WSDGM, ϕ is a function of the bulk Richardson number which allows smooth transition between a pure SGM reconstruction (ϕ = 0.0) and an essentially DGM reconstruction (ϕ = 1.0). By analogy to Aureli *et al*. (2008), it is determined by

$$\phi = \begin{cases} 0.5[1-\cos(\frac{\pi Ri_{\lim}}{Ri})] & Ri > Ri_{\lim} \\ 1 & Ri < Ri_{\lim} \end{cases} \tag{2.39}$$

2.3.3 Wetting and drying

The treatment of the wetting and drying is critical for the successful modelling of turbidity currents. The method proposed by Zhao *et al*. (1994) is employed here, which has been widely used (Imran *et al*. 1998; Bradford and Katopodes 1999a, b). Two neighbouring cells will be defined as a wet/dry front if one cell of the two is wet and the other is dry (Figure 2.3). In Figure 2.3, $h_{\lim}$ is a threshold current thickness, which is used to judge whether a cell is wet or not. A sufficiently small value (irrespective of the grid sizes/spatial steps in the computation) of threshold current thickness is used throughout the present study: $h_{\lim}$= 1E-6 m. With reference to Figure 2.3, considering two neighbouring cells i and $i+1$, for which one is wet $h_i \geq h_{\lim}$ and the other is dry $h_{i+1} < h_{\lim}$:

If $z_i > \eta_{i+1}$, then $z_{i+1} = z_i$ and $h_{i+1} = h_{\lim}$ (Figure 2.3a)

If $\eta_i < \eta_{i+1}$, then $z_{i+1} = \eta_i$ and $h_{i+1} = 0$ (Figure 2.3b)

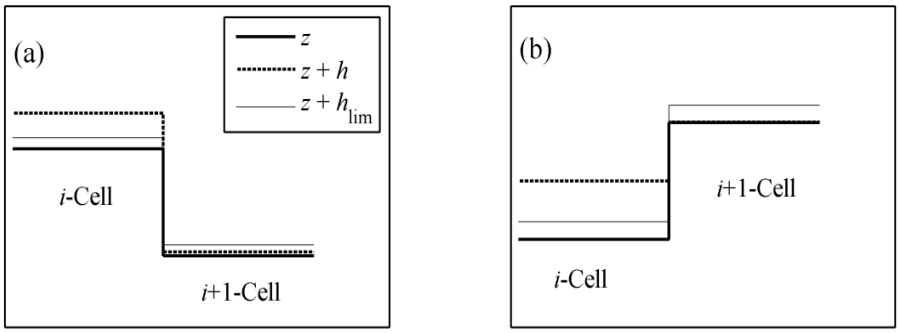

Figure 2. 3 Sketch for the wet/dry front.

2.4 Model Summary

The governing equations presented above are based on the complete layer-averaged mass and momentum conservation laws. While existing mathematical models are exclusively based on simplified versions, the present model advances modelling capability of turbidity currents in that the complete governing equations are used and thus the interactions between the current evolution, sediment transport and morphological change are explicitly considered. Therefore the present model is termed a fully coupled model. In contrast, previous models are classified into decoupled models or partially coupled models. In decoupled models, the variations to bed topography by the currents are neglected completely, i.e., there is no bed deformation equation involved in decoupled models, e.g., the 1D steady models by Fukushima *et al*. (1985), Parker *et al*. (1986) and Sequeiros *et al*. (2009a). In partially coupled models, morphological changes are tracked using the bed deformation equation, yet the feedback impacts of bed deformation on the current evolutions are ignored. Take the 2D governing equations as an example, the last terms in the Right-Hand-Side (RHS) of Eqs. (2.7), (2.8) and (2.9) are neglected. Partially coupled models include Bonnecaze *et al*. (1995), Zeng and Lowe (1997a, b), Choi (1998, 1999), Imran *et al*. (1998), Bradford and Katopodes (1999a, b) and Fildani *et al*. (2006). Mathematically, these source terms are simple algebraic functions of unknown variables as presented in **Section 2.2 Auxiliary Relationships**, and essentially their inclusion incurs negligible extra computational cost.

Decoupled models and partially coupled models may be applicable to turbidity currents with weak sediment transport and mild bed deformation when the interactions between the turbidity currents, sediment transport and topography are negligible. However, it is those turbidity currents featuring active sediment transport and rapid bed deformation that are of practical interest and are responsible for reservoir sedimentation, the formation of submarine turbidites and morphological features. For these turbidity currents, interactions may be considerable and accordingly fully coupled modelling is critical for high quality modelling. The significance of fully coupled modelling and its comparison with decoupled or partially coupled modelling will be examined in detail in Chapter 4.

A summary of models that are to be referred to is presented in Table 2.1.

Table 2. 1 Model Summary

Model	Remarks
FCM	Presently proposed fully coupled models The interactions between the turbidity current, sediment transport and topography are explicitly considered
PCM	Partially coupled models in literature (e.g., Bonnecaze *et al*. 1995; Zeng and Lowe 1997a, b, Choi 1998, 1999, Imran *et al*. 1998, Bradford and Katopodes 1999a, b and Fildani *et al*. 2006) Bed deformation is considered, yet its feedback impacts are ignored
TEM	Three equation model by Fukushima *et al*. (1985) and Parker *et al.* (1986) No bed deformation at all Steady flow assumption
FCMK	Based on FCM, PCM, and TEM respectively, yet the bed drag coefficient is estimated using the turbulent energy conservation Eqs. (2.14) and (2.15)
PCMK	
FEM	

Finally, in the literature there has been comment that layer-averaged models implicitly assume sediment as a passive constituent (Parsons *et al*. 2007). This is misleading for turbidity currents. It might be true for decoupled or partially coupled models of open channel sediment-laden flow. However, for the present coupled model of turbidity currents, the impacts of sediment transport on the flow or current evolution have to be fully considered. More importantly, it is the presence of the sediment that gives a density excess and thus provides the driving force for the turbidity currents, as reflected in the source term of the momentum conservation (say, $-RgchB\partial z/\partial x$ in the x-direction). The higher the sediment concentration, the larger the driving force would be. The most telling case is self-accelerating turbidity currents, for which sediment entrainment increases the driving force that propels a faster current, which in turn causes more sediment entrainment (Fukushima *et al*. 1985; Parker *et al*. 1986). Sediment in turbidity currents is therefore an active constituent, irrespective of decoupled or coupled layer-averaged models.

While the governing equations are presented for both 1D and 2D conditions, the numerical algorithm is presented with regard to the 2D governing equations. A 1D coupled model was developed originally using the DGM version of the SLIC scheme, which is applicable only to regular beds. The imbalanced 1D coupled model was applied to investigate the hyperconcentrated turbidity currents by Hallworth and Huppert (1998) in Section 3.4, and the self-accelerating turbidity currents representative of those occurring in the Submarine Scripps Canyon in Chapter 4. The 1D model was later extended to the 2D situation and made well-balanced for the investigation of the effects of submarine turbidity currents on submarine morphological evolution in Chapter 5 and the reservoir turbidity currents for effective reservoir sediment management in Chapter 6. Nevertheless, the hyperconcentrated turbidity currents by Hallworth and Huppert (1998) and the self-accelerating turbidity currents have been revisited by the well-balanced 2D coupled model, of which the numerical solutions are almost the same as those by the 1D coupled model. Therefore, in presenting the research work in the following chapters, no distinction is made between the 1D and 2D models.

Chapter 3. MODEL PERFORMANCE

Summary

- Accuracy of the fully coupled model is demonstrated against experimental data.
- Ability of the model to handle both subcritical and supercritical current regimes is demonstrated
- Ability of the model to deal properly with irregular topography is demonstrated

Tests of the fully coupled model are presented in this chapter. Special attention is paid to the ability of the model to properly deal with irregular topography (so that it is applicable to turbidity currents in the field) and capture shock waves (i.e., interchange between subcritical and supercritical current regimes). Moreover, the accuracy of the model is examined in terms of morphological change, current front propagation and position of the current surface.

These tests are necessary before the model is used for application and research purposes. Nevertheless, it does not necessarily mean that the empirical model parameters used in this chapter are generic for all conditions. For different conditions, the empirical parameters should be calibrated and validated as necessary.

3.1 Well-balanced Property

The well-balanced property, i.e., the C-property, is associated with the capability of the model to preserve static water conditions over an irregular topography. Although the Godunov-type finite volume method can capture shock waves and discontinuities well and be easily adapted to deal with wet/dry fronts, it has been widely recognized that achieving

the well-balanced property is not straightforward (e.g., Bermudez and Vazquez 1994; Hubbard and Garcia-Navarro 2000; Zhou *et al*. 2001; Rogers *et al*. 2001, 2003; Aureli *et al*. 2008; Liang and Marche 2009; Serrano-Pacheco *et al*. 2009). The well-balanced property of the present model is achieved by using the WSDGM version of the SLIC scheme (see the section of numerical algorithm in Chapter 2). The satisfaction of this property is tested in this section.

A hypothetical 1D test case is proposed to examine the well-balanced property of the fully coupled model. Figure 3.1 shows the sketch of the idealized case. As seen in Figure 3.1, a layer of initially static turbidity layer (grey) is imposed over a hump of Gaussian shape (black) in an 8.0 m long tank. Above the turbidity layer is a layer of clear water (white). The shape of the hump is defined by $z = 0.24\exp[-50(x - 4.0)^2]$ m. At t = 0 (s), the interface elevation η = 0.4 m, and the sediment concentration in the turbidity layer is 0.04. In this case, it is assumed that the turbidity layer is vertically well mixed as it settles out. Although this case is idealized, it does have engineering background, see for example Toniolo *et al.* (2007), which presented an investigation of the natural settling process of ponded turbidity currents.

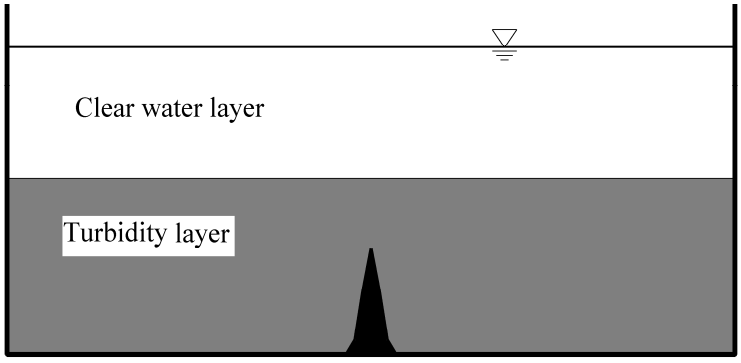

Figure 3. 1 Sketch of idealized test case

It is physically reasonable to expect that the initially static turbidity volume in Figure 3.1 would preserve its static status as the sediment settles. Both the DGM and the WSDGM are applied to facilitate comparison. Based on grid-convergence tests, Δx = 0.2 m and Cr = 0.95 are applied.

The numerical solutions are presented in Figure 3.2 for the model using the WSDGM and in Figure 3.3 for the model using the DGM: (a, b) shows bed elevation z and turbidity surface elevation η at t = 25 (s) and 100 (s) respectively, (c) shows sediment storage hc at two instants, and (d) shows current discharge hu at two instants. It is seen from Figure 3.2 that when WSDGM is used, the initial static condition is preserved satisfactorily: no horizontal advection (Figure 3.2d), no oscillation in the turbidity surface elevation (Figure 3.2a, b) when the sediment settles (Figure 3.2c). In contrast, when the DGM is used (Figure 3.3), appreciable horizontal advection is computed with an order of magnitude of 0.005 in terms of the current discharge, see Figure 3.3(d) and considerable fluctuations of the turbidity surface elevation are observed (Figure 3.3a, b).

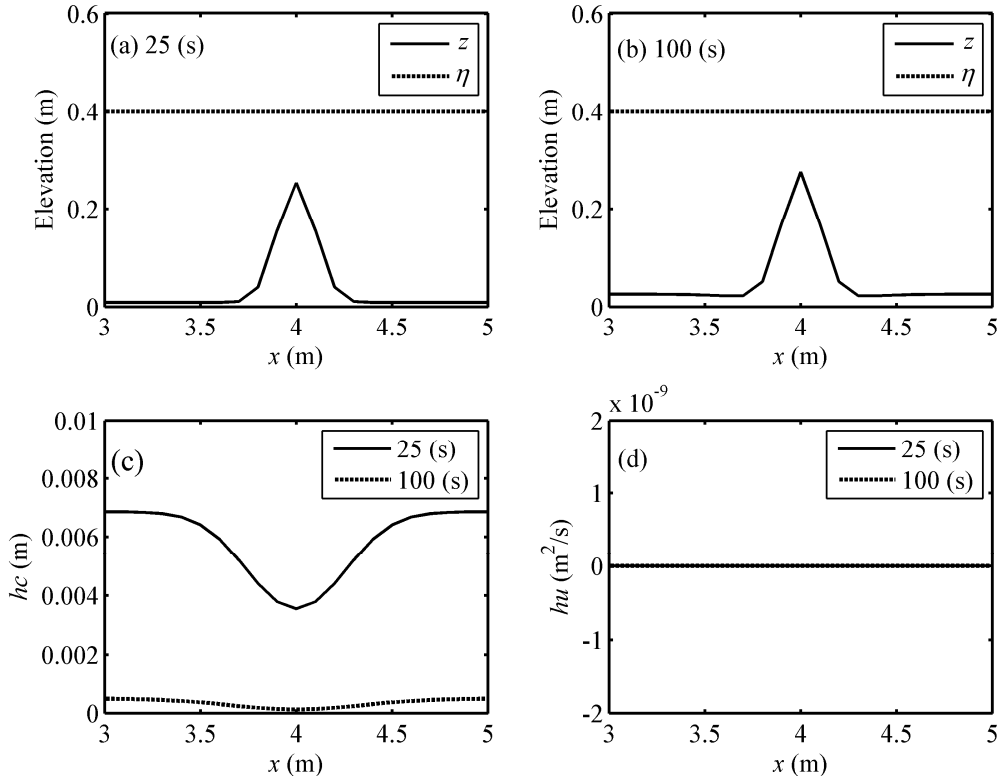

Figure 3. 2 Numerical solutions from the well-balanced model (WSDGM is applied): (a, b) bed elevation z and current surface elevation η, (c) sediment storage hc, and (d) current discharge hu.

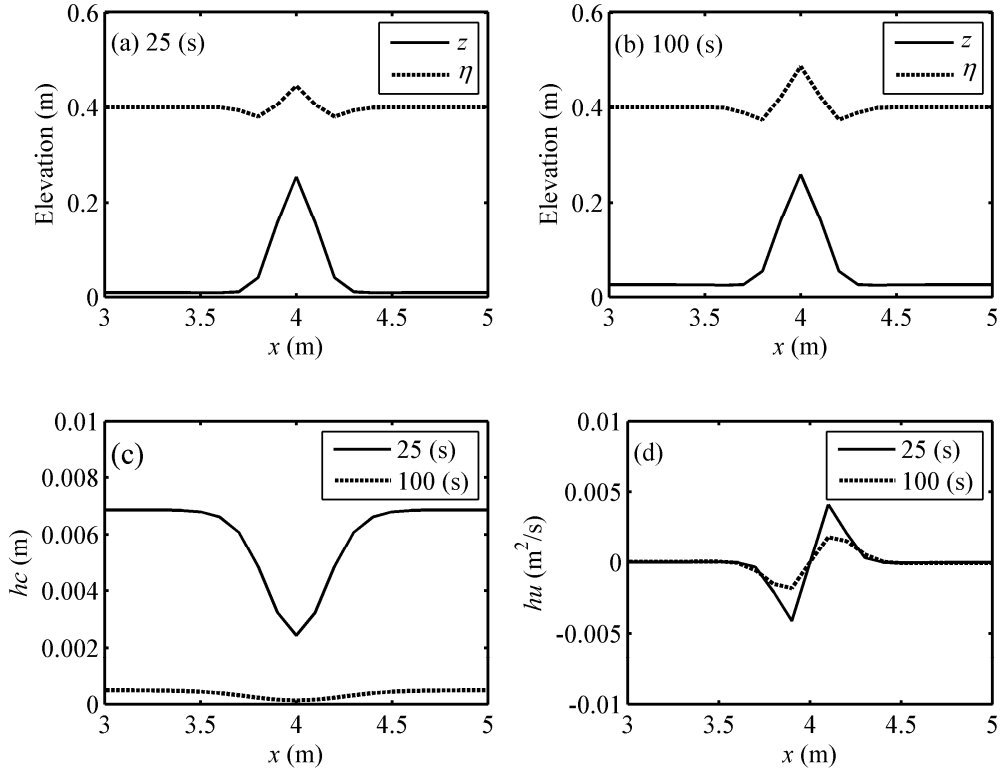

Figure 3. 3 Numerical solutions from the imbalanced model (DGM is applied): (a, b) bed elevation z and current surface elevation η, (c) sediment storage hc, and (d) current discharge hu.

A slight horizontal sediment concentration gradient around the hump is noted in Figs. 3.2(c) and 3.3(c), which can be ascribed to the different times needed for sediment settling around hump (with different depth). As the driving force of turbidity current comes from the density difference, this slight spatial gradient may induce some horizontal advection, which may indicate that the horizontal advection in Figure 3.3(d) is correct. To avoid this confusion, numerical exercises have been conducted, in which the sediment concentration is set to be constant (= the initial sediment concentration). It has been observed that the DGM still produces appreciable horizontal advection and oscillation in the turbidity surface elevation and the WSDGM preserves the static condition satisfactorily. The numerical results are similar to Figs. (3.2) and (3.3), thus they are not included in the thesis.

The above observations suggest that if the WSDGM version of SLIC is applied, the fully coupled model is well-balanced and thus should be applicable to turbidity currents over

irregular topographies. Moreover, if the WSDGM is applied, models listed in Table 2.1 are essentially well-balanced. The differences among these models lie in physical processes considered.

3.2 Experimental Turbidity currents with an Internal Hydraulic Jump

Around a slope reduction in topography, supercritical turbidity currents may change to become subcritical through an internal hydraulic jump. The occurrence of internal hydraulic jumps for turbidity currents has been confirmed by the analysis of field observed deposition (Weirich 1988), laboratory experiments (Garcia and Parker 1989; Garcia 1993, 1994) and also theoretically supported by the hyperbolic nature of the governing equations (Toro 2001). This fact necessitates numerical models of turbidity currents that are capable of capturing shock waves and contact discontinuities. It is accomplished in this thesis by using the SLIC scheme in the framework of the finite volume method.

The experimental work by Garcia and Parker (1989) and Garcia (1993, 1994) on turbidity currents with internal hydraulic jumps provides a good data set to test of the fully coupled model. A 11.6 m long flume was constructed to resemble the slope break, which consists of a sloping bed 5 m long with a slope of S_{bx} = 0.08 in the upstream part, followed by a horizontal bed of 6.6 m long. Two experimental runs are numerically simulated by the present model: GLASSA2 with well sorted sediment reported in Garcia (1993) and MIX1 with poorly sorted sediment reported in Garcia (1994). Following Garcia (1993), the following parameters are specified: p = 0.5, ρ_s = 2650 kg/m^3, r_b = 2.0. The bed drag coefficient for GLASSA2 is specified following Imran *et al*. (1998): c_D = 0.01, and that for MIX1 following Garcia (1994): c_D = 0.025. The inlet current thickness h_0 = 0.03 m for both runs. Other parameters are summarized in Table 3.1, including the inlet current velocity u_0, the inlet sediment concentration c_0, the representative particle diameter d_r and the experimental temperature. From Table 3.1, it is easy to see that the inlet current is supercritical, thus at the upstream boundary the current variables are specified directly. At the downstream boundary, the critical current condition is used: $Ri = 1$, because the free outfall condition is designed there (Garcia 1993, 1994). In the computation, the sediment

entrainment is set to be zero following Garcia (1994) because the flume bed is free of sediment. Numerical exercises with spatial steps ranging from 0.005 m to 0.5 m were conducted. Grid-convergence tests showed that a spatial step less than 0.1 m permits essentially the same numerical solutions. A spatial step of 0.025 m is used and Cr = 0.95.

Table 3. 1 Parameters for Garcia's experiments

Run	u_0	c_0	d_r	Temperature
GLASSA2	0.083 m/s	0.00339	30	25^{o}C
MIX1	0.11 m/s	0.0109	27	5^{o}C

Figs. 3.4 and 3.5 illustrate the numerical solutions and the available experimental data for MIX1 and GLASSA2 respectively, including (a) bed elevation and current surface elevation, (b) deposit thickness, (c) current velocity and (d) Richardson number. An internal hydraulic jump is computed for MIX1 (Figure 3.4), whereas no internal hydraulic jump occurs for GLASSA2 (Figure 3.5). Around the location x = 5 m for the internal hydraulic jump of MIX1, abrupt increases in the current surface elevation and Richardson number as well as decrease in the current velocity can be seen (Figure 3.4a, c, d). No signal of internal hydraulic jump can be identified for GLASSA2 in Figure 3.5. These are consistent with the descriptions in Garcia and Parker (1989) and Garcia (1993, 1994).

The deposition thickness for MIX1 appears to be overestimated by the fully coupled model for x < 4 m (Figure 3.4b). This is understandable because MIX1 used graded sediment mixtures (Garcia 1993, 1994), whereas the present model is limited to uniform sediment transport. Nevertheless, satisfactory agreement is obtained between the computed and measured deposition thickness for the uniform sediment run GLASSA2 (Figure 3.5b). Furthermore, the computed current surface position for MIX1 compares satisfactorily with the experimental data (Figure 3.4a).

MIX1 and GLASSA2 are reasonably resolved. The present model provides a useful tool for investigating internal hydraulic jump for turbidity current.

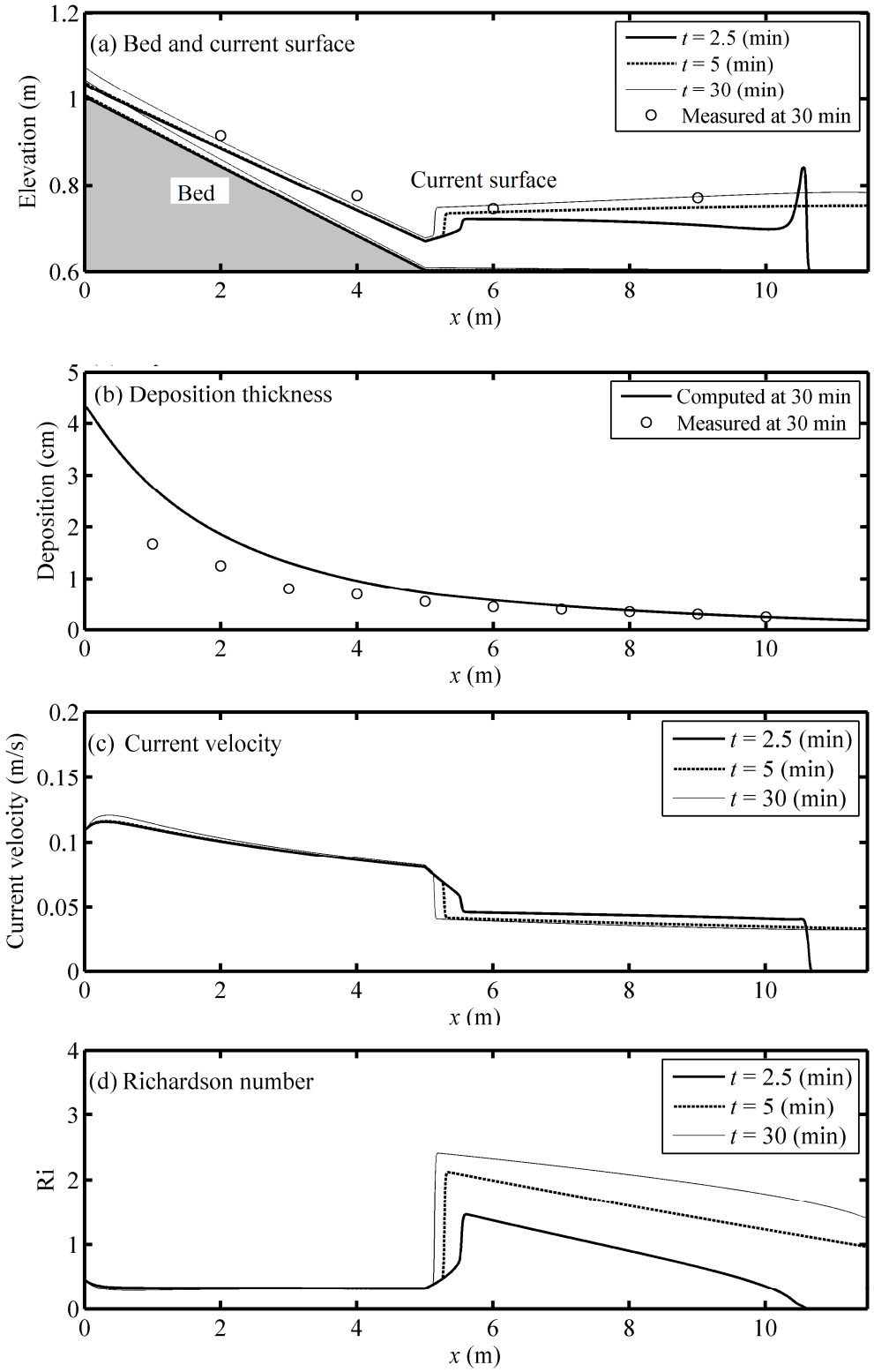

Figure 3. 4 Numerical solutions and measured data for MIX1 (a) bed and current surface, (b) deposition thickness, (c) current velocity, (d) Richardson number.

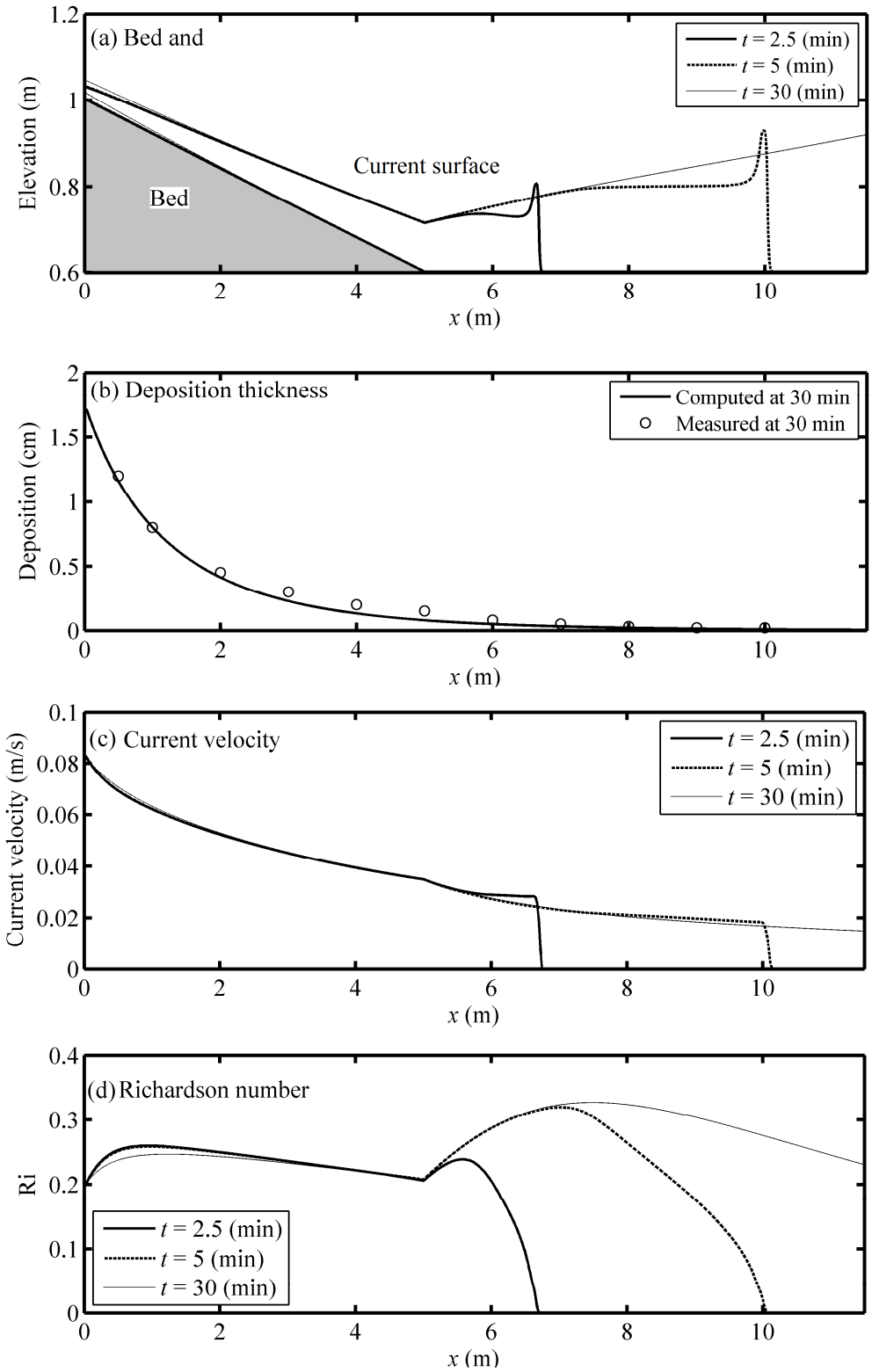

Figure 3. 5 Numerical solutions and measured data for GLASSA2 (a) bed and current surface, (b) deposition thickness, (c) current velocity, (d) Richardson number.

3.3 Experimental 2D Axisymmetric Turbidity Currents

The 2D experimental axisymmetric lock-release turbidity currents by Bonnecaze *et al.* (1995) are simulated numerically. Figure 3.6 shows a plan view of the sketch of the flume. The flume consists of a rectangular part (0.038 m wide and 0.306 m long) and a radial part (the width expands from 0.038 m to 0.294 m within 1.83 m). A lock gate is placed at the centre of the rectangular part, which separates the flume filled with water-sediment mixture on the left side and ambient clear water on the right side. Turbidity currents are initiated by instantaneous vertical withdrawal of the lock gate. The initial thickness is 0.14 m. Sediments with d = 37 μm, p = 0.5 and ρ_s = 3217 kg/m^3 are used. Three runs are conducted with different initial sediment concentrations for the turbidity volume in the LHS of the flume: 0.019, 0.01 and 0.0051, labelled as C1, C2 and C3 respectively. Based on grid-convergence tests, $\Delta x = \Delta y$ = 0.0047 m, and Cr = 0.95 are applied. C3 is used to calibrate the model parameters, which gives: r_b = 1.0 and c_D = 0.01.

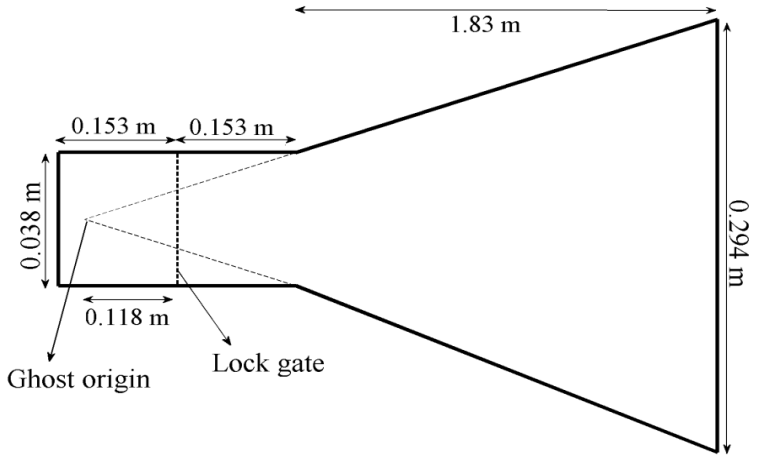

Figure 3. 6 A sketch for plan view of the 2D lock-release turbidity current.

Figs. 3.7-3.10 present the numerical solutions of C1 including distributions of current thickness (Figure 3.7), current velocity (Figure 3.8), sediment concentration (Figure 3.9) and deposition thickness (Figure 3.10), respectively. Figs. 3.7-3.10 essentially exemplify the propagation and spreading of the axisymmetric turbidity currents. In Figure 3.8, the arrows represent the velocity direction, and the contours of the current velocity are also

included. The values of the contours are indicated in the bottom-left of each graph, corresponding to the contours from the external contour to the internal contour. The maximum current velocity u in the x-direction is also stated.

Initially the water-sediment mixture stands still on the left side of the lock gate when the lock gate is closed. Once the lock gate is withdrawn, the turbidity volume slumps and plunges into the standing clear water due to the horizontal pressure difference, driving the turbidity current (Figure 3.7a, b). The current velocity attains a maximum value within this short period (0.065 m/s at t = 0.01 s, Figure 3.8a; and 0.22 m/s at t = 0.5 s, Figure 3.8b). In this stage, sediment deposition and the variation of the sediment concentration are negligible (Figure 3.10a, b; Figure 3.9a, b). Afterwards, as the currents propagate and spread, the current thickness (Figure 3.7), sediment concentration (Figure 3.9) and current velocity (Figure 3.8) decreases, due to sediment deposition (Figure 3.10) and thus the driving force reduces.

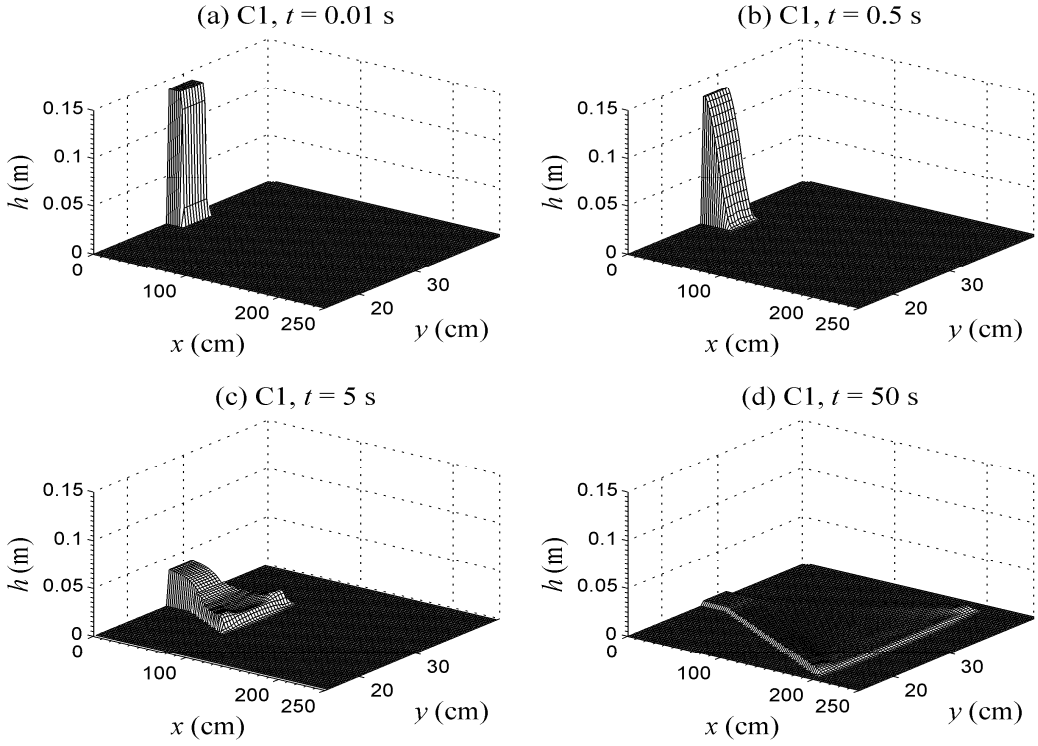

Figure 3. 7 Distributions of the computed current thickness at four times for C1.

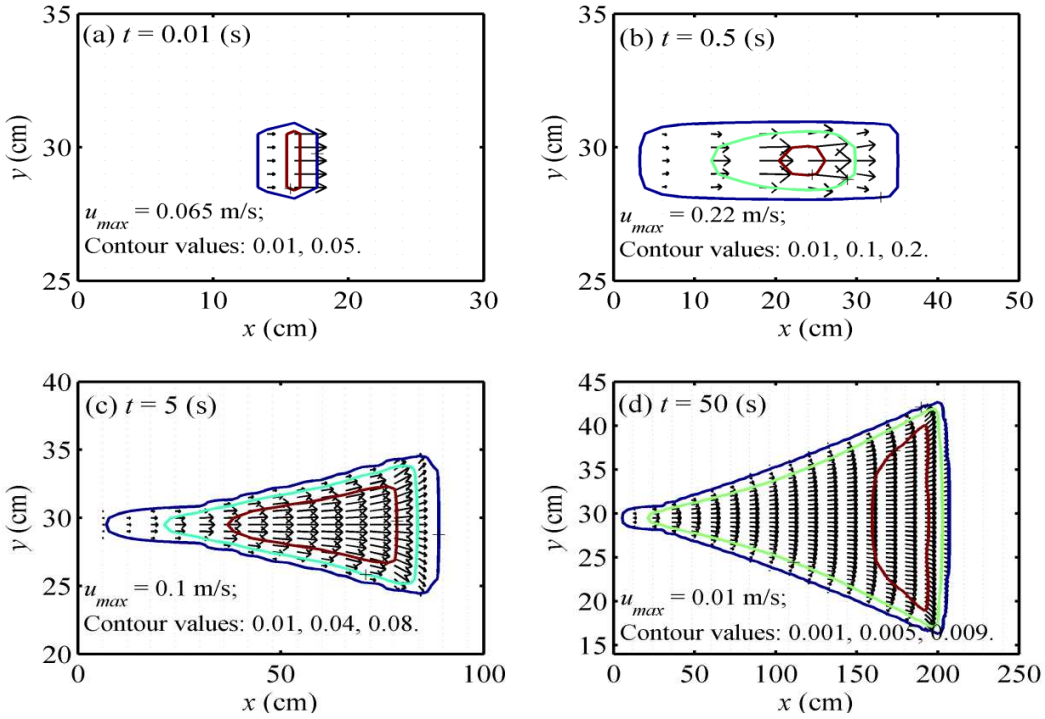

Figure 3. 8 Distributions of the computed current velocity at four times for Test C1.

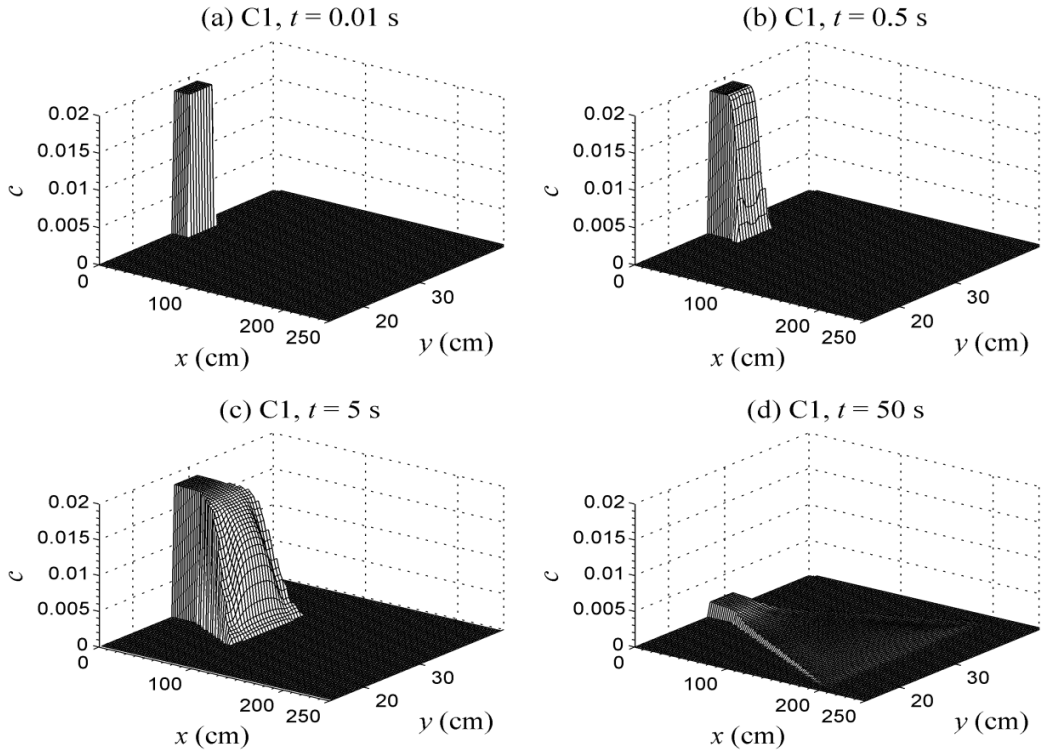

Figure 3. 9 Distributions of the computed sediment concentration at four times for C1.

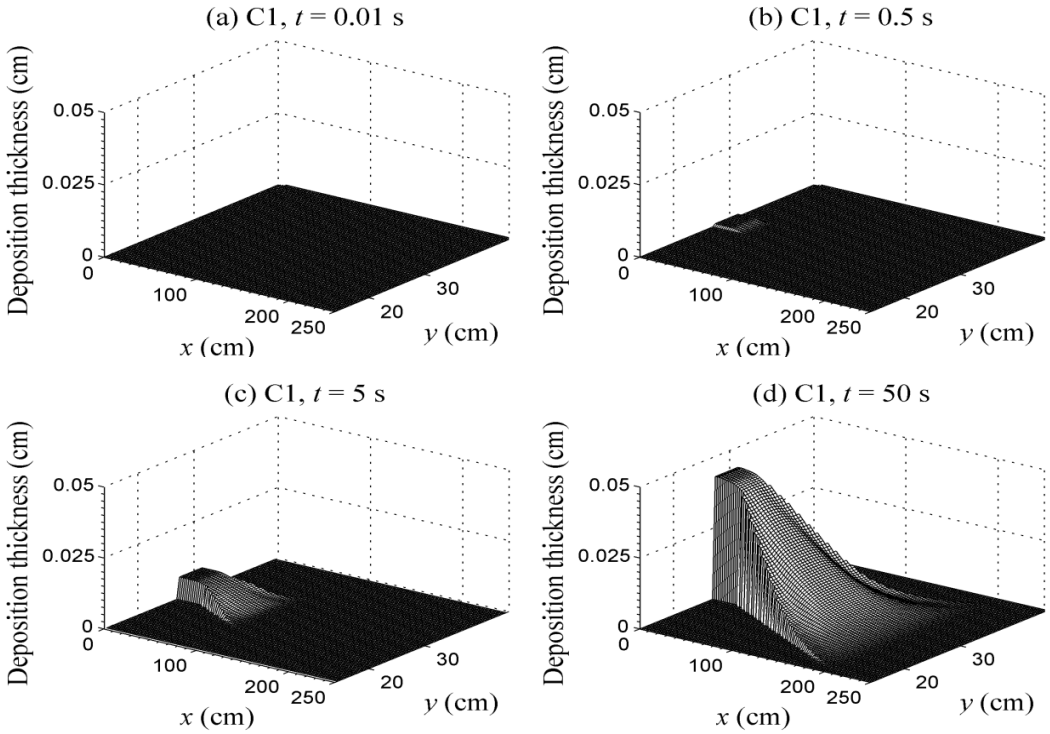

Figure 3. 10 Computed bed elevation distributions at four times for C1.

Figure 3.11 shows (a) the final deposit density versus the radial distance and (b) the current front location against time. The radial distance is measured from the ghost origin as indicated in Figure 3.6(a), which is set to be the intersection of the extended walls of the radial flume part. It is seen from Figure 3.11(b) that the turbidity currents propagate fastest at the beginning and then slow down gradually with time, consistent with that noted in Figure 3.8. The higher the initial sediment concentration (corresponding to a higher driving force), the faster the currents advance and thus the further the currents travel (Figure 3.11b). Finally the location of the current front becomes approximately stable without further propagation (Figure 3.11b). This is because the driving force is reduced gradually by sediment deposition with time, as indicated in Figure 3.11(a). Turbidity currents with a higher initial concentration deposit more sediment per area (Figure 3.11a).

Moreover, from Figure 3.11(a, b), the computed deposition density and the advance of the current front agree with the measured values rather well, though quantitative differences are observed. The 2D coupled model appears to underestimate the deposition density in the

vicinity of the left wall of the flume for turbidity currents with low sediment concentrations (C2 and C3, see Figure 3.11a). This is due to sediment depositions in the wall corners during the experiments, of which the effects can be minimized if the overall deposition becomes more pronounced as in C1 (Figure 3.11a).

The above observations suggest that the axisymmetric turbidity currents are satisfactorily resolved by the present 2D coupled model, indicating the good credibility of the 2D fully coupled model.

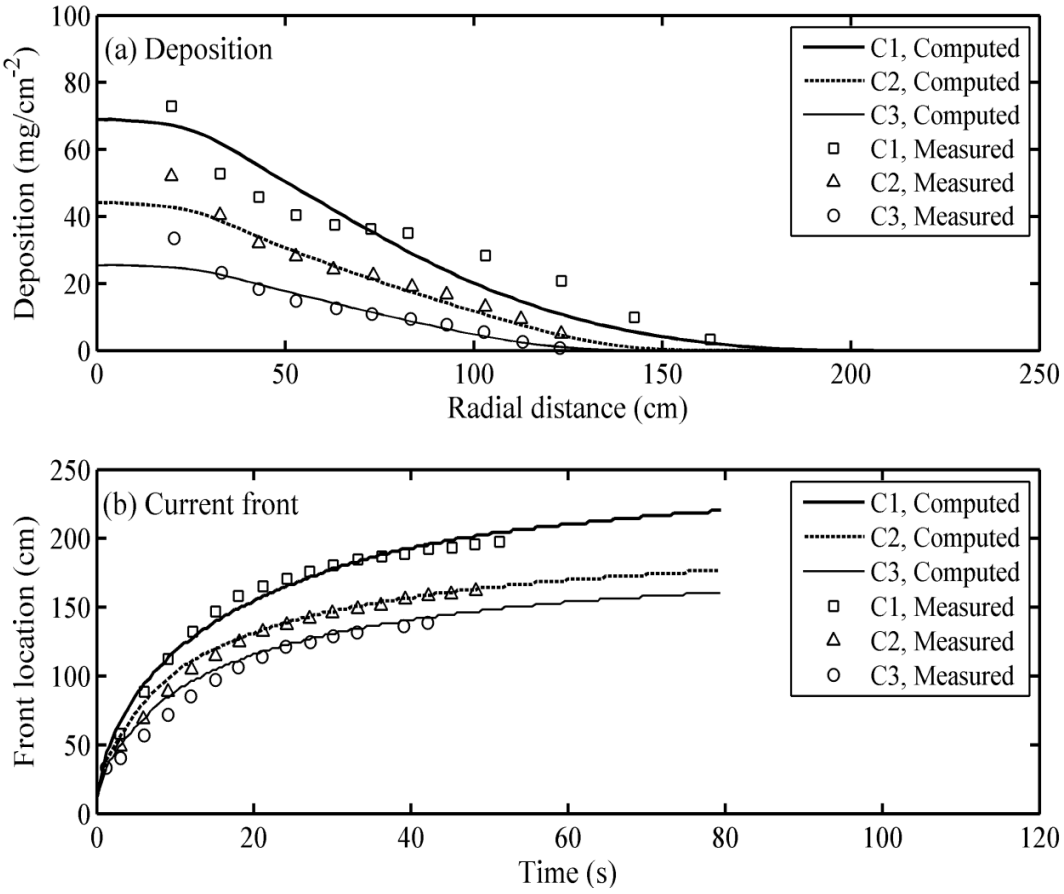

Figure 3. 11 Numerical solutions and experimental data for axisymmetric turbidity currents: (a) deposition density, (b) current front location.

3.4 Experimental Hyperconcentrated Turbidity Currents

Turbidity currents may be of very high sediment concentration in natural settings (e.g., Lowe 1982; McCave and Jones 1988; Hallworth and Huppert 1998). Due to the potential of particle-particle interactions at high concentrations, hyperconcentrated turbidity currents may behave qualitatively differently from turbidity currents with low sediment concentrations. Using experimental sediment-laden lock-release density currents with different initial sediment concentrations (Hallworth and Huppert 1998), different behaviour of hyperconcentrated turbidity currents has been observed in terms of the current front location and the deposition thickness, as compared to low concentration turbidity currents. A side view of the flume can be seen in Figure 3.12. The flume is 2 m long, 0.2 m wide and 0.25 m deep. The lock gate is placed at 3 cm from the left side of the flume. The initial water-sediment mixture and ambient water depth is 0.10 m. The initial concentration ranges from 0.025 to 0.40, sediment diameter d = 0.009 mm, sediment density ρ_s = 3217 kg/m^3.

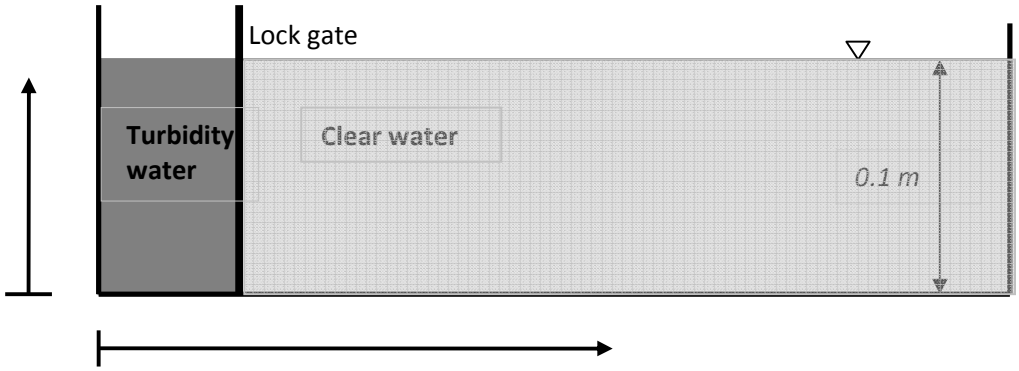

Figure 3. 12 A side view of the rectangular flume by Hallworth and Huppert (1998).

Figure 3.13 shows the experimental data (a) the position of the current front versus t; and (b) the deposit density versus x. The deposit density is the local deposition mass normalized by the total deposition mass D/M_0. From Figure 3.13, hyperconcentrated turbidity currents propagate rapidly the same as dilute turbidity currents during the slump stage in the vicinity of release, however, beyond a threshold concentration (0.275, Figure 3.13), the former experienced a pronounced and sudden arrest, depositing their sediment close to the release point, featuring step geometries (Figure 3.13b). The arrest point

approaches progressively closer to the release point and the deposition becomes steeper as the initial sediment concentration increases. This phenomenon is termed an abrupt transition of a hyperconcentrated turbidity current.

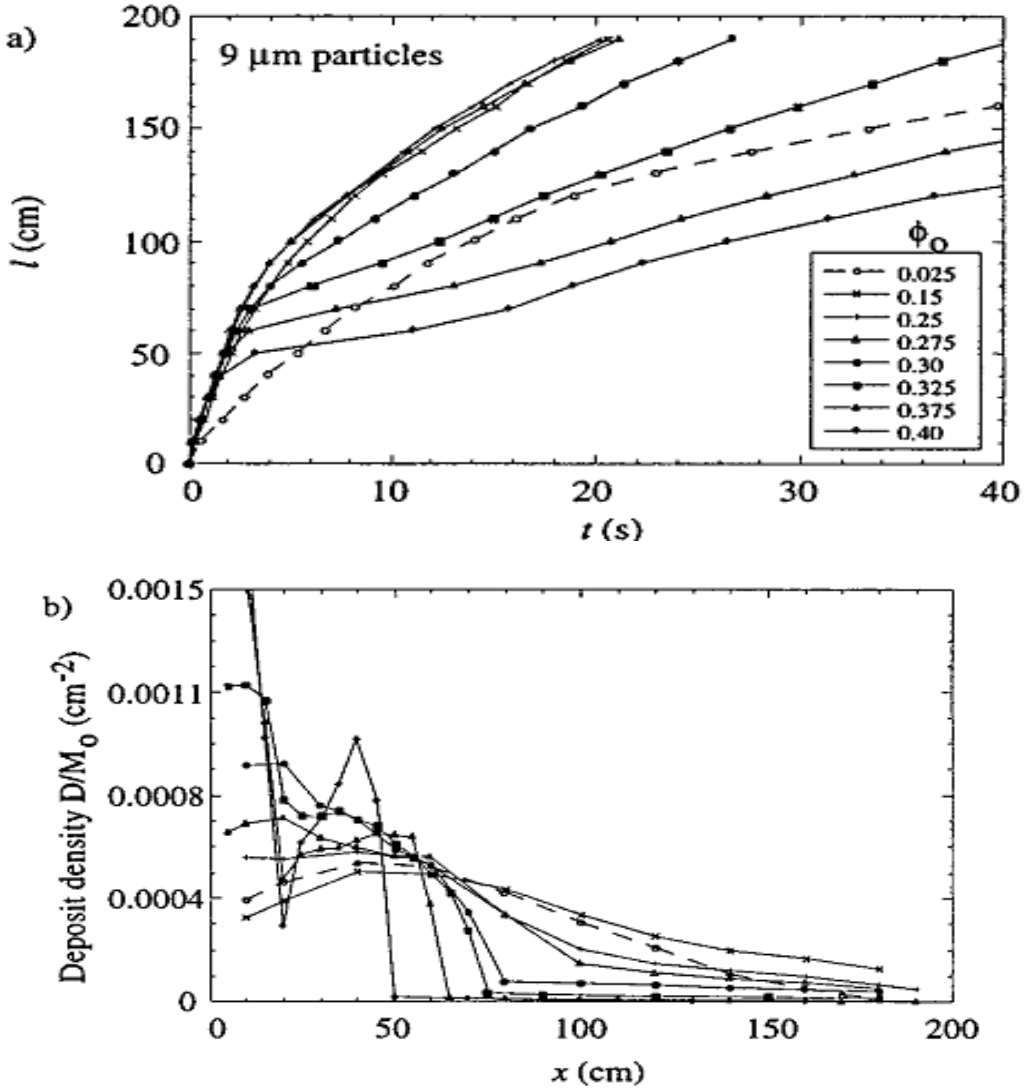

Figure 3. 13 Experimental results by Hallworth and Huppert (1998), with permission of AIP. (a) position of the current front versus t; and (b) deposit density versus x, using various initial concentrations as indicated in the legend.

Based on experimental saline density currents, Amy *et al*. (2005a) attributed this different behaviour to the difference in the magnitude of the Reynolds number. By depth-resolving

3D simulation, Cantero *et al*. (2007) suggested that the physical basis for this reason remains an open question. There has been a proposition that the abrupt transition might be due to the non-Newtonian property at high concentrations (Huppert 2006). This proposition echoes with the observed abrupt halt of the hyperconcentrated flood in the Yellow River, of which the non-Newtonian property is well known (Qian and Wan 1993). Hyperconcentrated floods in the Yellow River may come to stop suddenly and block the river accompanied by severe sedimentation, due to the non-Newtonian property at high concentrations (Cao *et al.* 2006; YRCC 2007). Yet a physically-based explanation for the abrupt transition of hyperconcentrated turbidity current remains an unresolved question.

In this section, the non-Newtonian property at high concentrations is tentatively incorporated in the fully coupled model, and the experimental lock-release turbidity currents by Hallworth and Huppert (1998) are investigated numerically. By incorporating a Bingham yield stress, the relationship for bed shear stress Eq. (2.12) is revised as

$$\tau_{bx} = \rho u_*^2 + \tau_B \tag{3.1}$$

where τ_B = Bingham yield stress, estimated simply as (Qian and Wan, 1983)

$$\tau_B = k_1 c^{k_2} \tag{3.2}$$

where k_1, k_2 are empirical coefficients, usually greater than unity.

When the sediment concentration is not sufficiently large, the Bingham yield stress would be negligible, thus turbidity currents would behave as a Newtonian fluid; on the contrary, at high concentrations, the non-Newtonian properties have a noticeable influence on the current evolution. Two cases are considered here with ($k_1 = 100.0$ and $k_2 = 8.0$) and without ($k_1 = 0.0$ and $k_2 = 0.0$) incorporating the potential non-Newtonian property. Other parameters are: $p = 0.4$ and $c_D = 0.02$. Based on grid convergence tests, the spatial step Δx = 0.002 m and Cr = 0.9. The upstream boundary conditions are specified by mass conservations of the water-sediment mixture and sediment. Six different initial sediment concentrations are considered for both cases.

The slumping and propagation processes of these turbidity currents are qualitatively similar to these of the 2D axisymmetric turbidity currents considered in **Section 3.3**. Thus they are not discussed further here. Figure 3.14 presents the numerical solutions for which the potential for non-Newtonian property is not accounted for (a) the position of the current front versus *t* and (b) the final deposition density versus distance. Figure 3.15 presents those when the Bingham yield stress is considered.

When turbidity currents are treated as Newtonian fluid, turbidity currents with large initial sediment concentrations propagate faster than those with relatively low concentrations (Figure 3.14a). This can be explained from the perspective of the driving force of turbidity currents. The higher the sediment concentration, the greater the driving force, thus the faster and farther the turbidity current propagates. Accordingly, the deposition by turbidity currents with higher concentration extends further downstream (Figure 3.14b). These observations are in accordance with the existing understanding of low concentration turbidity currents (e.g., Huppert and Simpson 1980; Bonnecaze *et al*. 1993, 1995; Dade and Huppert 1995), however are in contradiction with the understanding of hyperconcentrated turbidity currents (Hallworth and Huppert 1998).

When the potential of the non-Newtonian property is considered, the propagation of turbidity current is subdued to a certain extent (Figure 15a). This is because turbidity currents have to overcome the Bingham yield stress. When the initial concentration is not sufficiently large (say, lower than 0.25), the Bingham yield stress is relatively small and the effects of non-Newtonian behaviour are negligible. However, as the initial concentration increases and exceeds a threshold value, the Bingham yield stress becomes increasingly dominant and the influence of non-Newtonian property of the turbidity current becomes significant, thereby the relationship between the initial concentration and the advance of current front exhibits a reversed tendency in comparison to those of lower density, which is similar to the observed abrupt transition for hyperconcentrated turbidity currents by Hallworth and Huppert (1998).

These can also be clearly seen from the geometric from of the final deposit densities as shown in Figure 3.15(b). For dilute turbidity currents, the deposition density has a

maximum value near the release point and decreases to zero along the channel. On the contrary, a step geometry of the deposition density is predicted for hyperconcentrated turbidity currents and the maximum deposition density appears at the downstream of the channel. The step geometric form becomes steeper as the initial concentration increases. These observations are similar to the observed difference between the turbidites (due to turbidity currents with low concentrations) and debrites (due to turbidity currents with high concentrations) in the Marnoso-arenacea Formation, Italy (Amy *et al*. 2005b; Amy and Talling 2006). Turbidites created by low density turbidity currents tend to thin gradually downstream, whereas those by high density turbidity currents feature abrupt terminations.

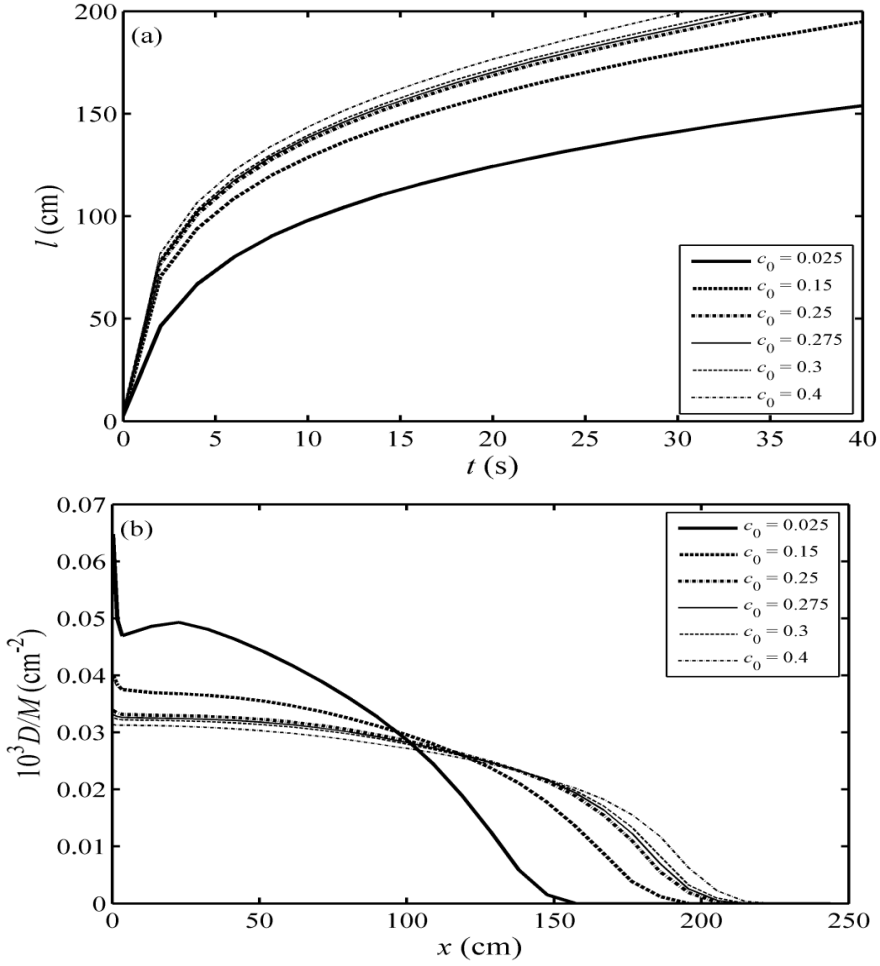

Figure 3. 14 (a) Position of the current front versus t and (b) deposition density $10^3 D / M_0$ versus x for those when the potential of non-Newtonian effects is not accounted for.

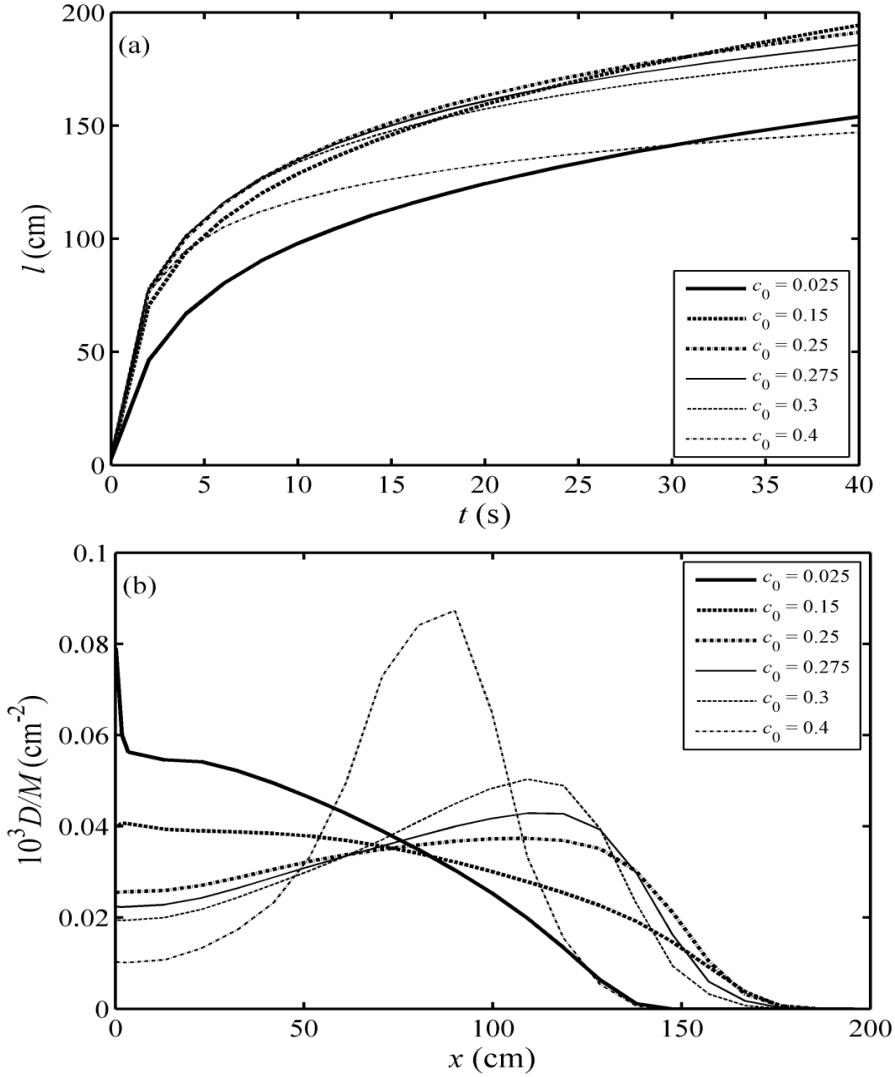

Figure 3. 15 (a) Position of the current front versus t and (b) deposition density $10^3 D / M_0$ versus x for those when the potential of non-Newtonian effects is accounted for.

Considering the non-Newtonian property at high concentrations, the fully coupled model can reproduce reasonably well the phenomenon of abrupt transition for hyperconcentrated turbidity currents. This allows us to propose that the property of non-Newtonian fluid should be responsible for abrupt transitions in hyperconcentrated turbidity currents. There are inevitable quantitative differences, yet it will have at least contributed a better understanding of the mechanism of hyperconcentrated turbidity currents. The successful reproduction of the abrupt transition indicates excellent performance of the fully coupled model.

Chapter 4. MULTIPLE TIME SCALES – SIGNIFICANCE OF COUPLED MODELLING

Summary

- Multiple time scale theory is developed to analyze theoretically the interactions between the current, sediment transport and bed topography and deformation
- Self-accelerating turbidity currents representative of those occurring in the Scripps Submarine Canyon are simulated to complement the analyses of time scales
- Fully coupled modelling is shown to be critical

The interactions between the current, sediment transport, and morphological change (bed deformation) normally assume multiple time scales, which essentially dictate whether the feedback impacts of bed deformation appreciably affect the current evolution, i.e., the conditional applicability of decoupled and partially coupled models, as compared to a fully coupled model. If the rate of bed deformation is smaller than that of the current change by an order (or orders) of magnitude, the feedback impact of bed deformation on the currents might be negligible, thus partially coupled or decoupled modelling may be applicable, and vice versa. In this chapter, the significance of fully coupled modelling for turbidity currents is demonstrated. First, the time scales of turbidity currents are defined and analyzed under static conditions. Second, self-accelerating turbidity currents representative of those occurring in the Scripps Submarine Canyon are numerically simulated and numerical comparisons are conducted with regard to different models as summarized in Table 2.1.

4.1 Time Scales of Turbidity Currents

The theory of multiple time scales was developed first for (subaerial) fluvial processes with uniform suspended sediment transport by Cao *et al.* (2007), and then extended to fluvial

processes with uniform bed load sediment transport (Cao *et al.* 2010, 2011). Efforts are being made to derive multiple-time-scale understanding of fluvial processes with graded sediment transport. Here the multiple-time-scale theory is developed for turbidity currents to understand the multiple time scales of the interactions between turbidity currents, sediment transport and morphological change. Although subaqueous turbidity currents differ from sediment-laden open channel flow in many aspects (Qian and Wan 1983; Simpson 1997), this extension is theoretically justified as the governing equations of turbidity currents are of a hyperbolic nature (Bradford *et al.* 1997; as also suggested below by the existence of the four real eigenvalues for the matrix **A**).

By time scale, it means the time that governs the rate of the change of a specific quantity describing the current, for example, current thickness and sediment transport rate or bed deformation. Physically, it measures how fast a physical quantity of the turbidity currents changes with time. The greater the time scale, the slower the physical quantity varies in time, and vice versa. Consider a general ordinary differential equation for a physical quantity σ

$$d\sigma / dt = \Theta \tag{4.1a}$$

or simply an order-of-magnitude estimation

$$d\sigma / dt \sim \Theta \tag{4.1b}$$

The time scale of the physical quantity σ is defined as $T_\sigma = abs(\sigma / \Theta)$, which is dictated by the variation rate of σ with time.

4.1.1 Definitions

Since the layer-averaged governing equations for turbidity currents are of a hyperbolic nature, they can be transformed into a set of ordinary differential equations (compatibility equations) along characteristics. The analysis of the time scales is underpinned by the characteristic theory for the hyperbolic governing equations. As a characteristic cone is involved for 2D governing equations, which is mathematically complicated, the multi-scale

theory is presented with regard to a 1D turbidity current for qualitative understanding. The 1D governing equations are first rewritten in primitive form as follows,

$$\frac{\partial \mathbf{W}}{\partial t} + \mathbf{A}\frac{\partial \mathbf{W}}{\partial x} = \mathbf{R} \tag{4.2}$$

with

$$\mathbf{W} = \begin{bmatrix} h \\ u \\ c \\ z \end{bmatrix}, \qquad \mathbf{A} = \begin{bmatrix} u & h & 0 & 0 \\ Rgc & u & \frac{Rgh}{2} & Rgc \\ 0 & 0 & u & 0 \\ 0 & 0 & 0 & 0 \end{bmatrix}$$

$$\mathbf{R} = \begin{bmatrix} R_1 \\ R_2 \\ R_3 \\ R_4 \end{bmatrix} = \begin{bmatrix} E_w + (E-D)/(1-p) \\ -[\frac{\rho_w}{\rho} E_w u + \frac{u(E-D)\rho_0}{(1-p)\rho} + u_*^2(1+r_w)]/h \\ [(E-D)(1-p-c)/(1-p) - cE_w]/h \\ -(E-D)/(1-p) \end{bmatrix}$$

where $\mathbf{W}$ = vector of primitive variables, $\mathbf{A}$ = matrix, $\mathbf{R}$ = vector of source terms. The characteristics and the corresponding characteristic compatibility equations for Eq. (4.2) read

$$\begin{cases} dx/dt = \lambda_k \\ \mathbf{L}^k \left(\frac{d\mathbf{W}}{dt}\right)\Big|_{\lambda_k} = \mathbf{L}^k \left(\frac{\partial \mathbf{W}}{\partial t} + \lambda_k \frac{\partial \mathbf{W}}{\partial x}\right) = \mathbf{L}^k \mathbf{R} \end{cases} \qquad k = 1,2,3,4 \tag{4.3a, b}$$

where λ_1, λ_1, λ_3 and λ_4 = celerities that are the eigenvalues of $\mathbf{A}$ and can be computed from $|\mathbf{A} - \lambda \mathbf{I}| = 0$ (where $\mathbf{I}$ is the unit matrix), $\mathbf{L}^k$ = left eigenvector corresponding to the eigenvalue λ_k. The analytical expressions for the left eigenvector $\mathbf{L}^k$ and λ_k are as follows

$$\begin{cases} dx/dt = \lambda_{1,2} = u \pm \sqrt{g'h} = u \pm \sqrt{Rgch} \\ \dfrac{du}{dt} \pm \sqrt{\dfrac{Rgc}{h}} \dfrac{dh}{dt} \pm \dfrac{Rgh}{2\sqrt{Rgch}} \dfrac{dc}{dt} + \dfrac{Rgc}{u \pm \sqrt{Rgch}} \dfrac{dz}{dt} \\ \qquad = R_2 \pm \sqrt{\dfrac{Rgc}{h}} R_1 \pm \dfrac{Rgh}{2\sqrt{Rgch}} R_3 + \dfrac{Rgc}{u \pm \sqrt{Rgch}} R_4 \end{cases} \tag{4.4a, b}$$

$$\begin{cases} dx/dt = \lambda_3 = u \\ \dfrac{dc}{dt} = R_3 = \dfrac{\partial c}{\partial t} + \lambda_3 \dfrac{\partial c}{\partial x} \end{cases} \tag{4.5a, b}$$

$$\begin{cases} dx/dt = \lambda_4 = 0 \\ \dfrac{dz}{dt} = R_4 = \dfrac{\partial z}{\partial t} \end{cases} \tag{4.6a, b}$$

For congruence of evaluation, time scales are all defined along the $\lambda_{1,2}$-characteristics. For sediment concentration and bed elevation, the following can be derived

$$\left.\frac{dc}{dt}\right|_{\lambda_{1,2}} = \frac{\partial c}{\partial t} + \lambda_{1,2} \frac{\partial c}{\partial x}, \qquad \left.\frac{dz}{dt}\right|_{\lambda_{1,2}} = \frac{\partial z}{\partial t} + \lambda_{1,2} \frac{\partial z}{\partial x} \tag{4.7a, b}$$

From Eq. (4.5b) and Eq. (4.6b)

$$\frac{\partial c}{\partial t} = R_3 - \lambda_3 \frac{\partial c}{\partial x}, \qquad \frac{\partial z}{\partial t} = R_4 \tag{4.8a, b}$$

Substituting Eq. (4.8a, b) into Eq. (4.7a, b), one has

$$\left.\frac{dc}{dt}\right|_{\lambda_{1,2}} = R_3 + (\lambda_{1,2} - \lambda_3)\frac{\partial c}{\partial x} = R_3 \pm \sqrt{gh}\frac{\partial c}{\partial x} \tag{4.9a}$$

$$\left.\frac{dz}{dt}\right|_{\lambda_{1,2}} = R_4 - \lambda_{1,2} S_{bx} \tag{4.9b}$$

Substituting Eq. (4.9a, b) into Eq. (4.4a, b), one gets

$$\frac{du}{dt} \pm \sqrt{\frac{Rgc}{h}} \frac{dh}{dt} = RgcS_{bx} + R_2 \pm \sqrt{\frac{Rgc}{h}} R_1 - \frac{Rg}{2} h \frac{\partial c}{\partial x} = R_{hu} \tag{4.10}$$

In general, the two terms in the LHS of Eq. (4.10) are of the same order of magnitude as R_{hu}. Otherwise, say, dh/dt (or du/dt) was of a lower order-of-magnitude and thus neglected, one would yield two usually distinct values of velocity (or current thickness) from the two compatibility equations along the $\lambda_{1,2}$ - characteristics. Therefore, the following order-of-magnitude estimations can be obtained along the $\lambda_{1,2}$ - characteristics

$$\frac{du}{dt} \sim R_{hu} \ , \ \frac{dh}{dt} \sim R_{hu} \sqrt{\frac{h}{Rgc}} \tag{4.11a, b}$$

According to Eq. (4.11), the time scales of the currents can be defined as

$$T_u = \left| \frac{u}{R_{hu}} \right| \qquad \text{time scale } T_u \text{ of the current velocity} \tag{4.12}$$

$$T_h = \frac{h}{\left| R_{hu} \sqrt{h/Rgc} \right|} = \frac{T_u}{Fr} \qquad \text{time scale } T_h \text{ of the current thickness} \tag{4.13}$$

Of particular interest is the rate of bed deformation due to non-equilibrium sediment transport as represented by $\partial z/dt = R_4$, which is valid along any characteristics, including the $\lambda_{1,2}$-characteristics. In analogy to the definitions of the time scales T_u and T_h, it is straightforward to define the time scale of bed deformation as $z/|R_4|$. However, the magnitude of the bed elevation z depends on the defined datum level. Thus the expression $z/|R_4|$ would incur an issue of nonuniqueness for the time scale due to the arbitrary definition of the datum. The most viable length scale, the current thickness, is used as a compromise for the definition of the time scale of bed deformation

$$T_b = \frac{h}{|R_4|} \qquad \text{time scale } T_b \text{ of bed deformation} \tag{4.14}$$

Moreover, it is the rate of bed deformation relative to that of the change of the flow depth that is directly critical in quantifying the effects of bed deformation on the current evolution. Thus the time scale of bed deformation relative to that of the flow depth can be defined as the ratio of the change rates of the two variables

$$T_{b/h} = \frac{\left| R_{hu} \sqrt{h / Rgc} \right|}{R_4} \tag{4.15}$$

From Eqs. (4.13), (4.14) and (4.15), it is easy to get that $T_b / T_h = T_{b/h}$, indicating the compromise made in defining the time scale T_b in Eq. (4.14) has no effect on the assessment of the feedback impacts of bed deformation.

4.1.2 Static Time Scales and Implications

The time scales defined above are evaluated under static conditions here in relation to self-accelerating turbidity currents representative of the Submarine Scripps Canyon (Fukushima *et al*. 1985; Parker *et al*. 1986), with the following relevant parameters: d = 0.15 mm, ω = 0.0165 m/s, ρ_s = 2650 kg/m3, p = 0.4, c_D = 0.004, ψ_p = 1, υ = 1E-6 m/s^2, h = 3 m, S_{bx} = 0.08, $\partial c / \partial x$ = 0.0003. The bed shear velocity and sediment concentration are varied over a wide spectrum. With these parameters, the time scales T_u, T_h and T_b / T_h can be computed according to Eqs. (4.12 to 4.15) along with the empirical formulae presented in Chapter 2.

Figure 4.1 shows the contours of the time scale T_u of the current velocity in the $u_* - c$ plane along (a) the λ_1-characteristics and (b) the λ_2 -characteristics. The existence of double values of T_u is evident, respectively along λ_1- and λ_2 -characteristics (comparing Figs. 4.1a and 4.1b). This is due to the third term $\pm \sqrt{Rgc / h} R_1$ in the middle of Eq. (4.10). The contours of T_u along the two characteristics are qualitatively similar and only exhibit slight quantitative differences. Thus the analyses below pertain to the time scale T_u along the λ_1-characteristics, which are essentially applicable to both characteristics.

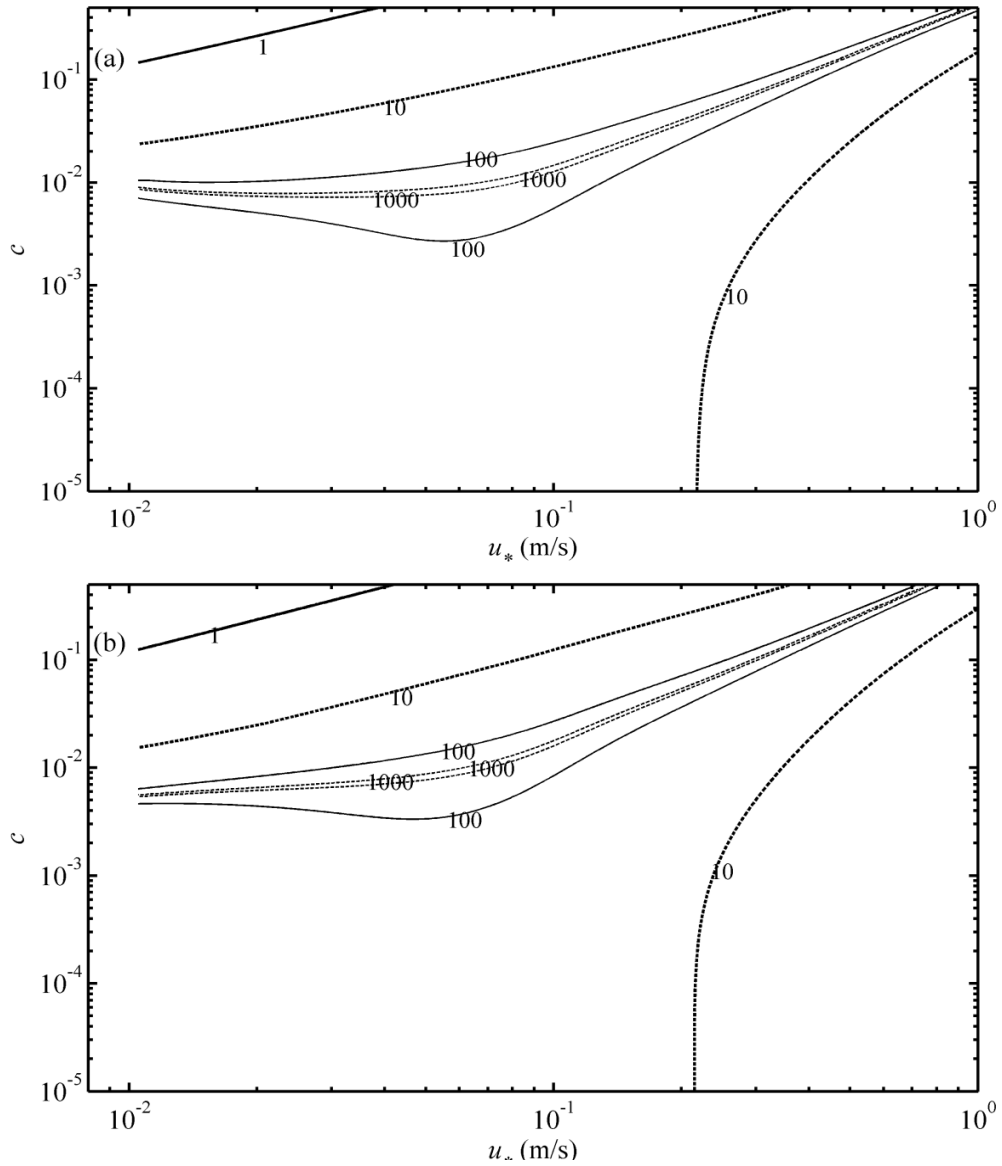

Figure 4. 1 Contour of the time scale T_u of the current velocity in the $u_* - c$ phase along (a) λ_1- characteristics and (b) λ_2- characteristics.

The time scale T_u essentially characterizes the change rate of current velocity along the characteristics. The larger the time scale T_u, the slower it varies; and vice versa. Notably, there exists a long and narrow region where the maximum value of T_u appears, i.e., T_u> 1000, indicating negligible variation rate of the current velocity. This in essence should correspond to an approximately steady and uniform regime. In other regions, the further the

distance that it is away from the region of T_u > 1000, the smaller T_u is. This suggests that turbidity current has a trend to adjust to a steady and uniform state. The further the currents are away from the steady and uniform regime, the faster the adaptation is; and vice versa.

As shown in Figure 4.2 are the contours of the time scale T_h of the current thickness along (a) the λ_1-characteristics and (b) the λ_2 -characteristics. Considerable differences can be seen between T_u and T_h, as the latter is differentiated by the densimetric Froude number (see Eq. 4.13). Under given current conditions (bed shear velocity and current thickness), the values of the time scale T_h tend to be generally greater than that of the time scale T_u for higher sediment concentrations, whereas for lower sediment concentrations $T_h < T_u$. This is because the magnitude of the densimetric Froude number depends on sediment concentration. Nevertheless the locations of the regions with $T_h > 1000$ and $T_u > 1000$ resemble each other well, suggesting a steady and uniform regime.

To maintain a steady, uniform turbidity current, it is equally important to have a state of equilibrium sediment transport, i.e., there is a vanishing sediment exchange between the current and the loose bottom boundary and negligible bed deformation, which is not typical of turbidity currents. An examination of the time scale T_b of bed deformation would shed insight on this issue. Figure 4.3 illustrates the contours of the time scale T_b of bed deformation, of which the value is independent of the λ_1- and λ_2 -characteristics. The greater the time scale T_b, the slower the bed deformation. In Figure 4.3, a region where the maximum value of T_b appears (say, T_b> 100000) is evident, implying that bed deformation is negligible and sediment transport is in a quasi-equilibrium state. Actually, this region is in essence immediately around the curve of sediment transport capacity as estimated by Eq. (2.19a). Comparing the time scale T_b for bed deformation (Figure 4.3) and the time scales T_u or T_h (Figure 4.1 or Figure 4.2), the regions with maximum T_b and T_h (or T_u) hardly collapse onto each other in the $u_* - c$ plane. Probably there would be only two intersections due to the convex and concave characteristics of the two regions with T_h> 1000 and T_b> 100000 respectively.

These has interesting implications. When the current tends to attain a steady and uniform regime, sediment transport is likely to be non-equilibrium, which would change the driving force and make the current deviate from the steady and uniform state. In contrast, even if the sediment transport is in equilibrium, the current may be unsteady or nonuniform, which would induce a variation in sediment exchange. These suggest that steady and uniform turbidity current under equilibrium sediment transport may not exist simultaneously.

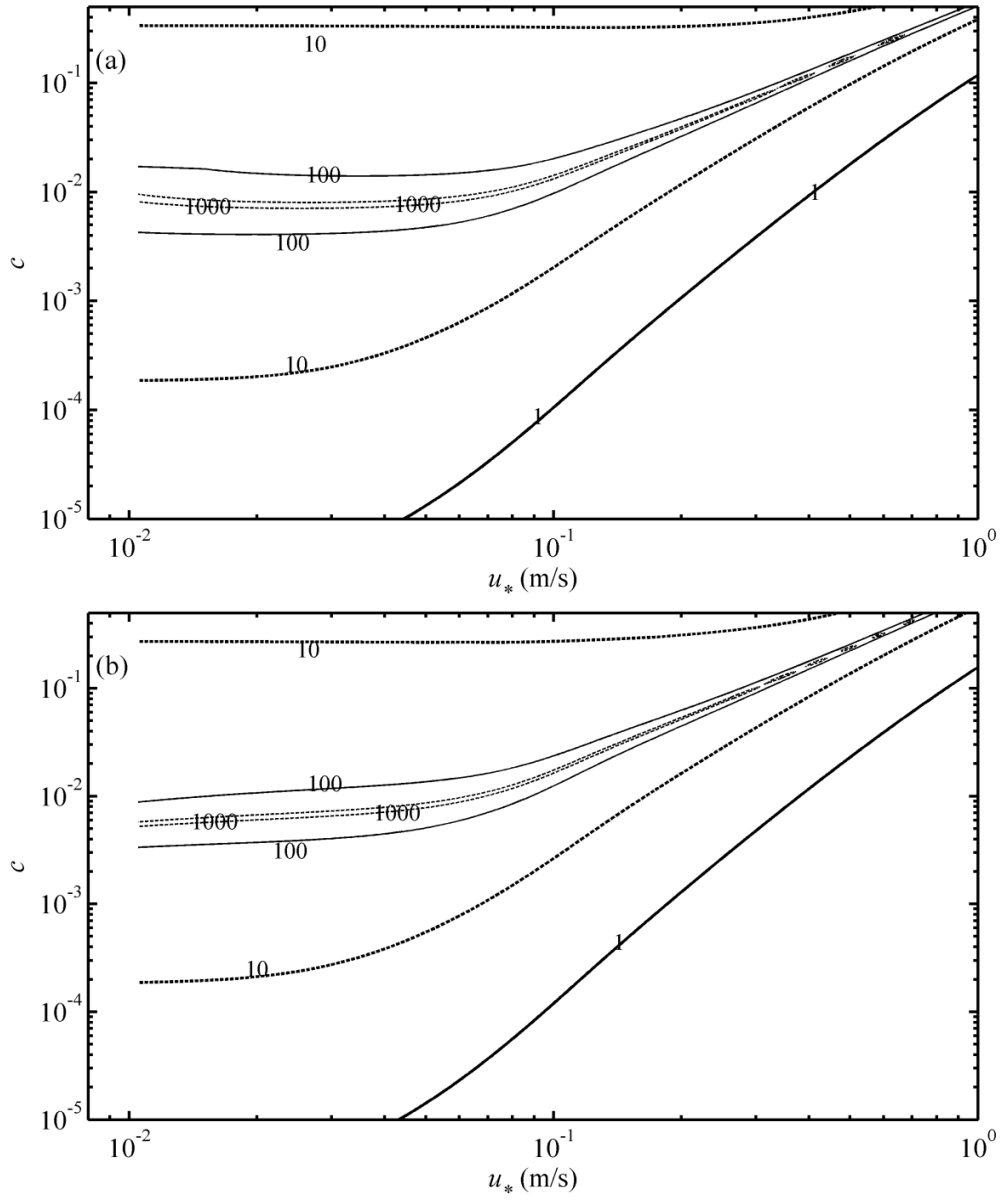

Figure 4. 2 Contours of the time scale T_h of the current thickness along (a) λ_1 - characteristics and (b) λ_2 - characteristics.

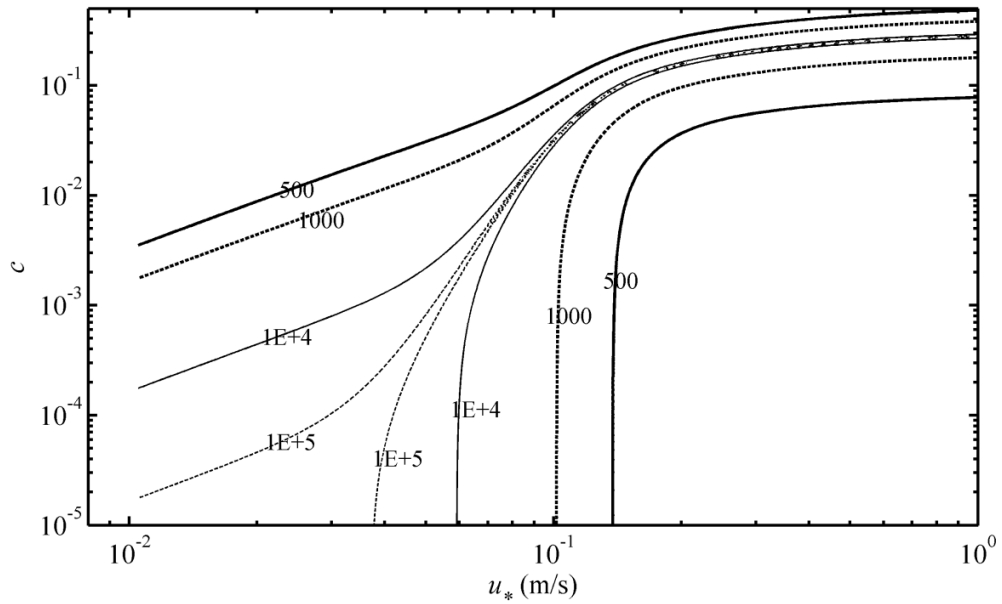

Figure 4. 3 Contour of the time scale T_b of the current velocity.

Of particular interest is the relative rate of bed deformation against the change of current thickness, which can be measured by T_b/T_h. Figure 4.4 illustrates the contour of T_b/T_h in the u_*-c plane along (a) the λ_1-characteristics and (b) the λ_2-characteristics. T_b/T_h along the two characteristics are quantitatively only slightly different. In addition to a region with a very large value of the relative time scale T_b/T_h> 1000, there also exists a region with a very small value of the relative time scale T_b/T_h< 1. It is not surprising to see that the region with T_b/T_h> 1000 essentially corresponds to the region with T_b> 100000 in Figure 4.3, and the region with T_b/T_h< 1 corresponds to the region with T_h > 1000 in Figure 4.2. It is consistent with the prior speculation that there are only two intersections in the u_*-c plane between the regions with T_h > 1000 or T_b/T_h< 1 and the region with T_b> 100000 or T_b/T_h> 1000, suggesting steady and uniform turbidity current with equilibrium sediment transport hardly exist.

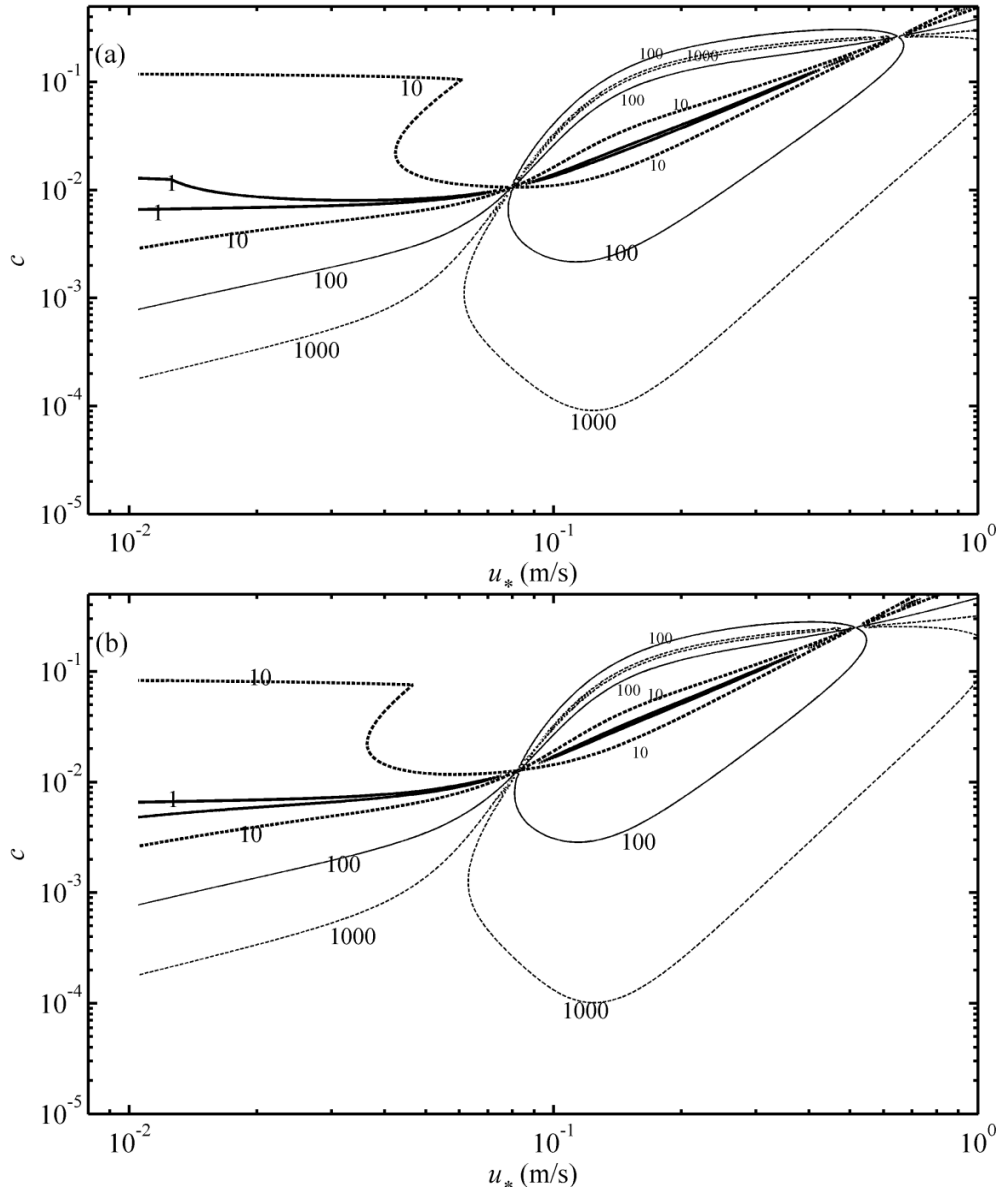

Figure 4. 4 Contour of the relative time scale T_b/T_h along (a) λ_1- characteristics and (b) λ_2- characteristics.

Figure 4.4 actually shows the rate at which the bed deforms, relative to the change of the turbidity current thickness. Physically the greater the value of T_b/T_h, the slower the bed deforms in relation to the current, and the less the bed deformation affects the current. Thus, existing decoupled or partially coupled models may be approximately applicable. In contrast, when T_b/T_h is not sufficiently large, the feedback impact of bed deformation

deserves full consideration, thus fully coupled models must be employed. In Figure 4.4(a) it is observed that the variation of T_b/T_h exhibits a rather sophisticated pattern against the bed shear velocity and sediment concentration. Similar to the proposition of Cao *et al.* (2007), two critical values (1000, 100) are tentatively used to distinguish the regimes with different relative time scale of bed deformation, and accordingly the applicability of mathematical models is suggested (see Table 4.1). In the region with $T_b/T_h >$ 1000, the rate of bed deformation is at least three orders slower than that of the change of current thickness. This region is termed NBD, in which a decoupled model might be justified. Furthermore, there exists a WBD regime with $100 < T_b/T_h <$ 1000 in the vicinity of NBD region, in which the rate of bed deformation is considerable, yet its feedback impacts may not be appreciable. Presumably for the WBD, a partially coupled model suffices. Thirdly, the existence of the large region with $T_b/T_h <$ 100 is evident, corresponds to the RBD regime, in which the rate of bed deformation as well as its feedback impact on the current change are considerable, and use of a fully coupled model is critical.

Table 4. 1 Regimes of bed deformation

T_b/T_h	T_b/T_h>1000	1000> T_b/T_h >100	100> T_b/T_h
Regime	Negligible bed deformation (NBD)	Weak bed deformation (WBD)	Rapid bed deformation (RBD)
Model	TEM, PCM or FCM	PCM or FCM	FCM

As shown in Figs. 4.5-4.7, a sensitivity analysis of key variables (current thickness, bed slope, the spatial gradient of sediment concentration) is conducted with regard to the relative time scale T_b/T_h. Except the changed values of these key variables as indicated in the figure titles, all other parameters are the same as those used for Figs. 4.1-4.4. From Figure 4.5-4.7, all these key variables exert a considerable quantitative effect on the relative time scale T_b/T_h, yet they are qualitatively similar. The relative time scale T_b/T_h in Figs. 4.5-4.7 further demonstrate a necessity of fully coupled modelling at most conditions.

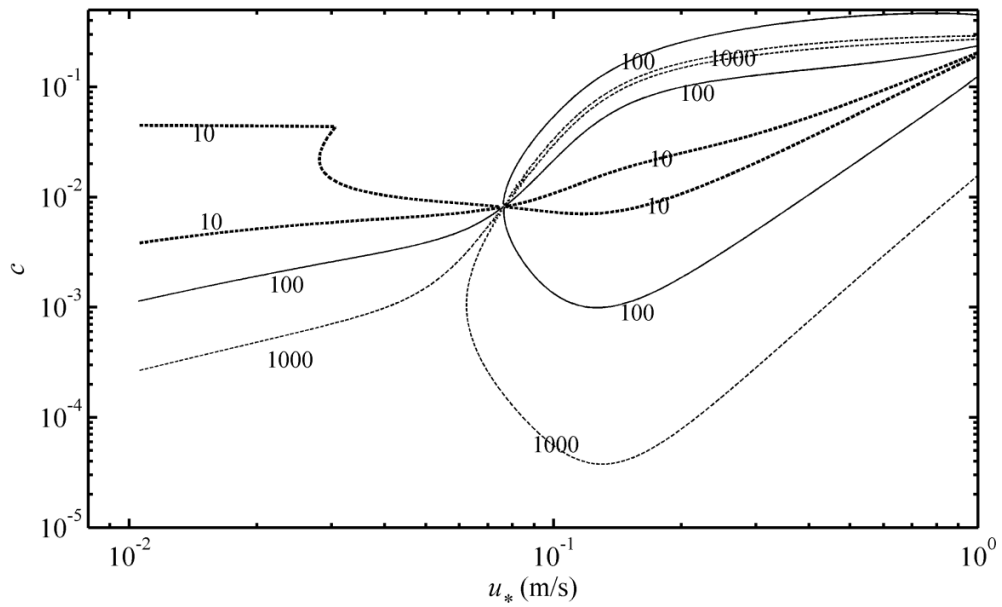

Figure 4. 5 Impact of current thickness with h = 10 m: T_b / T_h along the λ_1 -characteristic.

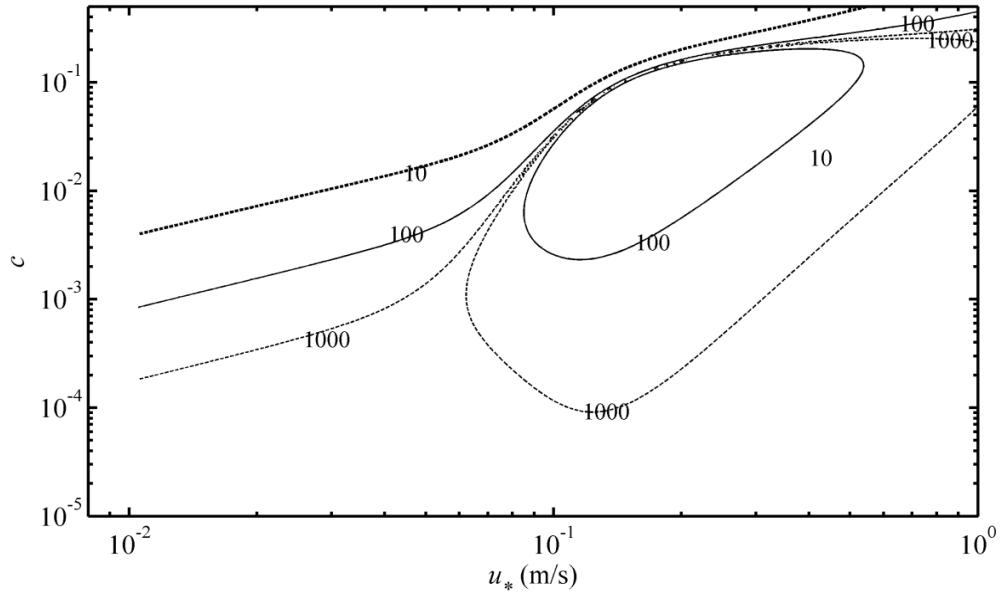

Figure 4. 6 Impact of bed slope with S_{bx} = 0.001 m: T_b / T_h along the λ_1-characteristic.

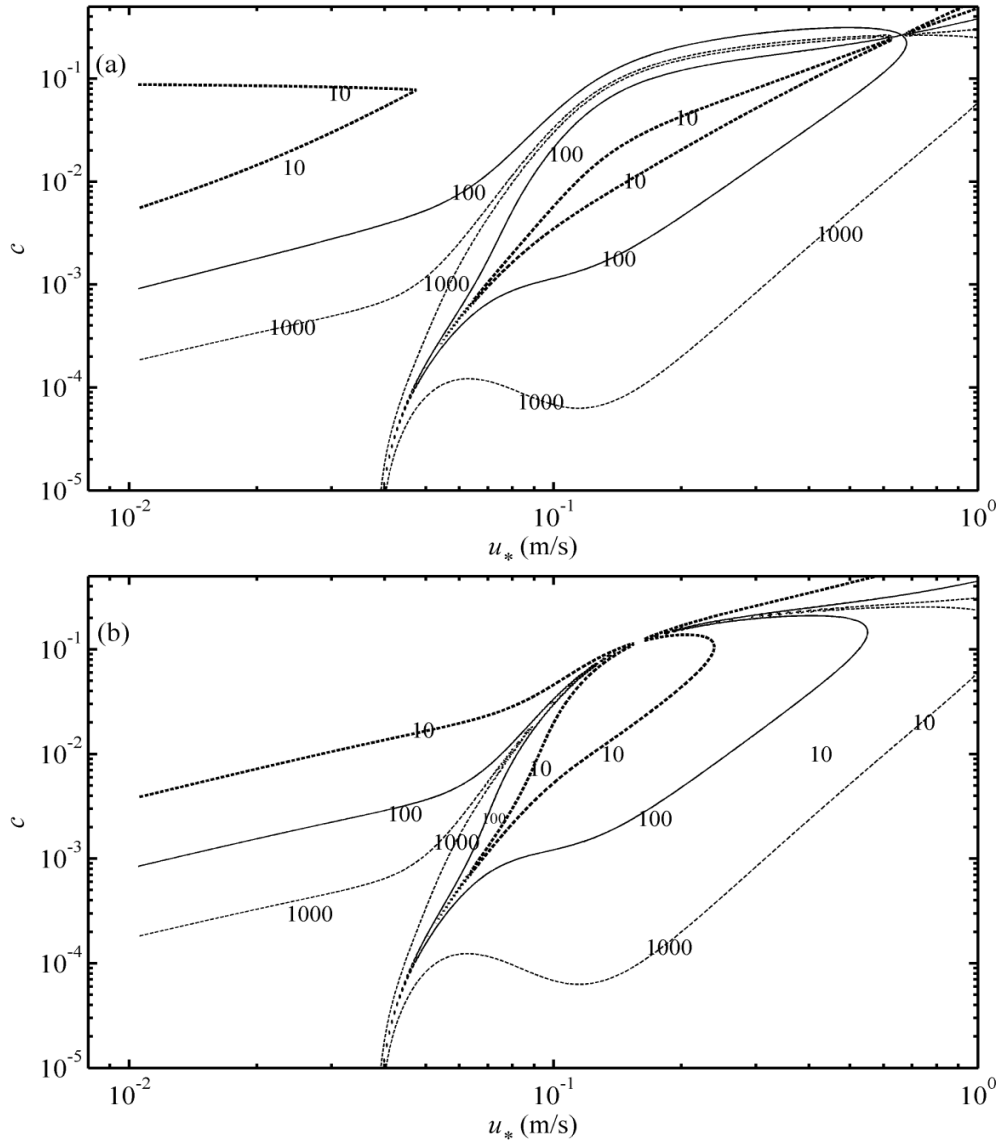

Figure 4. 7 Impact of spatial gradient of sediment concentration with (a) $\partial c/\partial x$ **= -0.0003 and** S_{bx} **= 0.008; (b)** $\partial c/\partial x$ **= -0.0003 and** S_{bx} **= 0.001: contours of** T_b/T_h **along the** λ_1**-characteristic.**

These critical values of T_b/T_h in Table 4.1 may not be generally applicable and need to be substantiated through further studies. For example, in the right and bottom (RB) of the $u_* - c$ plane in Figure 4.4, T_b/T_h is greater than 1000. However, in the RB, T_b is smaller than 500 as seen in Figure 4.3, representing a very fast rate of bed deformation, which may induce a strong feedback impact of bed deformation on the current evolution. These

analyses all pertain to time scales under static conditions. Further computational case studies of self-accelerating turbidity currents are presented below to complement these analyses.

4.2. Self-Accelerating Turbidity Currents

Numerical modelling of self-accelerating turbidity currents was first presented by Fukushima *et al*. (1985) and Parker *et al*. (1986) in their study of the Submarine Scripps Canyon. Six mathematical models are applied to the self-accelerating turbidity currents and numerical comparisons are conducted to complement the analysis of static time scales. For a model summary, one can refer to Table 2.1 in Chapter 2. Following Fukushima *et al*. (1985) and Parker *et al*. (1986), the following values of the relevant parameters are specified: S_{bx} = 0.08, p = 0.4, d = 0.15 mm, ω = 0.0165 m/s, ρ_s = 2650 kg/m^3, c_D = 0.004 for the models using a constant value for the bed drag coefficient (FCM, PCM, TEM), whereas α = 0.1 and c_{D*} = 0.004 for the models using the turbulent energy constraint (FCMK, PCMK, FEM). The computational reach is set to be 3500 m. The upstream boundary conditions are prescribed as h_0 = 3.0 m, u_0 = 1.24 m/s, c_0 = 0.005. Based on grid-convergence tests, spatial step Δx = 0.25 m and Cr = 0.9 are applied. Specifying both the turbidity current thickness and velocity at the inlet boundary (x = 0 m) is appropriate because the densimetric Froude number ($Fr_0 = u_0 / \sqrt{Rgc_0 h_0}$) at the inlet boundary is equal to 2.52, greater than unity. Numerical modelling is performed within the time period before the front of turbidity currents reaches the downstream boundary, for which the boundary conditions can be simply set at the initial static condition.

4.2.1 Reproducing self-accelerating turbidity currents

Figure 4.8 shows the longitudinal velocity profiles computed by the six models summarized in Table 2.1, and Figure 4.9 shows the sediment discharge profiles. Sediment concentration profiles from the six models are illustrated in Figure 4.10. From Figs. 4.8-4.10, the following are identified. A dip in the velocity computed by FCM and PCM is seen in the immediate vicinity of the inlet boundary (Figure 4.8a, b, c, d). As the energy constraint is incorporated in FCMK and PCMK, the dip essentially disappears. Apart from the dip in

velocity by FCM and PCM, as the currents propagate downstream, the velocities and sediment discharges from the six models increase monotonously (Figs. 4.8 and 4.9). Recall the definition by Fukushima *et al*. (1985) and Parker *et al*. (1986) that the currents are self-accelerating if the velocity and sediment discharge eventually increase monotonically in the downstream direction. Therefore, Figs. 4.8 and 4.9 actually demonstrate the ability of the six models (Table 2.1) to reproduce self-accelerating turbidity currents. As the currents propagate forward, the velocities increase (Figure 4.8), thus the currents can entrain more sediment from the bed than they lose through deposition, becoming heavier as characterized by the increase in sediment concentration (Figure 4.10) and increasing the term $-RgchC_f\partial z/\partial x$ that quantifies the driving force of the currents. As a result, self-acceleration is generated, triggering active sediment transport (Figure 4.9).

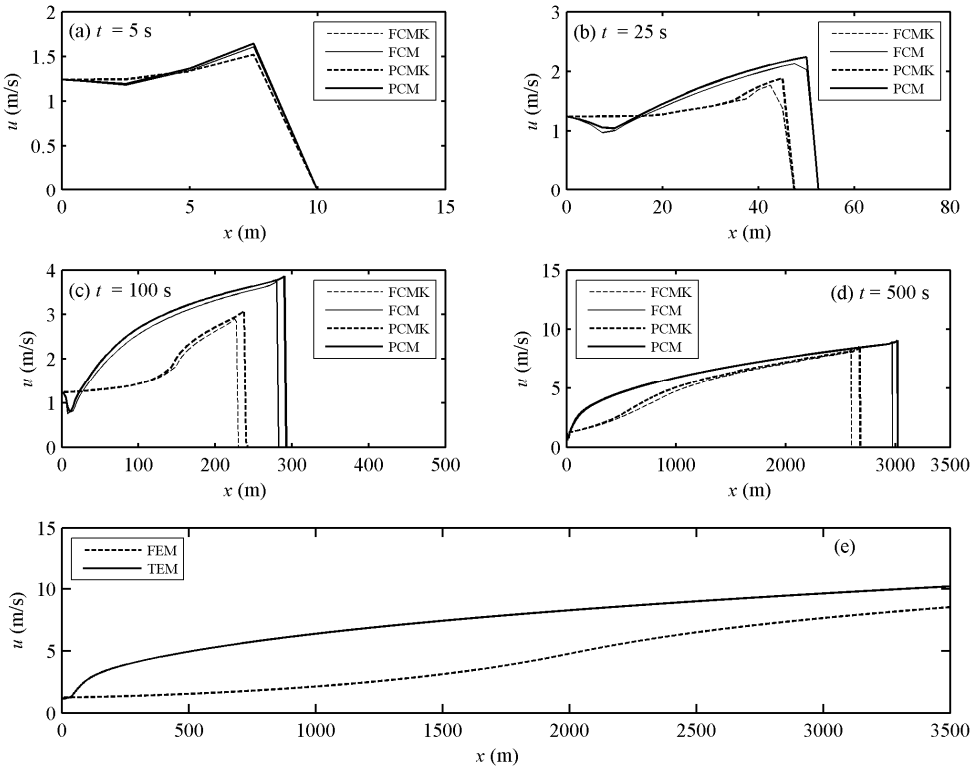

Figure 4. 8 Current velocity profiles versus down-canyon distance: (a, b, c, d) from the fully and partially coupled models with c_D determined empirically (FCM, PCM) and c_D linked to a turbulent constraint (FCMK, PCMK), respectively; (e) from the three equation model (TEM) and four equation model (FEM). See Table 2.1 for the differences of these models.

There exist remarkable differences among the solutions of the six models. Firstly, PCM produces appreciably higher velocity and sediment concentration than FCM (Figs. 4.8 and 4.10). Sediment discharge from PCM is slightly different from that of FCM (Figure 4.9). These observations also hold true for PCMK compared to FCMK (Figs. 4.8-4.10). Secondly, the differences are considerable between the models with (FCMK, PCMK and FEM) and without (FCM, PCM and TEM). The velocity and sediment discharge from FCMK are markedly lower than those from FCM (Figs. 4.8 and 4.9), except for the dip in velocity close to the inlet boundary from FCM. The comparison between PCMK and PCM is in principle similar to that between FCM and FCMK. The velocity, sediment discharge and sediment concentration from FEM are significantly lower than those from TEM (Figs. 4.8e, 4.9e and 4.10e), concurring with the finding by Parker *et al*. (1986). Finally, the numerical results from TEM feature higher velocity, sediment discharge and sediment concentration than those from FCM at t = 500 s (Figs. 4.8e, 4.9e, 4.10e), whereas the inverse is seen for FEM in comparison to FCM. These differences will be further addressed and the potential causes are interpreted in the following.

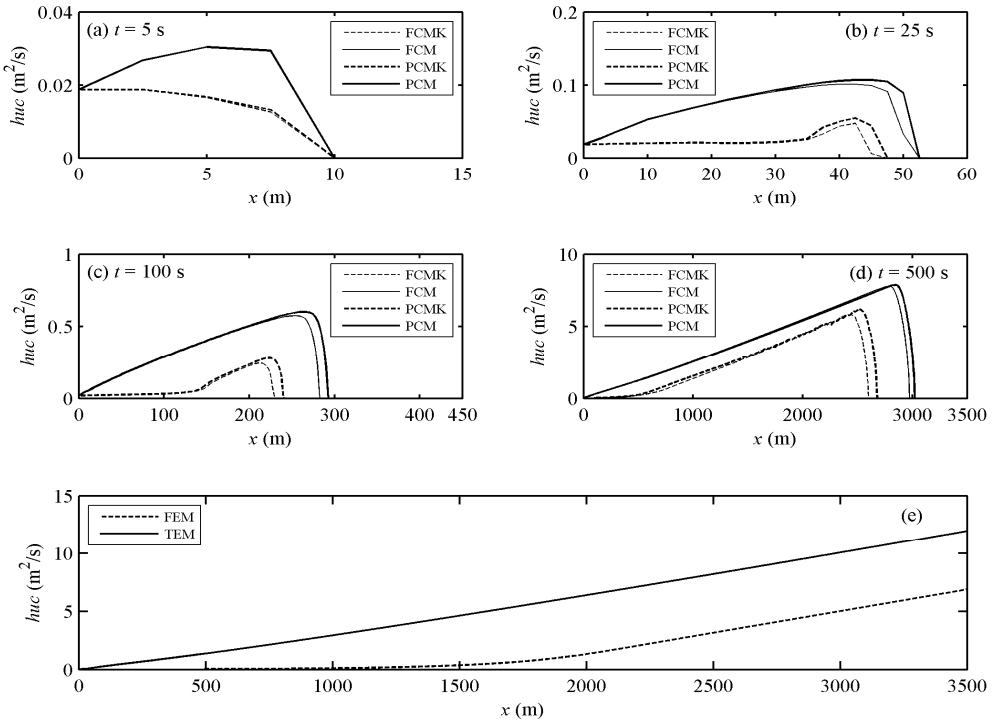

Figure 4. 9 Sediment discharge profiles versus down-canyon distance from FCM, PCM, FCMK, PCMK, TEM and FEM.

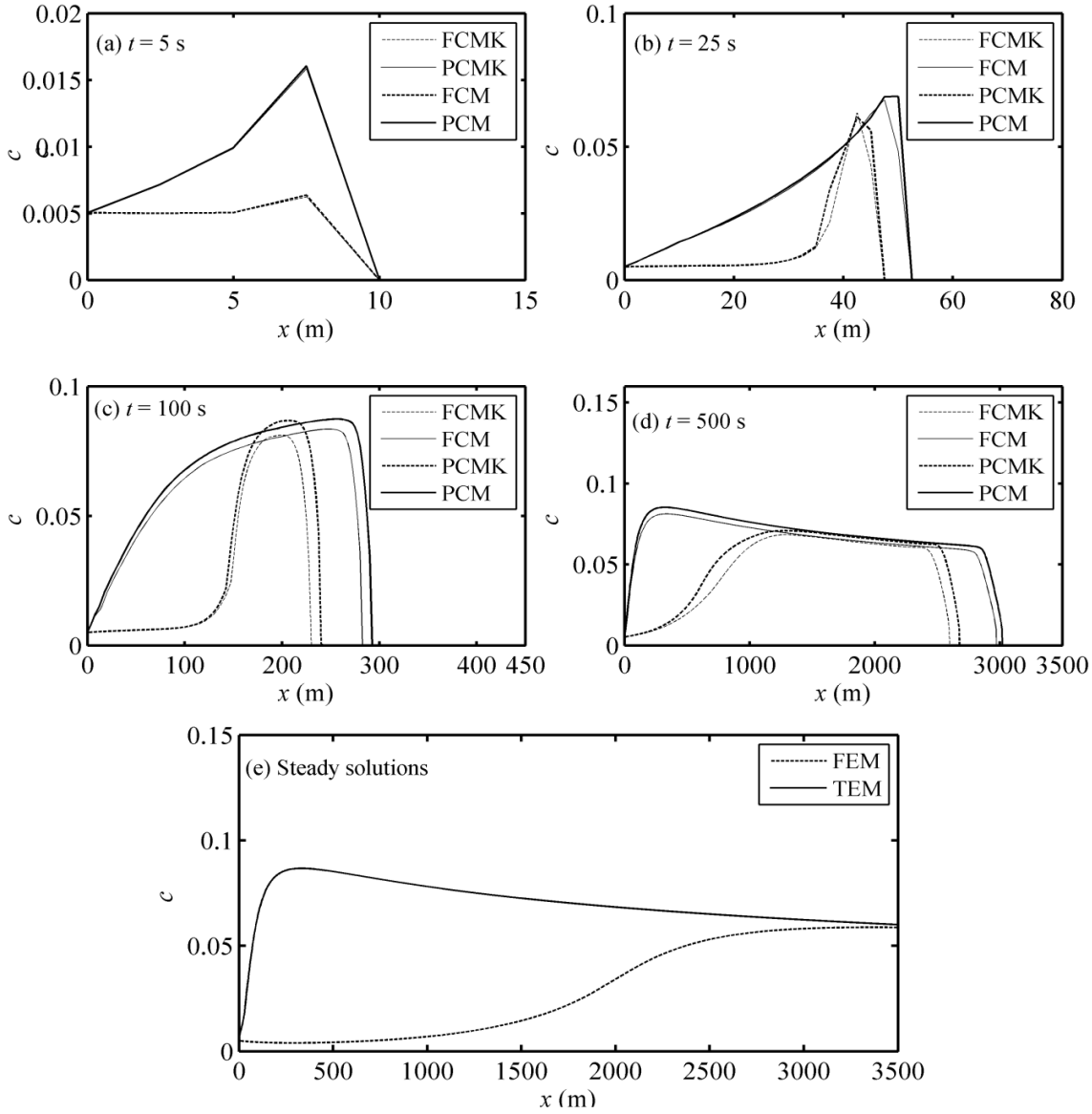

Figure 4. 10 Sediment concentration profiles versus down-canyon distance from FCM, PCM, FCMK, PCMK, TEM and FEM.

4.2.2 Feedback impacts of bed deformation

Figs. 4.11 and 4.12 illustrate respectively the longitudinal profiles of turbidity current thickness and bed scour depth $\Delta z = z(x,t) - z(x,0)$ at selected instants from the fully and partially coupled models. From Figure 4.11, partially coupled models feature detectably smaller turbidity current thickness than the fully coupled models (PCM versus FCM, and PCMK versus FCMK). When seeking the potential causes of these differences along with

those in velocity, sediment discharge and sediment concentration, one may refer to the momentum transfer due to water entrainment, which is neglected in partially coupled models (PCM and PCMK). By numerical experiments, however, it is observed that the influence of momentum transfer due to water entrainment is actually negligible (not shown). Therefore, the differences between the fully and partially coupled models can only be ascribed to the coupling terms in the governing equations, which represent the feedback impacts of bed deformation. They are explained as follows.

Physically bed degradation (Figure 4.12) would lead to an increase in the total mass of sediment carried by the turbidity currents. However, by PCM, the increase in the total mass of sediment is not accounted for in the total mass of the water-sediment mixture because the second term in the RHS of the mass conservation equation Eq. (2.5) or (2.7) of the water-sediment mixture is neglected. Its net effect is an underestimation of the current thickness by PCM (Fig 4.11) and thus an overestimation of the current velocity ($u = hu / h$, Figure 4.8) and sediment concentration ($c = hc / h$, Figure 4.10) by PCM as compared to FCM, which in turn gives an overestimation of driving force and thus faster advancing of the current front, as seen in Figs. 4.8 - 4. 10. Not surprisingly, when the current velocity, sediment concentration and the current thickness are combined together (sediment transport rate: huc, Figure 4.9), the difference between FCM and PCM appears negligible. The computed bed scour depth by PCM is generally greater than that by FCM (Figure 4.12) due to the overestimation of the current velocity by PCM. This explanation also applies to the numerical difference between FCMK and PCMK.

Indeed, in the initial period (say, $t < 5$ s), the differences between the fully and partially coupled models are essentially negligible, in respect of that the currents have not been sufficiently swift and the bed deformation is mild (Figs. 4.8-4.10(a)). As turbidity currents propagate downstream and accelerate, they become sufficiently swift and heavier, resulting in active sediment transport and rapid bed deformation (Figs. 4.9 and 4.12). Mostly notably, the bed scour depth is not negligible compared to turbidity current thickness as shown in Figs. 4.11(c, d) and 4.12(c, d).

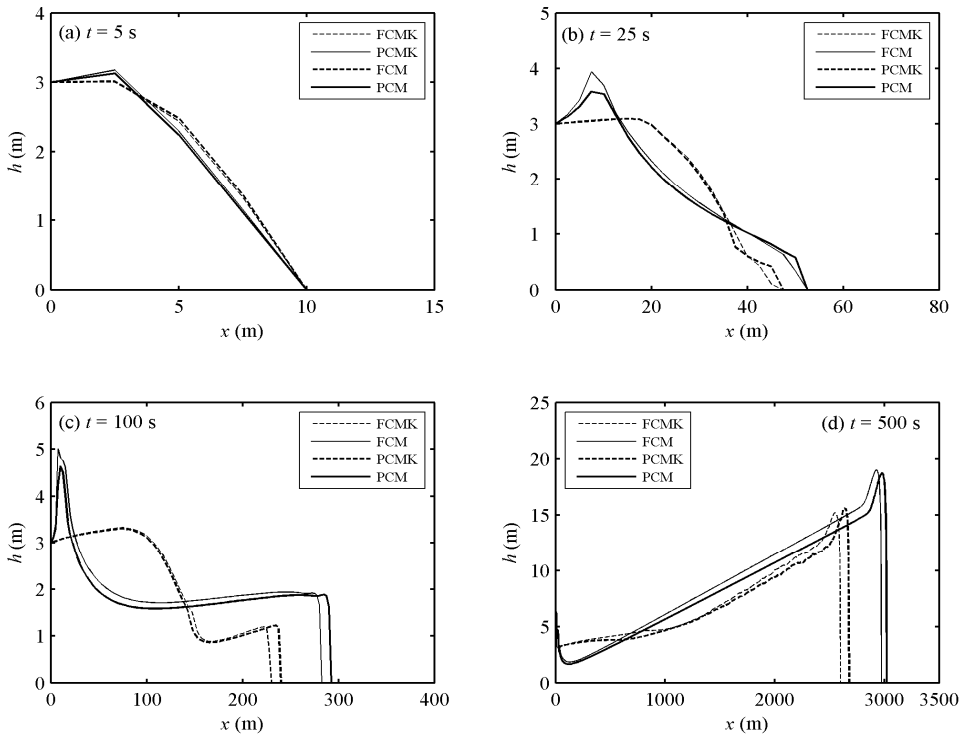

Figure 4. 11 Turbidity current thickness versus down-canyon distance from FCM, PCM, FCMK and PCMK at four times.

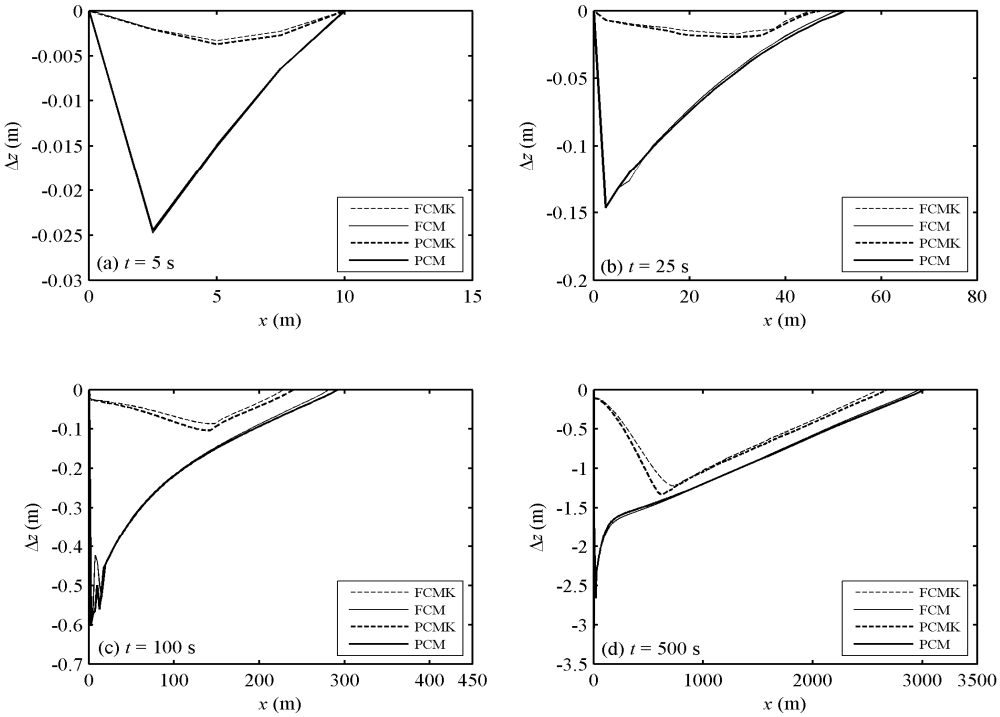

Figure 4. 12 Bed scour depth versus down-canyon distance from FCM, PCM, FCMK and PCMK at four times.

The above observations follow that fully coupled modelling with the complete governing equations is essential for refined resolution of turbidity currents featuring active sediment transport and rapid bed deformation. In support of this argument, the relative time scale of bed deformation at selected cross sections along the λ_1-characteristics is shown in Figure 4.13 (that along the λ_2-characteristics is similar and thus not shown). The value of T_b/T_h is consistently lower than 100, corresponding to the RBD regime as in the analysis of static time scales. This indicates that the fully coupled modelling must be employed for self-accelerating turbidity currents. These are also backed up by the significant differences (Figs. 4.8-4.10) between the solutions of the decoupled and fully coupled models (TEM versus FCM, and FEM versus FCMK), although these are partly ascribed to the steady flow approximation in TEM and FEM.

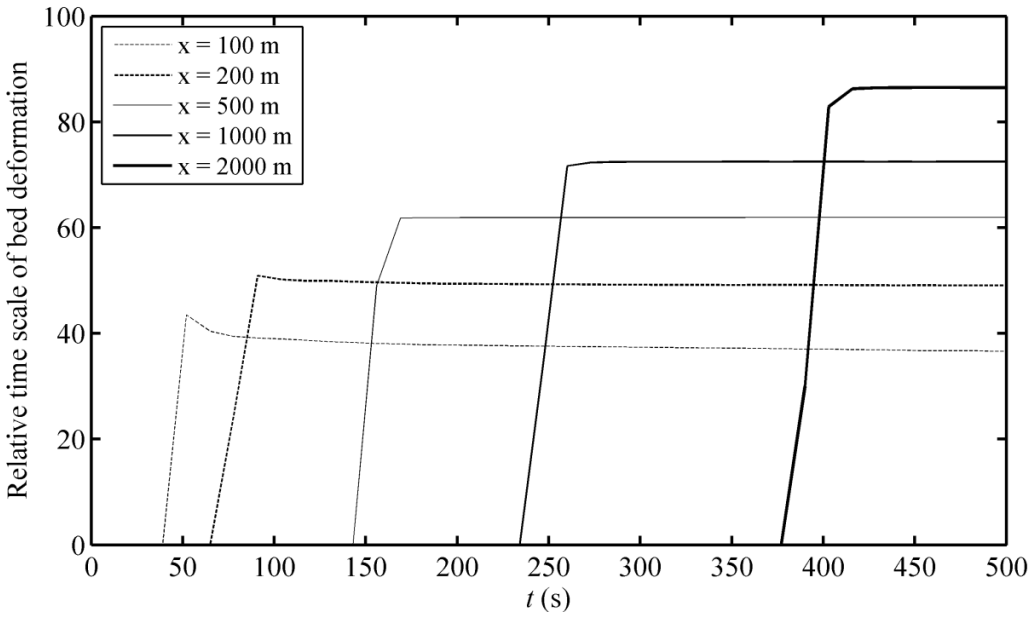

Figure 4. 13 Relative time scale T_b/T_h of bed deformation along the λ_1-characteristics at selected cross sections.

4.2.3 Effect of the steady flow approximation

To further address whether the steady flow approximation is applicable or not, the constituent contributions of the temporal and spatial changes to the momentum conservation of turbidity currents, along with their ratio, are defined respectively as

$$TC_t \equiv \frac{\partial hu}{\partial t}\ ,\ TC_x \equiv \frac{\partial}{\partial x}(hu^2 + \frac{1}{2}Rgch)\ ,\quad R_{tx} = \frac{TC_t}{TC_x} \qquad \text{(4.10a, b, c)}$$

If turbidity currents are steady or weakly unsteady, the value of R_{tx} would be infinitesimal and thus the turbidity currents can be modelled with the steady flow assumption. On the contrary, if the value of R_{tx} is considerable, unsteady flow models must be used. Figure 4.14 shows the longitudinal profiles of R_{tx} at selected times from FCM. From Figure 4.14 it can be seen that the value of R_{tx} near the front of the turbidity currents can be far larger than 0.1, and R_{tx} within the body of the currents may not be negligibly small (say, smaller than 0.05). Alternatively, the contribution of the temporal change to the evolution of the turbidity currents is not negligible, the front of turbidity currents is highly time-dependent, and the body part may not be sufficiently steady. The implication of this observation is apparent, i.e., the steady flow approximation involved in models TEM and FEM is not justified, which may have to a certain extent contributed to the significant differences (Figs. 4.8-4.10) between the solutions of the decoupled and fully coupled models (i.e., TEM versus FCM, and FEM versus FCMK).

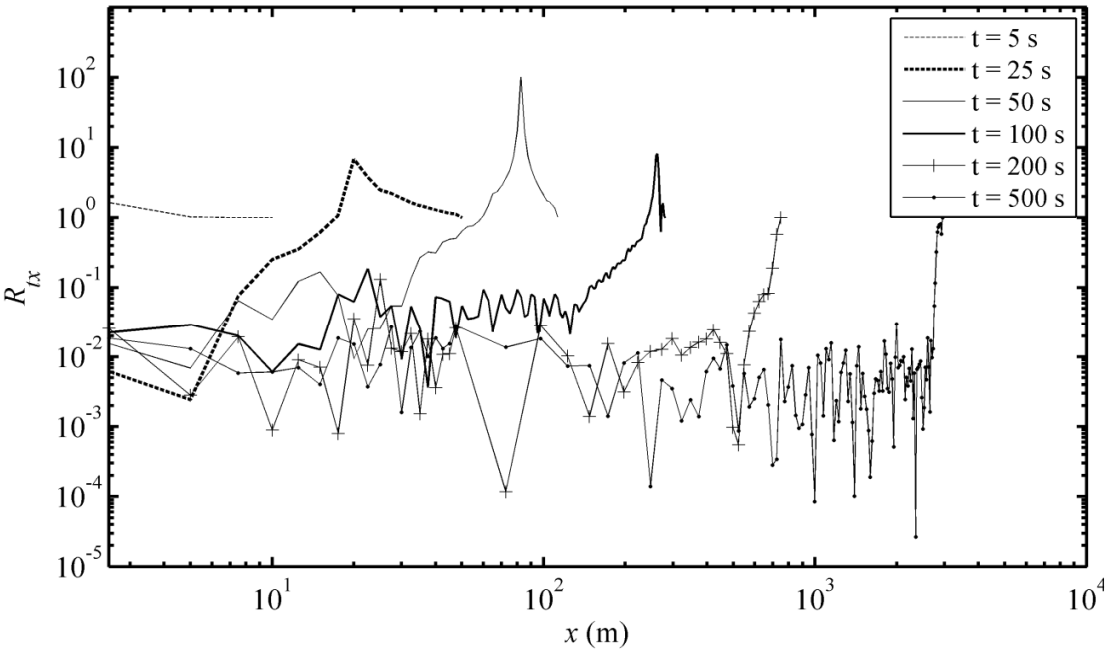

Figure 4. 14 Ratio of temporal to spatial change from FCM.

4.2.4 Impact of the conservation of mean turbulent energy

Fukushima *et al*. (1985) and Parker *et al*. (1986) stated that self-acceleration computed by TEM was physically unrealistic, and accordingly FEM was developed by incorporating the conservation of mean turbulent energy. Figure 4.15 presents the bed shear velocity profiles computed by FCM and FCMK. From Figure 4.15, it is observed that the bed shear velocity of FCMK is generally much smaller than that of FCM, implying greatly confined sediment entrainment flux for FCMK in comparison to FCM. This is also the case for PCMK and PCM, though not shown. Consequently, the bed scour depth computed by FCMK and PCMK is found to be greatly subdued compared to those computed by FCM and PCM (Fig 4.12). This observation along with the differences between the velocity, sediment discharge, sediment concentration and current thickness profiles from FCM and FCMK, or PCM and PCMK (Figs. 4.8, 4.9, 4.10 and 4.11) lead to the conclusion that incorporating the turbulent energy constraint would greatly modify the evolution of turbidity currents.

While the impacts of the mean turbulent energy constraint on the evolution of turbidity current are considerable in relation to the prescribed parameters following Fukushima *et al*. (1985) and Parker *et al*. (1986), uncertainty must not be ignored with Eqs. (2.14) and (2.15), especially the term related to bed resistance (as represented by bed shear velocity u_*). This is because the physics of turbulent turbidity currents has to date remained far from clear (Kneller and Buckee 2000). It is not surprising as one recalls that even for single-phase clear-water flow, the estimation of bed resistance bears much uncertainty. Here the impacts of the mean turbulent energy constraint Eqs. (2.14) and (2.15) on the evolution of turbidity current are examined by a series of numerical tests with a presumed set of values of parameter α, as the magnitude of the parameter α plays a key role in confining sediment entrainment flux and therefore affects current evolution.

The numerical modelling and the statements in the above text are all based on $\alpha = 0.1$ following Fukushima *et al*. (1985) and Parker *et al*. (1986). According to Fukushima *et al*. (1985) and Parker *et al*. (1986), the variation of α exhibits little influence on numerical solutions of FEM. Here numerical modelling tests of FCMK are performed with values of α varied (quite conservatively) by an order of magnitude around 0.1 (Fukushima *et al*.

1985; Parker *et al*. 1986), i.e., α = 0.01, 0.05 and 1.0. Figs. 4.16, 4.17, 4.18 and 4.19 illustrate the current velocity, sediment concentration, current thickness and bed scour depth profiles respectively, along with the results from FCM. It is observed from Figs. 4.16 to 4.19 that as α varies, the solutions of FCMK exhibit great changes, and yet the differences between FCMK solutions and that from FCM always appear to be considerable within the range of α considered. Therefore, the role of the mean turbulent energy constraint in modifying the evolution of turbidity currents should be interpreted with due caution. Also in this connection, its role must not be confused with the impact of the fully coupled modelling.

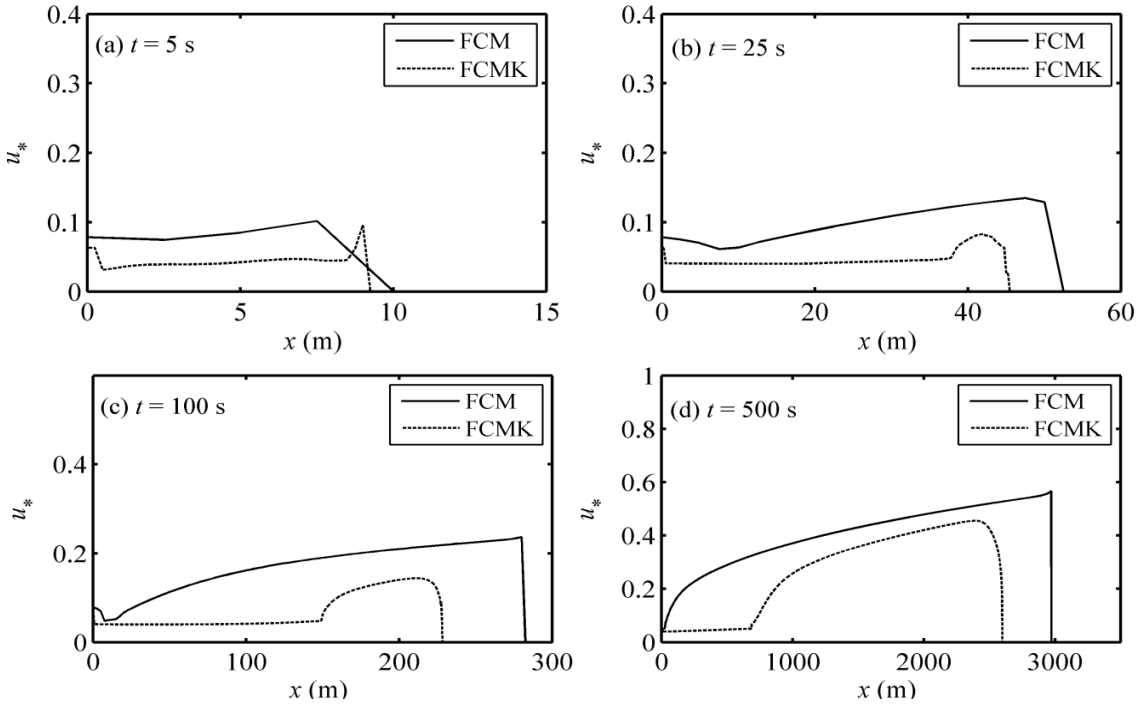

Figure 4. 15 Bed shear velocity profiles versus distance from FCM and FCMK with α = 0.1 at four instants.

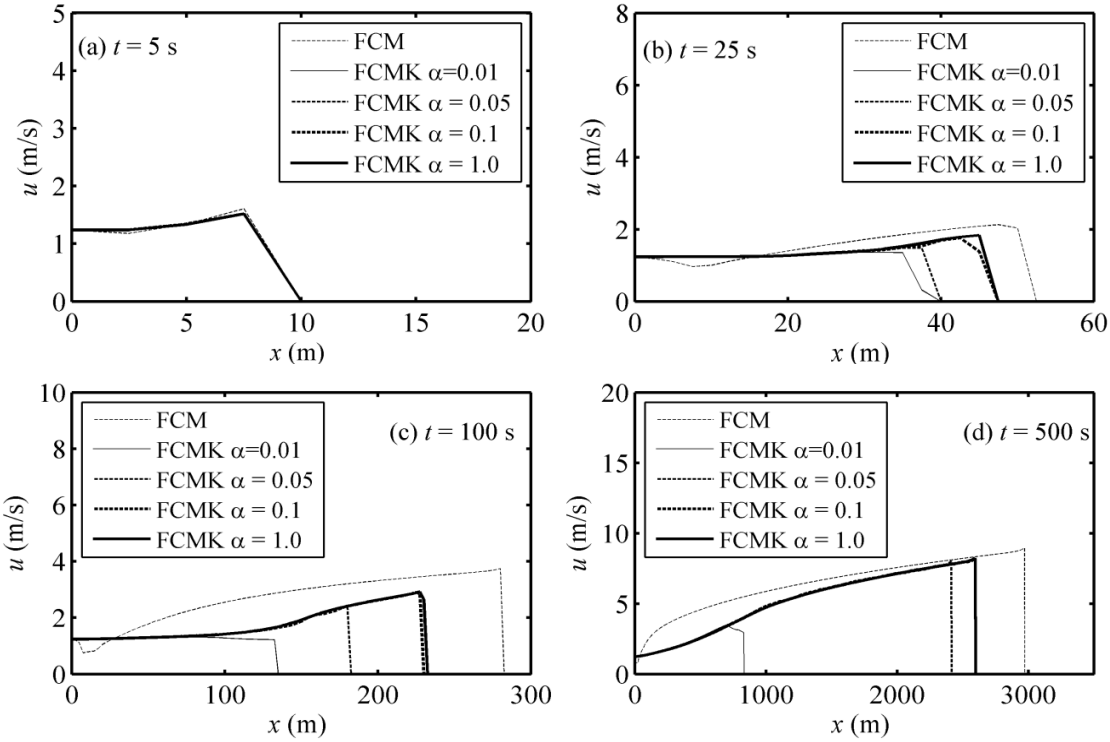

Figure 4. 16 Velocity profiles versus distance from FCM and FCMK with α = 0.1 at four instants.

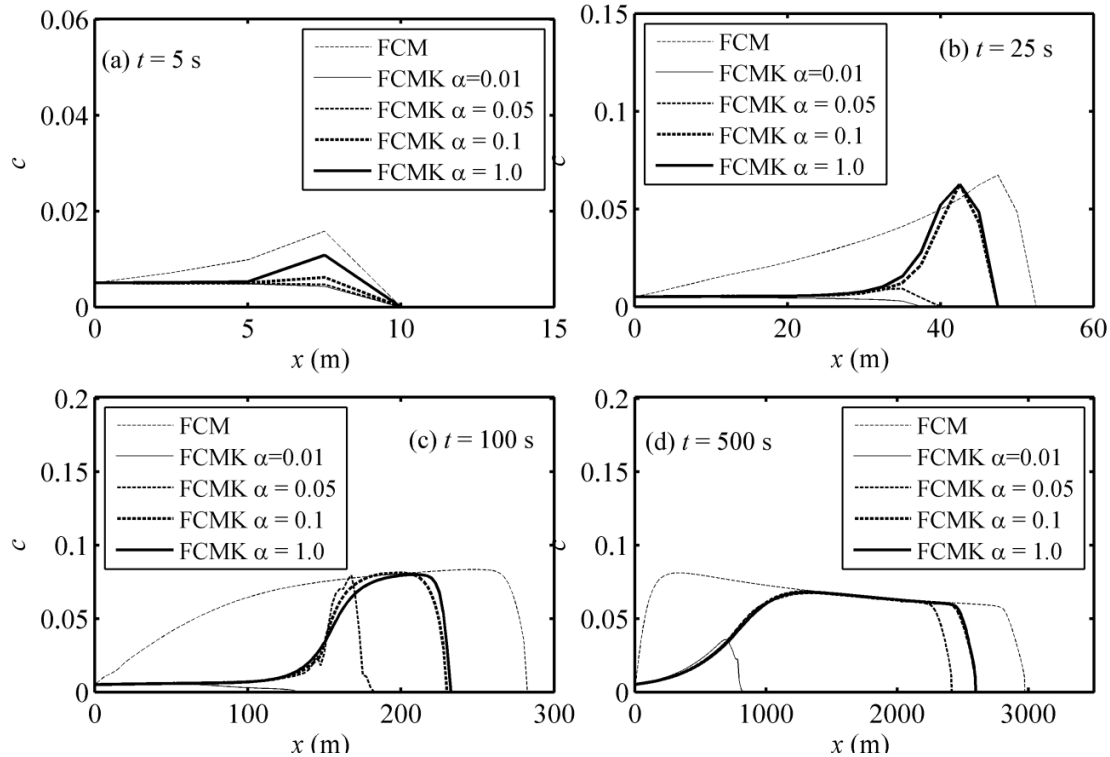

Figure 4. 17 Sediment concentration profiles versus distance from FCM and FCMK with α = 0.1 at four instants.

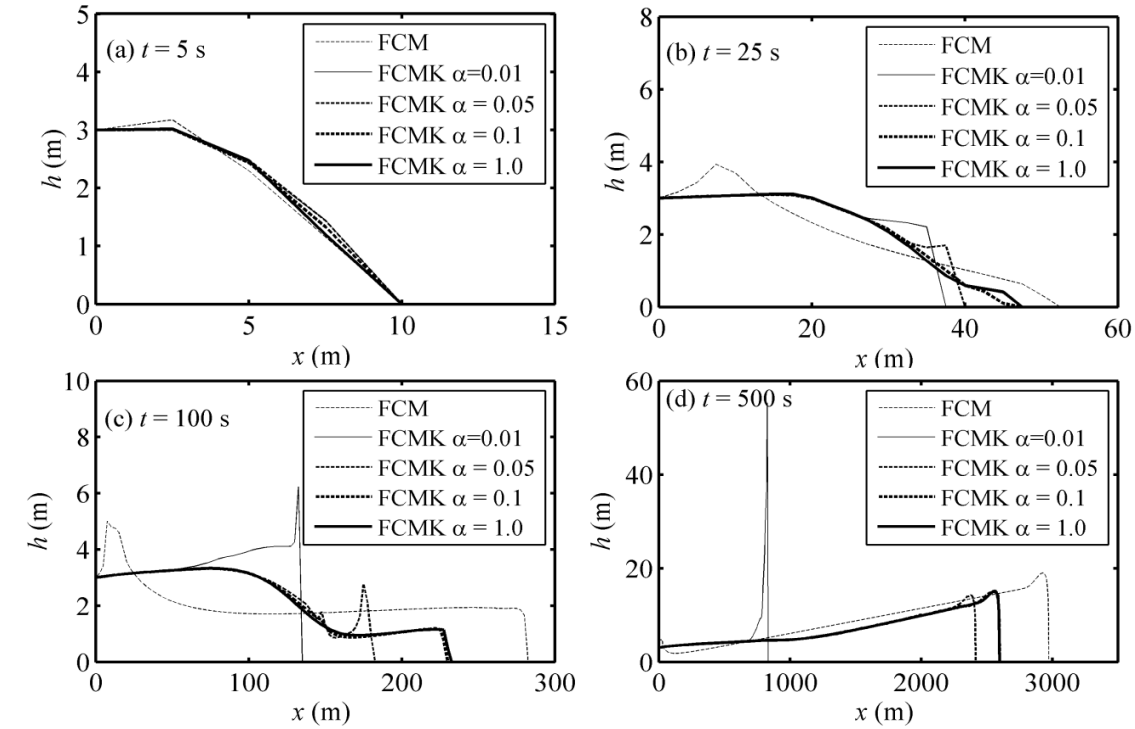

Figure 4. 18 Current thickness profiles versus distance from FCM and FCMK with α = 0.1 at four instants.

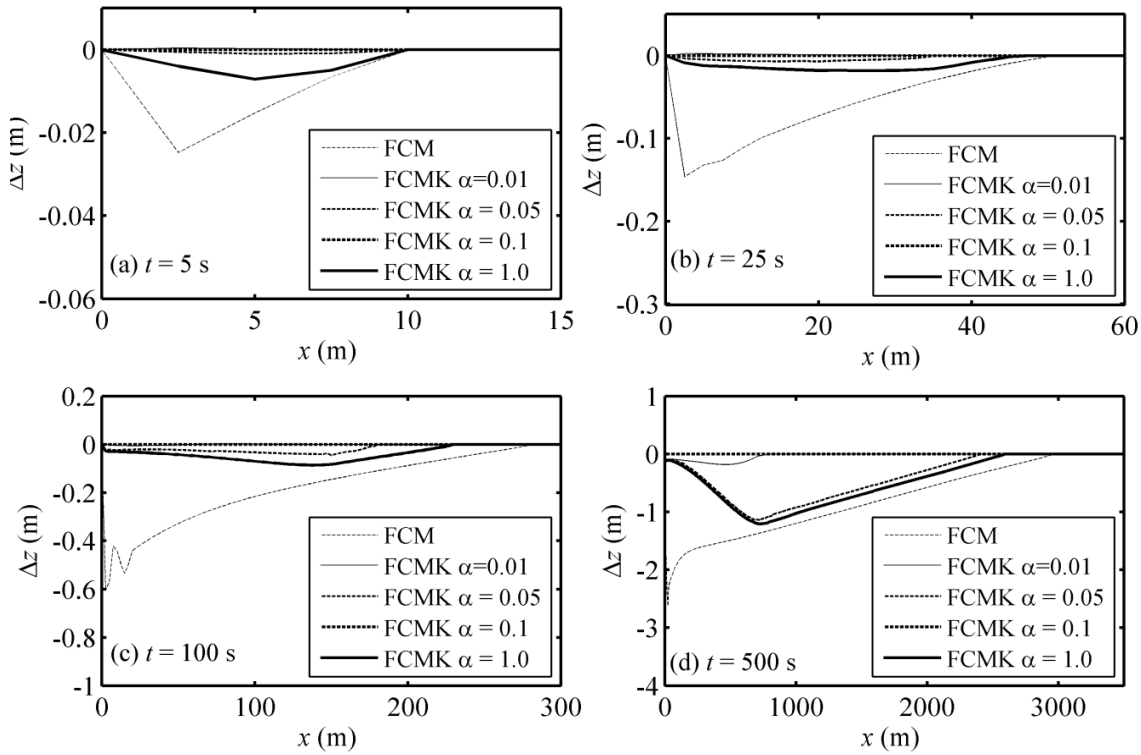

Figure 4. 19 Bed scour depth profiles versus distance from FCM and FCMK with α = 0.1 at four instants.

4.3 Conclusions

The fully coupled model is capable of reproducing self-accelerating turbidity currents. The discrepancies compared to decoupled and partially coupled models are ascribed to the simplification of the governing equations and assumptions. The use of the complete governing equations does not result in any essential increase in computing cost, because fully coupled modelling differs from the partially coupled modelling only in that the coupling source terms are incorporated in the former, which are only algebraic functions of unknown physical variables. Fully coupled modelling is essential for those turbidity currents featuring active sediment transport and rapid bed deformation, and existing simplified models need to be reformulated. The mean turbulent energy constraint, which confines the sediment entrainment flux through depressing the bed shear velocity, can considerably modify the evolution of turbidity currents. However, it should be used with due caution because the understanding of turbulence-sediment interaction remains far from clear, and its impact on the evolution of turbidity currents must not be confused with that of the fully coupled modelling. The steady flow assumption is open to question, and unsteady flow models are appropriate since the contribution of temporal change is considerable in the front of turbidity currents.

Chapter 5. EFFECTS OF TURBIDITY CURRENTS ON SUBMARINE MORPHOLOGICAL FEATURES

Summary

- Submarine turbidity currents and the formation of the associated morphological features (canyons, channel-levee and lobes on fans) are resolved by the fully coupled model
- Fully coupled modelling is shown to be critical for refined modelling quality
- Impacts of key factors dictating the incipient formation of channel-levee morphology on submarine fans are investigated systematically

Submarine turbidity currents have been recognized to be responsible for the formation of submarine morphological features (canyons, channels, levees, gullies and sediment waves etc) (Cofaigh *et al*. 2006; Dykstra and Kneller 2008). Previous investigations are mostly based on back-calculations from the observed morphological features and small-scale laboratory experiments as well as qualitative linear stability analyses, which cannot resolve the processes by which turbidity currents affect morphological evolution. In this chapter, submarine turbidity currents near a submarine canyon-fan transition and over submarine fans are investigated numerically using the fully coupled model. Particular attention is paid to the feedback impact of bed deformation on the current and morphological evolution and key factors dictating the formation of submarine channel-levee morphology.

5.1 Turbidity Currents near Submarine Canyon-fan Transition

Submarine canyon-fan transitions are usually characterised by abrupt decreases in the bed slope. Self-accelerating turbidity currents in the canyon portion may become subcritical and diminish around the bed slope break through an 'internal hydraulic jump'. Previous studies on turbidity currents near the submarine canyon-fan transition include indirect back-estimation based on depositional features (Weirich 1988), small scale laboratory flume experiments (e.g., Garcia and Parker 1989; Garcia 1993; Mulder and Alexander 2001) and 1D analyses based on many assumptions and simplifications (Komar 1971; Kostic and Parker 2006, 2007). An event of 2D turbidity currents around a slope break is investigated numerically by Bradford and Katopodes (1999a, b), yet a relatively small computational domain is considered and a partially coupled model is used, by which the process is insufficiently addressed and revealed. Here the case of turbidity currents around a slope break is numerically revisited in this section using the fully coupled model (FCM).

A sketch of the computational domain is shown in Figure 5.1. It consists of an erodible bed with initial slopes of S_{bx} = 0.1 and S_{by} = 0.0, followed by a sudden transition to a horizontal basin in the x-direction. The sloping portion is 50 m long. The inflow current enters into the domain at boundary 2-3, with the centre at coordinate (0, 0) and a width of b = 8 m. The adjacent boundaries of the upstream boundary are set as solid walls (1-2 and 3-4). The upstream boundary conditions are: h_0= 1.0 m, u_0 = 0.5 m/s, v_0= 0.0 m/s, c_0= 0.01, yielding Ri = 0.65 corresponding to supercritical flow. The computational time is 900 s. Other parameters are: p = 0.4, d = 0.09 mm, ρ_s = 2650 kg/m^3, c_D = 0.0025. Based on grid-convergence tests, Δx = 2 m, Δy = 2 m, Cr = 0.95 are applied in the computation. This case is similar to that of Bradford and Katopodes (1999b). Yet we use a much larger computational domain (400 m long and 500 m wide), as against a very small square domain of 100 m$\times$100 m employed by Bradford and Katopodes (1999b). This larger domain ensures that the current does not reach the boundaries within the computational time and thus no boundary conditions are needed. The sloping portion is designed to represent the submarine canyon, though initially no canyon morphology is superimposed. Similarly, in the horizontal portion representing the submarine fan, no morphological features typical of a submarine fan are superimposed. In presenting and

analyzing the numerical results below, attention will be paid to how turbidity currents form submarine morphological features such as canyons, channels, levees and lobes.

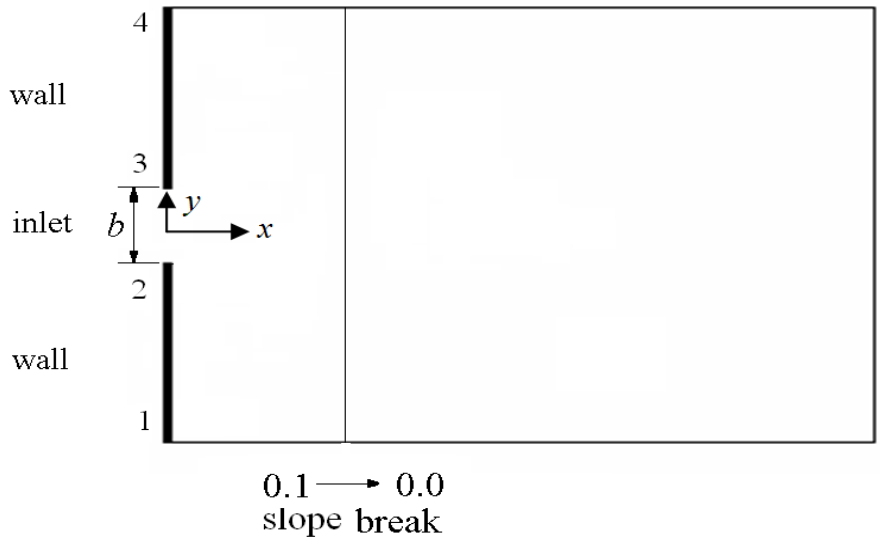

Figure 5. 1 Sketch of the computational domain.

5.1.1 Evolution of turbidity currents and formation of morphological features

Figure 5.2 illustrates the evolution of turbidity currents near the transition from FCM, as represented by the current surface position (black) and bed elevation (grey) at four times. Figure 5.3 is the same as Figure 5.2, yet the current surface is removed for clear illustration of the resultant bed morphology. Figure 5.4 shows the corresponding morphological change depth from FCM (i.e., the change of the bed elevation compared to the initial bed: $z(x,y,t)-z(x,y,0)$). The negative values in Figure 5.4 indicate bed scour; and vice versa. Figure 5.5 shows the longitudinal (along the x -direction) variations of (a) the current velocity and (b) the bulk Richardson number from the FCM at the centre of the computational domain (y = 0 m). From Figs. 5.2 – 5.5, the following can be observed.

From Figure 5.2, the downstream propagation and lateral spreading of the turbidity currents are apparent. In the upstream sloping portion (x < 50 m, S_{bx} = 0.1), downstream propagation is the main style of current evolution (t < 80 s, Figure 5.2a, b). When the current enters into the horizontal basin (x > 50 m, S_{bx} = 0.0), both downstream propagation

and lateral spreading dominate. Notably, two internal waves are formed at the two sides of the computational domain, which migrate upstream from the horizontal portion to the sloping portion. Physically the upstream migrating internal waves are due to the obstacle effect of the horizontal portion, qualitatively similar to the interval waves noted by Kneller and Buckee (2000). This indicates the ability of the present model to capture shock waves and contact discontinuities. Accordingly, turbidity currents finally occupy most of the upstream canyon portion (Figure 5.2d), though downstream propagation is the dominant current evolution style at the early stage (Figure 5.2a, b). At t = 900 s, the current occupies an area of about 300 m × 400 m (Figure 5.2d).

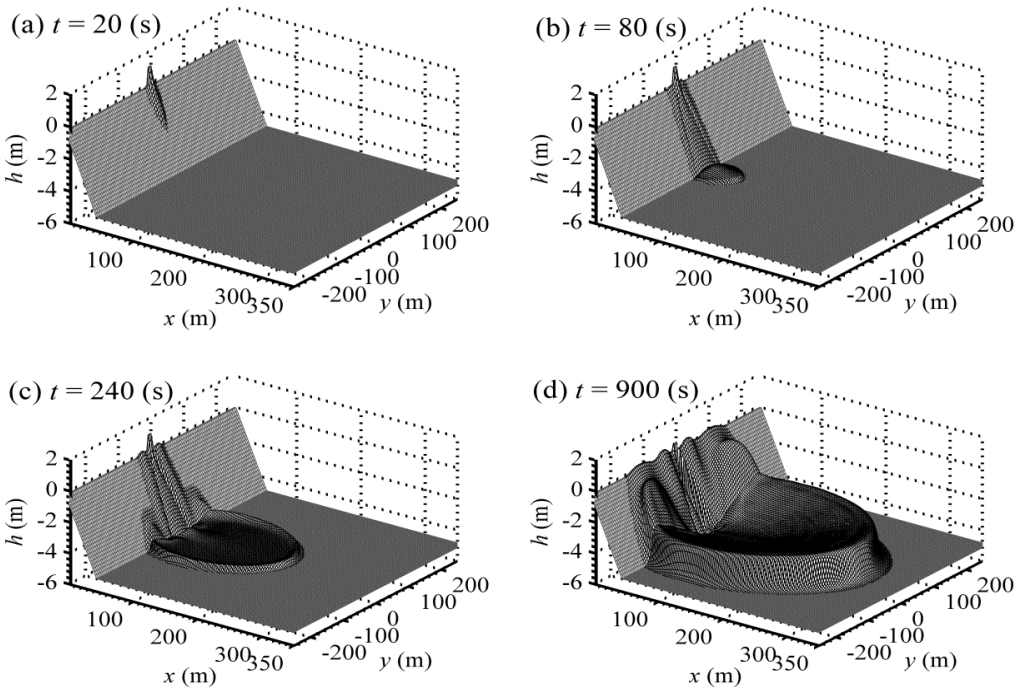

Figure 5. 2 Evolution of turbidity current from FCM: current surface (black) and bed elevation (grey) at four instants.

Along with the propagation and spreading of turbidity currents, the bottom bed deforms, as seen in Figs. 5.3 and 5.4. Yet the area with bed deformation is largely confined as compared to the area occupied by the current. In the upstream sloping portion (x < 50 m), the current appears to be self-accelerating, as evidenced by the rapid increase in current velocity along x -direction (see Figure 5.5a: the velocity increases from 0.5 m/s to about

1.5 m/s within the upstream 50 m of the sloping portion). In contrast, a self-decelerating feature is observed in the downstream horizontal portion, in which the current velocity decreases gradually with distance. Around the bed slope break, the current velocities appear to be halved abruptly. This abrupt decrease and the contrasting behaviour in the sloping and horizontal portions of the current velocity indicate the occurrence of an internal hydraulic jump for turbidity currents around the slope break. This is clearly reflected by the longitudinal variation of the bulk Richardson number (Figure 5.5b). Around x = 50 m, the bulk Richardson number exhibits a sharp increase from less than 0.5 to about 3.0-6.0 (Figure 5.5b), indicating the change of a supercritical current regime to a subcritical regime. The occurrence of internal hydraulic jump is justified and consistent with previous investigations (e.g., Komar 1971; Weirich 1988; Garcia and Parker 1989; Garcia 1993; Mulder and Alexander 2001). Both the bed slope of the sloping portion (S_{bx} = 0.1), and the particle size (d = 0.09 mm) are in the suggested range by Mulder and Alexander (2001), Kostic and Parker (2006, 2007) for the occurrence of an 'internal hydraulic jump'. The high-intensity, self-accelerating type of turbidity currents in canyons becomes depleting through the 'internal hydraulic jump' when it enters into the horizontal portion.

Not surprisingly, bed degradation is observed in the sloping portion (Figs. 5.3 and 5.4), whereas the bed scour depth decreases rapidly with distance in the horizontal portion. Sediment deposition is observed in the two lateral sides and the downstream side of the degradation region of the horizontal portion. In between the degradation and aggradation regions, there is an intermediate region, which sees negligible bed deformation. In the sloping portion, only bed scour is computed and the resultant morphology appears qualitatively similar to the observed submarine canyons, which are created by erosional turbidity currents. Similarly, the resultant morphology in the horizontal portion may represent a form of channel-levee morphology usually observed in submarine fans, with the depositional regions in the two sides being the levees, and the central erosional region being the bounded channel. Furthermore, the depositional region at the downstream side should represent a form of lobes observed in the distal part of submarine fans.

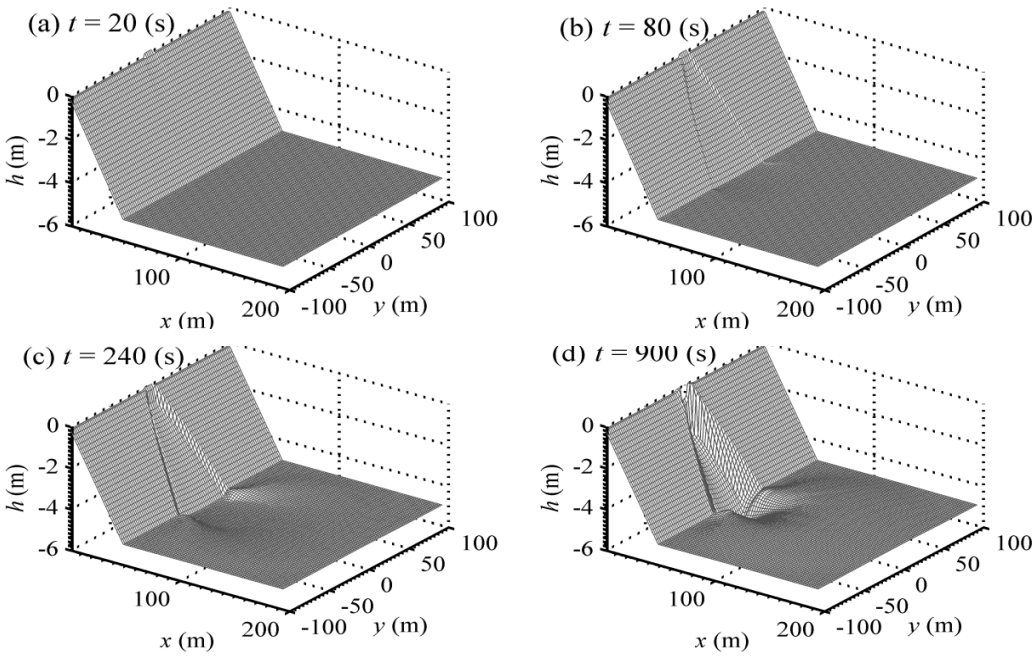

Figure 5. 3 Bed elevation at four instants from FCM.

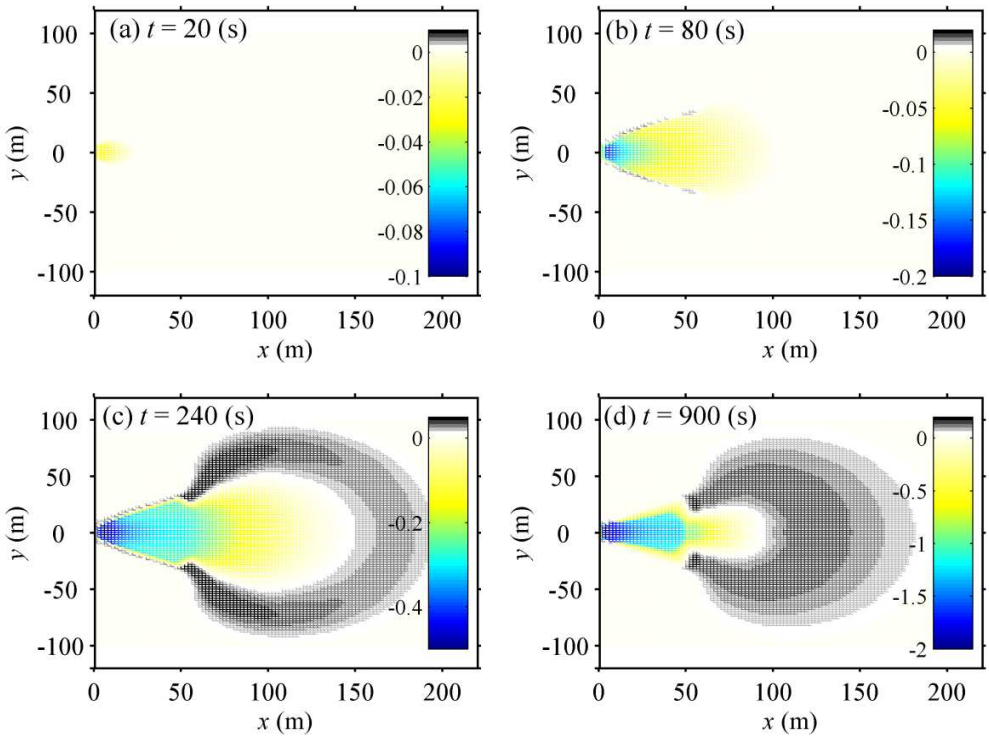

Figure 5. 4 Change of bed elevation compared to the initial bed from FCM at four instants. Negative values represent scour; and vice versa. The unit is meter.

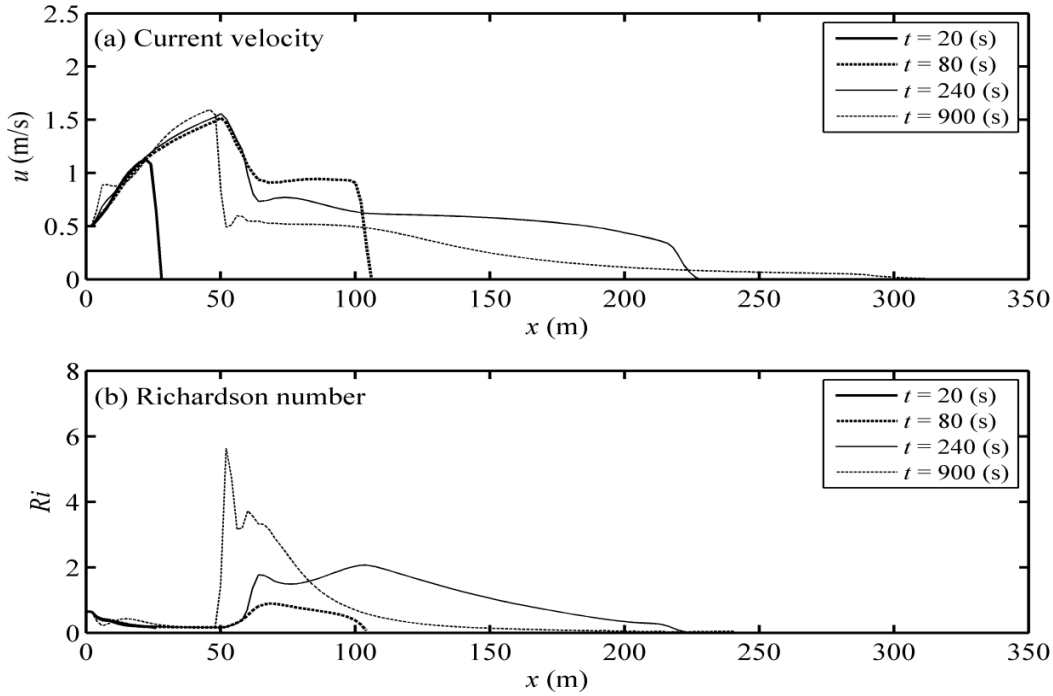

Figure 5. 5 (a) current velocity and (b) Richardson number along the centre line from FCM.

From the above observations, the evolution of turbidity currents and the morphological effects are reasonably resolved by the FCM. Over an initially flat topography (though a slope break is involved), submarine morphological features including canyons, channel-levees and lobes are produced by the fully coupled model. The present model provides an improved tool for the investigation of submarine turbidity currents, as compared to previous indirect back-estimation (Weirich 1988) and simplified 1D analysis (Komar 1971; Kostic and Parker 2006, 2007). A comparative study between mathematical modelling by the present fully coupled model and those simplified analyses would be useful and reserved for future study. Nevertheless, a detailed systematic numerical investigation of the incipient *formation of channel-levee morphology over submarine fans is presented in Section 5.2.

5.1.2 Feedback impacts of bed deformation

As seen in Figure 5.4, the maximum bed scour depth attains a value as high as 2.0 m at t = 900 (s) (Figure 5.4d), comparable to the current thickness. This may imply considerable feedback impacts of bed deformation, which can be seen in the comparisons of numerical solutions between FCM and PCM in Figs. 5.6 - 5.8. Figure 5.6 illustrates the difference in the transverse morphology between FCM and PCM at four cross sections. Figure 5.7 shows the comparison of the current surface elevation and bed elevation along x -direction at y = 0 m between FCM and PCM at four times. Figure 5.8 shows the comparison of the longitudinal variation of the sediment concentration at y = 0 m between FCM and PCM at four times. Figure 5.9 demonstrates the relative difference in the final morphology between FCM and PCM at four cross sections. Appreciable discrepancies are seen in Figs. 5.6 - 5.8, with the relative difference in bed elevation attains a value as high as 500 (Figure 5.9).

From Figure 5.7, the difference in the current front location is negligible when the time $t \leq$ 80 (s), whereas it becomes appreciable when the turbidity currents enter into the horizontal area. The negligible difference between FCM and PCM in Figure 5.7(a, b) is due to the short length of the sloping portion. Nevertheless, the sediment concentration predicted by the PCM is slightly higher than that predicted by the FCM (Figure 5.8a, b), consistent with that of self-accelerating turbidity currents in Chapter 4. The current advance predicted by the PCM is slower than that by the FCM on the horizontal basin (Figure 5.7c, d). This is because bed aggradation dominates over bed degradation (Figure 5.4c, d; Figure 5.6c, d). Net sediment deposition leads to a decrease in the total mass of sediment carried by the turbidity current, which is neglected by the PCM. The net effect is an underestimation of the sediment concentration (Figure 5.8c, d) by PCM in the horizontal portion and thus a smaller driving force. This results in the slower advance of the current front predicted by the PCM.

These follow that fully coupled modelling is critical for refined resolution of the turbidity currents and submarine morphological evolution.

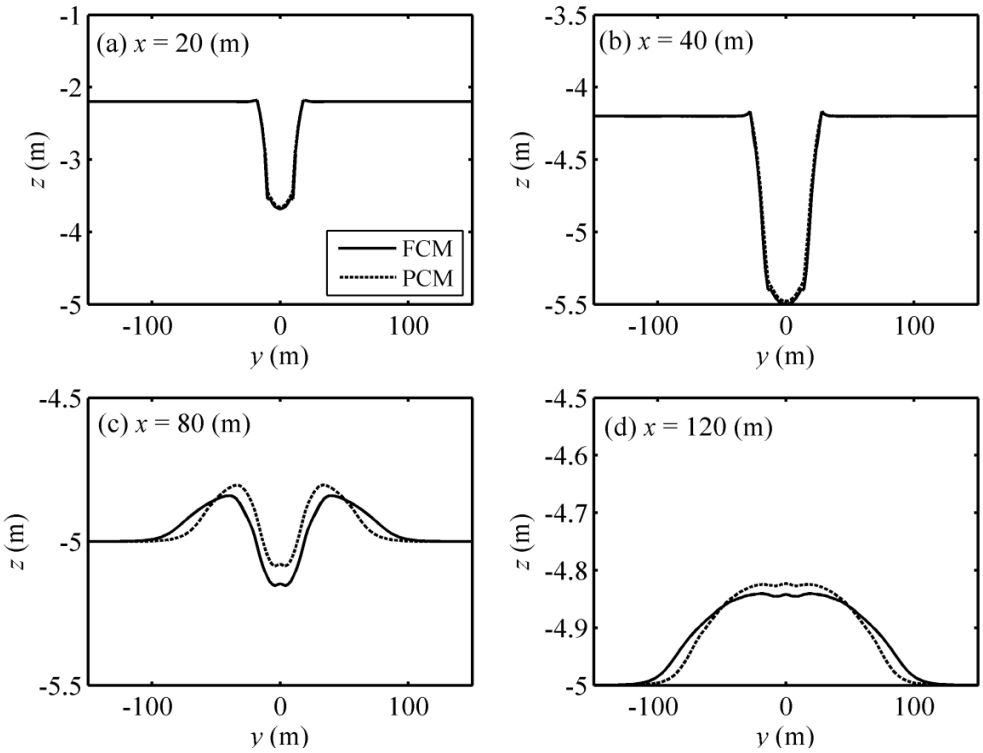

Figure 5. 6 Comparison of the cross-sectional bed elevations at different distance at t = 900 (s) between FCM and PCM.

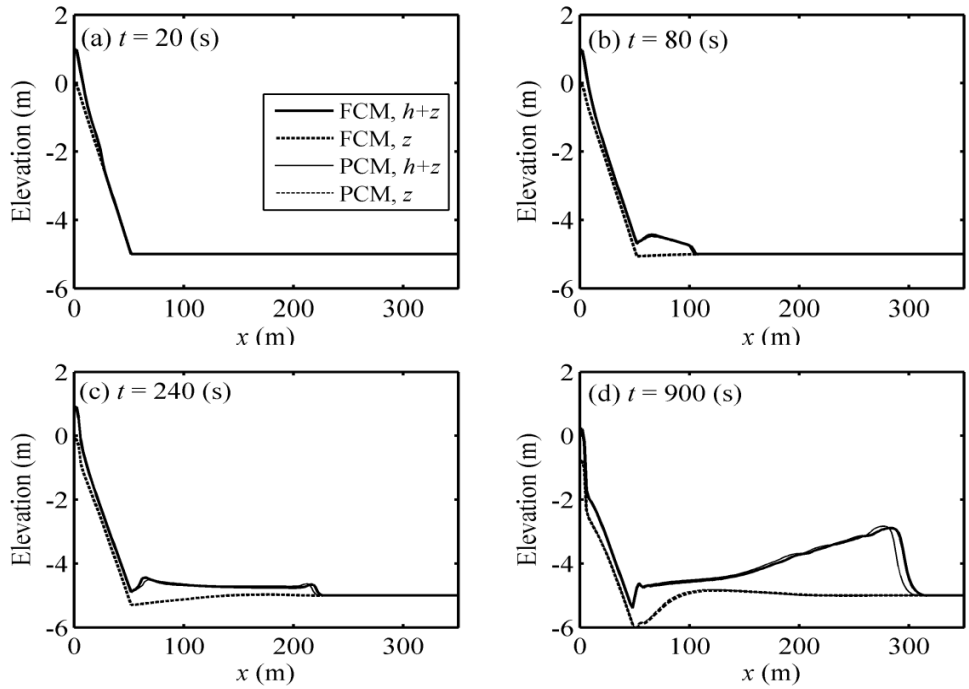

Figure 5. 7 Comparison of the longitudinal profiles of the bed and current surface elevation at y = 0 m at different time between FCM and PCM.

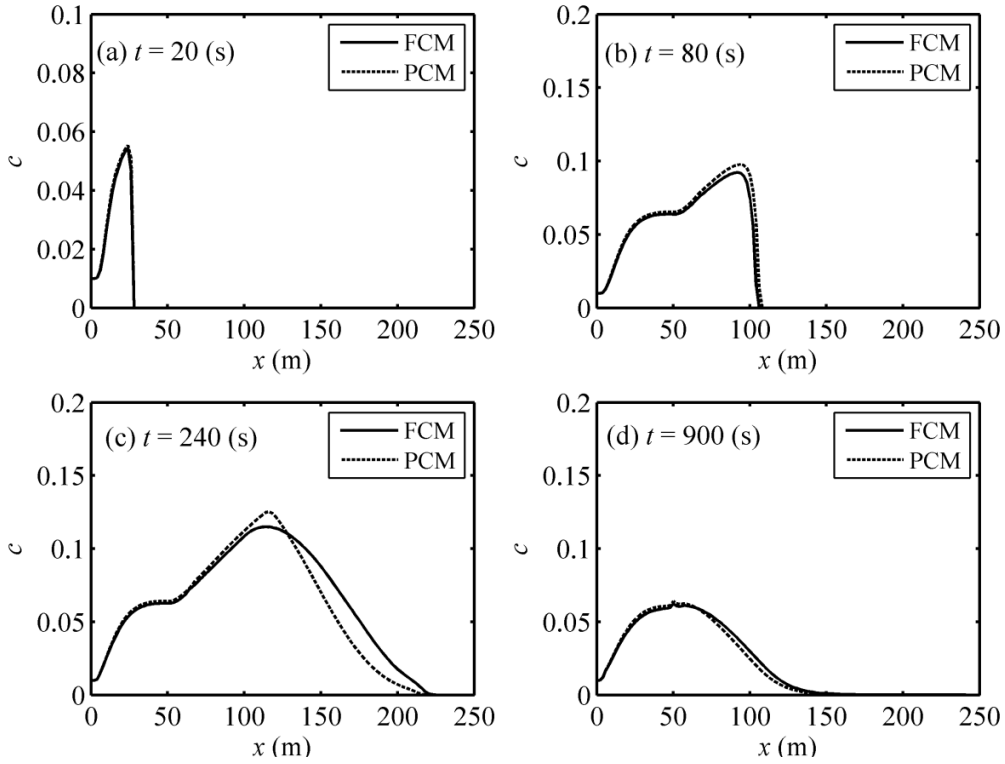

Figure 5. 8 Comparison of the longitudinal profiles of sediment concentration at y = 0 m at different time between FCM and PCM.

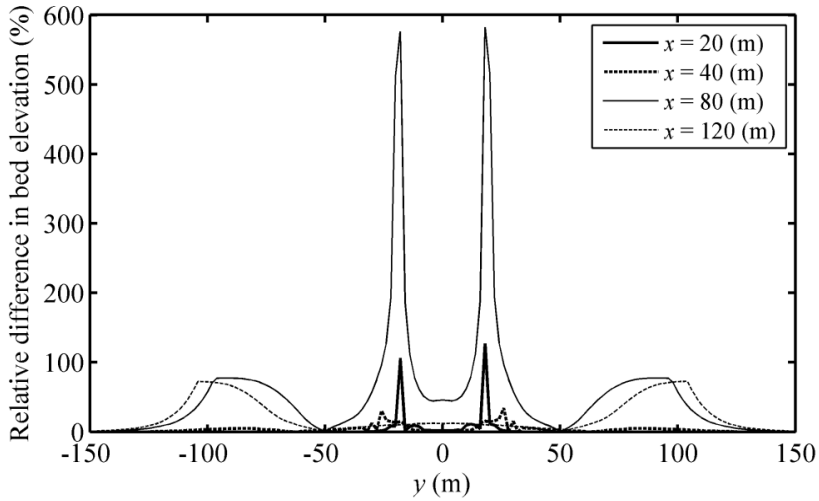

Figure 5. 9 Relative difference of the final bed elevation between FCM and PCM.

5.1.3 Discussion

There exist some discrepancies between numerical solutions of the fully coupled model and that of Bradford and Katopodes (1999b). For example, the area with considerable bed deformation (Figs. 5.3 and 5.4) is much wider than that from Bradford and Katopodes (1999b), i.e., $|y| < 30$ m in Figure 5.5(d) vs. $|y| < 5$ m in Bradford and Katopodes (1999b). Physically, with the lateral spreading of turbidity currents, it is reasonable to see appreciable morphological change in a wide region as in Figs. 5.3 and 5.4. The discrepancies may be ascribed to the inappropriate treatment of the downstream boundary conditions by Bradford and Katopodes (1999b), as explained below. The current at x = 100 m, which is defined as the outlet boundary by Bradford and Katopodes (1999b), tends to be subcritical (Ri > 1, see Figure 5.5). The subcritical regime at x = 100 m, if set to be the downstream outlet boundary as by Bradford and Katopodes (1999b), certainly necessitates the imposition of appropriate boundary conditions. This is nothing new, but similar to that in the routing of open channel flows (Cunge *et al*. 1980). Therefore, it is incorrect to specify a free flow at the boundary. While Bradford and Katopodes (1999b) have attempted to attribute their practice to the absence of a hydraulic jump, their arguments may not be fully justified. It is very likely to miss some key features (e.g., internal hydraulic jump) with a comparatively small domain (e.g., Kostic and Parker 2006, 2007). Equally importantly, the fine sediment (d = 0.09 mm) should favour the occurrence of an "internal hydraulic jump". In the critique here, it is important not to confuse the differences due to the inappropriate treatment of boundary conditions by Bradford and Katopodes (1999b) with the feedback impacts of bed deformation.

5.2 Turbidity currents and submarine channel-levee morphology

In the previous section, a horizontal fan type of channel-levee morphology was considered. Yet it should be noted that submarine fans are not necessarily horizontal. In this section, the incipient formation of submarine channel-levee morphology is investigated numerically in a systematic way. A partially coupled model was used by Imran *et al*. (1998) in a previous numerical investigation of the incipient formation of the submarine channel-levee morphology. Furthermore, Imran *et al*. (1998) only examined the effects of a limited range

of bed slope and sediment particle size. Three key effects are examined in the present thesis including the upstream boundary condition, the sediment particle size and the bed slope of the fan. The present study covers a larger range of bed slope, sediment particle size, which should be more typical of the real submarine turbidity current processes. More importantly, a fully coupled model is used here.

The sketch of the computational domain is similar to that in Figure 5.10. It is similar to that in the prior section, yet no abrupt slope break is involved in Figure 5.10. The initial bed is assumed to be non-erodible, meaning that only sediment deposited previously can be re-entrained. This assumption is reasonable over submarine fans and it does not conflict with the above erodible bed case in **Section 5.1** because only a very short reach of horizontal basin is considered there. Moreover, sediment deposition dominates in the considered portion of submarine fan. The following parameters are specified following Imran *et al*. (1998): b = 50 m, p = 0.5, c_D = 0.005, d = 60 μm, ρ_s = 2650 kg/m^3, initial bed slopes S_{bx} = 0.001 and S_{by} = 0.0. Based on grid-convergence tests, the spatial steps Δx = 25 m, Δy = 12.5 m, and the Courant number Cr = 0.95 are used. The smaller spatial step Δy in the y-direction is due to the limited width of the inlet boundary (b = 50 m), and also that at least four nodes are required to compute a numerical flux in the SLIC scheme (see Chapter 2). The upstream boundary conditions are h_0 = 4.0 m, u_0 = 2.5 m/s, v_0 = 0.0 m/s and c_0 = 0.02. Turbidity currents are computationally simulated for a period of 5 hours.

The above parameters and upstream boundary conditions provide a reference case, labelled as Case 1 in Table 5.1. Cases 2 and 3 illustrate the impacts of upstream boundary condition with inlet sediment concentrations of 0.05 and 0.08 respectively. Cases 4 and 5 show the influence of bed slope and Cases 6 through 9 represent the impacts of sediment particle size. The coordinates are non-dimensionalized by the inlet width. For convenience of description, the dimension of the channel-levee morphology due to turbidity currents is defined as the product of the channel width and length.

Table 5. 1 Numerical Cases for turbidity currents over submarine fans

Case No.	S_{bx}	d (μm)	Ri_0 (c_0)	Remarks
1	0.001	60	0.21 (0.02)	*Reference case*
2	0.001	60	***0.53 (0.05)***	*Impact of upstream boundary conditions*
3	0.001	60	***0.83 (0.08)***	
4	***0.01***	60	0.21 (0.02)	*Impact of initial bed slope*
5	***0.05***	60	0.21 (0.02)	
6	0.001	***20***	0.21 (0.02)	*Impact of sediment particle size*
7	0.001	***100***	0.21 (0.02)	
8	0.001	***300***	0.21 (0.02)	
9	0.001	***1000***	0.21 (0.02)	

Figure 5. 10 A sketch of the square computational domain of the submarine fan.

5.2.1 Formation processes of channel-levee morphology

Figure 5.11 shows the numerical solutions of Case 1 at t = 5 hours from the fully coupled model, including (a) non-dimensional current thickness h/h_0 , (b) non-dimensional sediment concentration c/c_0, (c) non-dimensional bed deposition depth $\Delta z/h_0$, and (d) non-dimensional current velocity distribution U/u_0. The legend 0.5 in Figure 5.11(d) indicates a magnitude for current velocity of 1.25 m/s (0.5×2.5 m/s). The downstream propagation and lateral spreading of turbidity currents are simulated. As the current propagates downstream and spreads laterally (Figure 5.11a), the current velocity decreases

with the distance away from the inlet (Figure 5.11d). This is because the turbidity current is depositional, as evidenced by the longitudinally and laterally decreasing sediment concentration (Figure 5.11b) and also the deposition (Figure 5.11c). Two long and narrow depositional regions are formed along the x -direction in the two sides of the inlet boundary, which finally become attached at a distance of about 40 times the inlet width downstream (Figure 5.11c). A channel can be observed, which are essentially bounded by two long levees. The incipient formation process of submarine channel-levee morphology by turbidity currents is resolved. The formed channel-levee morphology is bounded by deposition at the downstream side (Figure 5.11c), which is essentially the distal lobe on submarine fans.

Of particular interest is the transverse levee shape (e.g., Skene *et al.* 2002; Skene and Piper 2006; Birman *et al*. 2009; Kane *et al.* 2010). Figure 5.12 shows the non-dimensional transverse deposition thickness $\Delta z / h_0$ from eight cross sections at t = 5 hours, which essentially characterises the transverse levee shape. From Figure 5.12, the transverse levee shape varies considerably in the downstream direction. Specifically, the lateral decay rate of the levee height from the levee crest becomes slow with the distance away from the inlet boundary. It is clear from the partial derivative of the levee height, as shown in Figure 5.13. The downstream variation in the levee shape missed in Birman *et al*. (2009) is clearly resolved by the fully coupled model. An increase in the water entrainment can be expected in the downstream direction corresponding to the decreasing Richardson number (Figure 5.14). Thus it is not surprising to suggest a relation of the levee shape with the water entrainment.

For the computed bed deposition distribution as shown in Figure 5.11(c), there seems to be some 'undulations' in the vicinity of the inlet boundary ($x/b = 0$, $y/b = 0$), which however are not true undulations. It can be seen from Figure 5.12(a), showing the detailed transverse deposition thickness in the vicinity of the inlet boundary shown, that these 'undulations' are actually a reflection of the rapid increase of the channel width within the short distance $x/b < 2.5$.

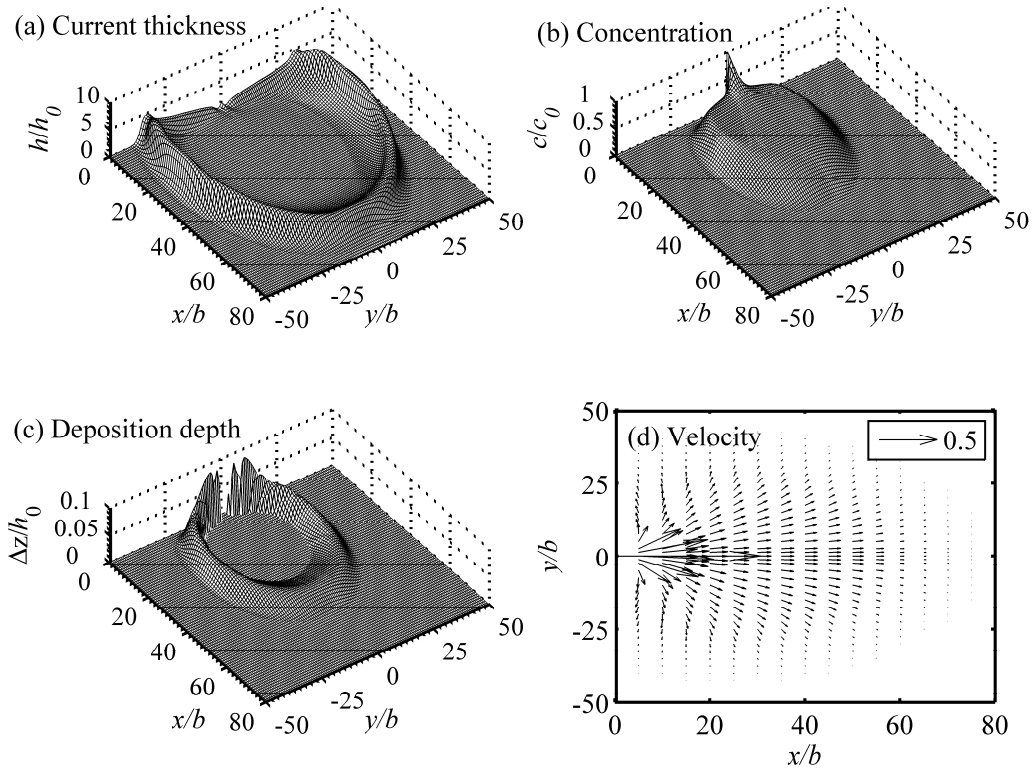

Figure 5. 11 Non-dimensional numerical solutions at t = 5 hrs for Case 1: (a) current thickness, (b) sediment concentration, (c) deposition depth, and (d) current velocity.

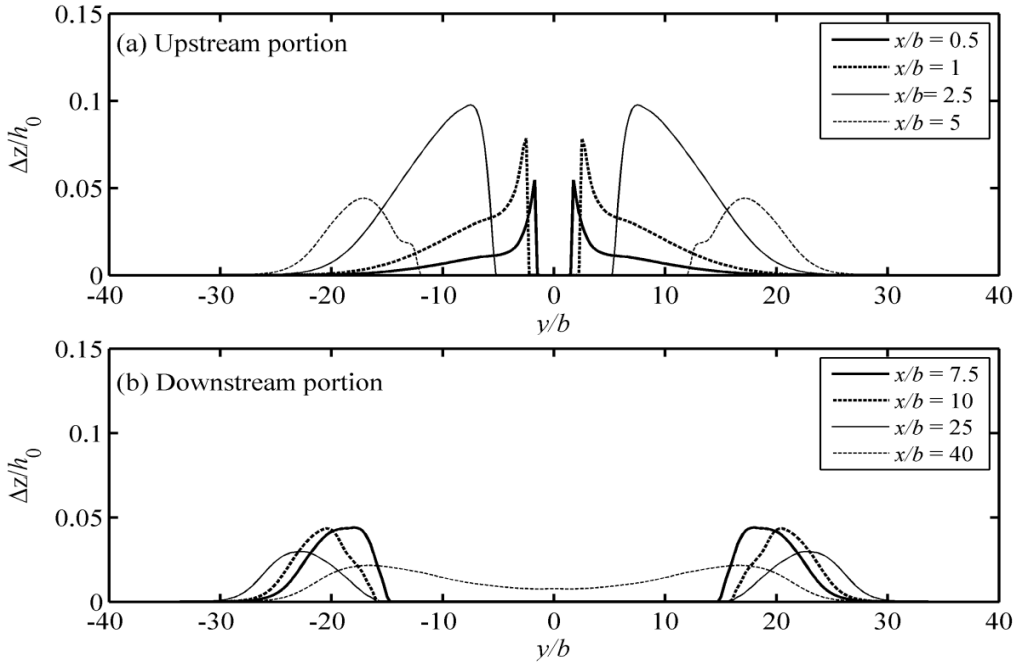

Figure 5. 12 Non-dimensional transverse deposition depth at *t* = 5 hours for Case 1.

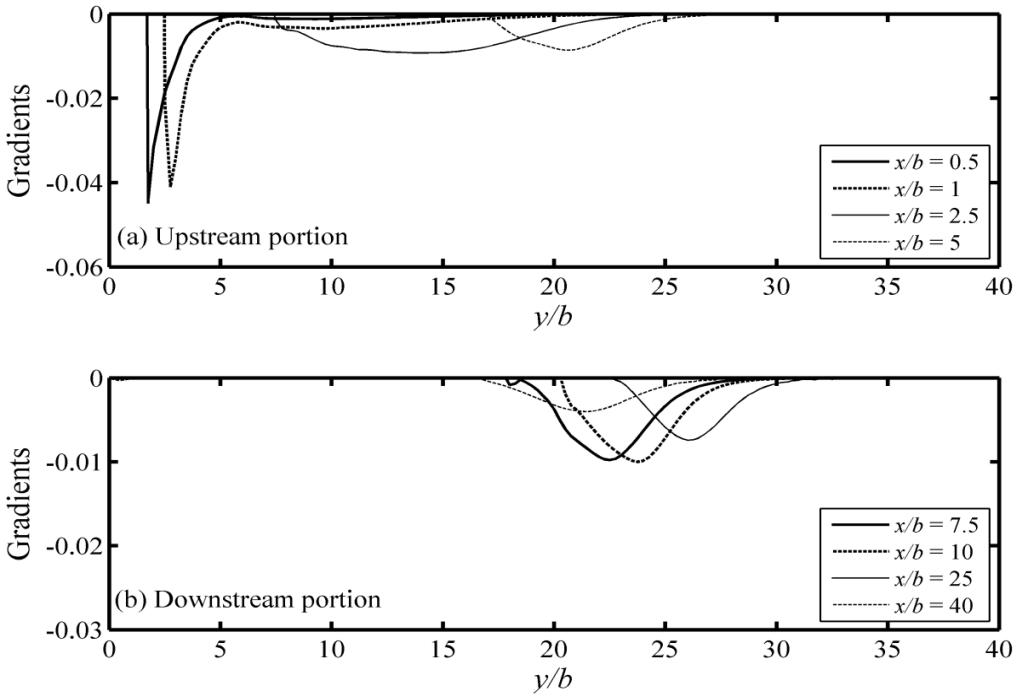

Figure 5. 13 Lateral gradients of the non-dimensional deposition thickness on the non-dimensional distance $b/h_0\partial(\Delta z)/\partial y$ at *t* = 5 hours for Case 1.

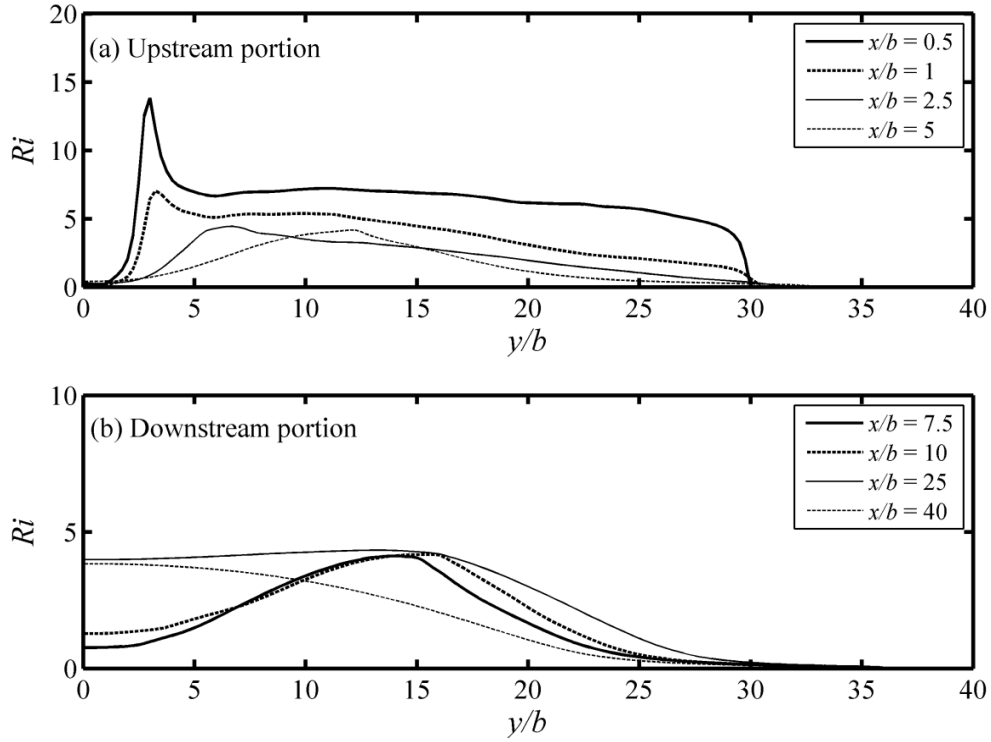

Figure 5. 14 Lateral variations of the bulk Richardson number from different cross sections at *t* = 5 hours for Case 1.

5.2.2 Impact of upstream boundary conditions

The upstream boundary condition is a key factor in mathematical modelling of river morphodynamics (Fasolato *et al*. 2009). For turbidity currents, it can be represented by the bulk Richardson number involving current thickness, velocity and sediment concentration. The impact of the inlet sediment concentration certainly warrants such an investigation.

Figure 5.15 illustrates the comparison of the transverse channel-levee morphology (i.e., levee height along the y -direction) by turbidity currents with different inlet sediment concentrations (Cases 1, 2 and 3). The channel-levee morphology exhibits remarkable differences for these cases. An increase in sediment input (i.e., sediment concentration) induces increases in both the levee height and the channel width. The termination of the channel around x/b = 40 by deposition for Case 1 (Figure 5.12b) does not occur for Cases 2 and 3 with enlarged sediment inputs (Figure 5.15d). These observations are quite understandable because the driving forces of turbidity currents come from the density excess between the turbidity current and the ambient fluid, as represented by $g'h\partial z/\partial x$ in the x -direction [note: $g'=Rgc$]. With a relatively larger driving force due to a higher inlet sediment concentration (Cases 2 and 3), sediment can be transported downstream for a relatively large distance. Furthermore, an increase in sediment input provides more sediment to build up the levee. This facilitates a wider, longer and deeper channel. Apparently, a larger Richardson number (due to a higher sediment concentration) favours shaping submarine channel-levee morphology. To the authors' knowledge, this seems to be the first attempt to examine quantitatively how upstream boundary condition in terms of the sediment input rate affects the formation of the submarine channel-levee morphology.

Note that turbidity currents that feature sediment concentration as high as 0.25 (Hallworth and Huppert 1998) may behave qualitatively differently from the present cases with maximum concentration of 0.08. Hyperconcentrated turbidity currents may exhibit a non-Newtonian property (Hallworth and Huppert 1998; See also in Section 3.4), giving rise to an additional friction. The additional friction may balance out or even overwhelm the enlarged driving force due to the increased sediment input. A smaller Richardson number (due to lower concentration) may favour channel-levee morphology for hyperconcentrated

turbidity current. However, the mechanism for hyperconcentrated turbidity current remains far from clear and these over submarine fans are not the focus of the present study.

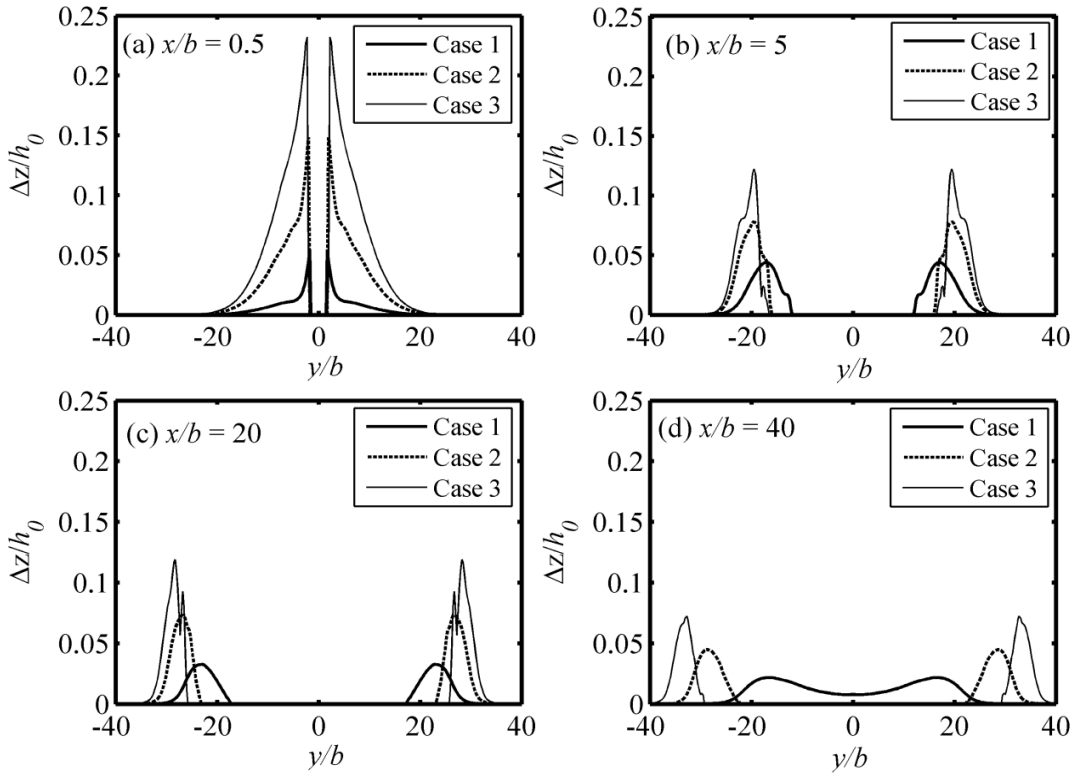

Figure 5. 15 Comparison of transverse non-dimensional levee height at cross sections from Cases 1, 2 and 3, showing the impacts of inlet Richardson number.

5.2.3 Impact of initial bed slope

Since the terms $g'h\partial z/\partial x$ and $g'h\partial z/\partial y$ represent the gravitational driving forces for turbidity currents, a variation in the bed slope will greatly affect the evolution of turbidity currents and the resultant morphological features once the sediment concentration (i.e. the density excess) is prescribed. Not surprisingly, sedimentologists and geologists have suggested connections between the levee shapes and the bed slopes (e.g., Skene *et al.* 2002; Skene and Piper 2006; Kane *et al.* 2010). It is useful to see how and in what way the bed slope influences the formation of channel levee morphology.

Figure 5.16 presents the comparison of the transverse channel-levee morphology from Cases 1, 4 and 5 with turbidity currents over different bed slopes. Apparent differences are noted in the transverse levee morphology, in terms of channel depth (i.e., levee height), channel length and channel width. First, turbidity currents over a relatively large bed slope tend to produce shallower channels than those over a relatively small bed slope. Second, for channels over a large slope, the channel is narrower near the inlet boundary ($x/b = 5$, Figure 5.16b) and appears wider further downstream, compared to channels over a small bed slope ($x/b = 20$, Figure 5.16c). Third, channels on a mild slope tend to be bounded on the downstream side by deposition (Case 1, Figure 5.16d), whereas channels on a large slope can only be observed within a short distance from the inlet boundary (Case 5). For Case 4 with intermediate bed slope ($S_{bx} = 0.01$), the channel extends downstream to a distance of about 40 times of the inlet width. Essentially, it is Case 4 with an intermediate bed slope that generates channel-levee morphology of the largest scale (channel length: longest; channel width: similar to Case 1, wider than Case 5). Submarine fans with appropriate bed slope favour the formation of submarine channel-levee morphology.

Note that the impact of bed slope shares little common ground with that of inlet sediment concentration, though varying either of them would incur the same trend of variation in the driving force. It is because a change in sediment input not only affects the driving force, but also determines the amount of sediment available to build up the levee.

5.2.4 Impact of sediment particle size

Another important factor is bed texture (specifically, the particle size). Figure 5.17 shows the transverse channel-levee morphology (non-dimensional levee height along the *y*-direction) for Cases 6~9. Similar to the impacts of upstream boundary condition (Figure 5.15) and bed slope (Figure 5.16), varying the particle size induces remarkable differences in the resultant channel-levee morphology (Figure 5.12 and Figure 5.17). First, the channel width and the channel depth (i.e., levee height) vary monotonically with the particle size. Turbidity currents carrying coarser sediment produce a deeper and narrower channel; and vice versa. Turbidity currents with coarse sediments are more likely to be depositional and thus do not spread laterally very much. Therefore, two high lateral deposition regions are

formed close to the centre line of the considered fan, corresponding to the observed narrow and deep channel by turbidity currents with coarse sediments. Second, the longest channel is formed by turbidity currents with intermediate particle size: channel length = 40 times of the inlet width for Case 1 with d = 60 µm (Figure 5.11c, Figure 5.12). Yet the channel lengths by turbidity currents with the finest (Case 6 with d = 20 µm, Fig 5.17a) and coarsest (Case 9 with d = 1000 µm, Figure 5.17d) sediments are only 2.5 and 4 times the inlet width, respectively. If sediments are too fine, they can be transported farther downstream without sufficient deposition. In contrast, coarser sediment would deposit near the inlet boundary without being transported a sufficient distance to create a channel. Turbidity current with intermediate particle size favours the formation of channel-levee morphology with a large scale. While heterogeneous sediment may be more typical, uniform sediment is assumed. Heterogeneous sediment transport by turbidity current is reserved for future studies.

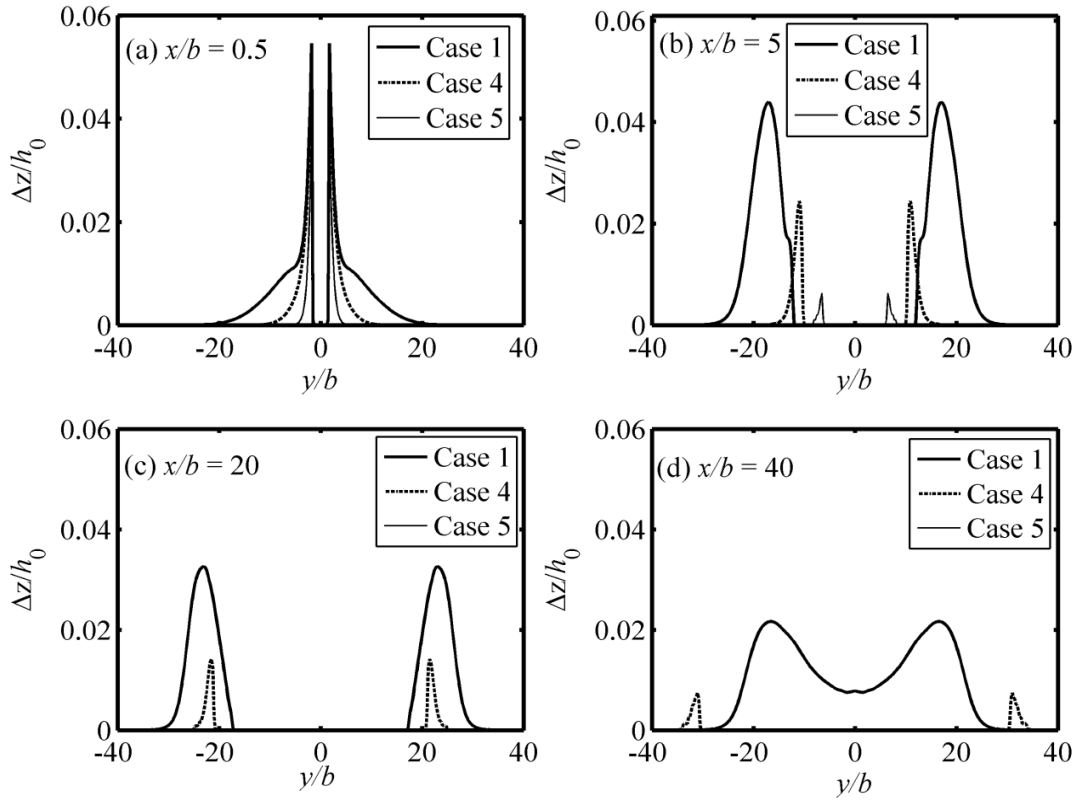

Figure 5. 16 Comparison of transverse non-dimensional levee height at different cross sections from Cases 1, 4 and 5, showing the impacts of initial bed slope.

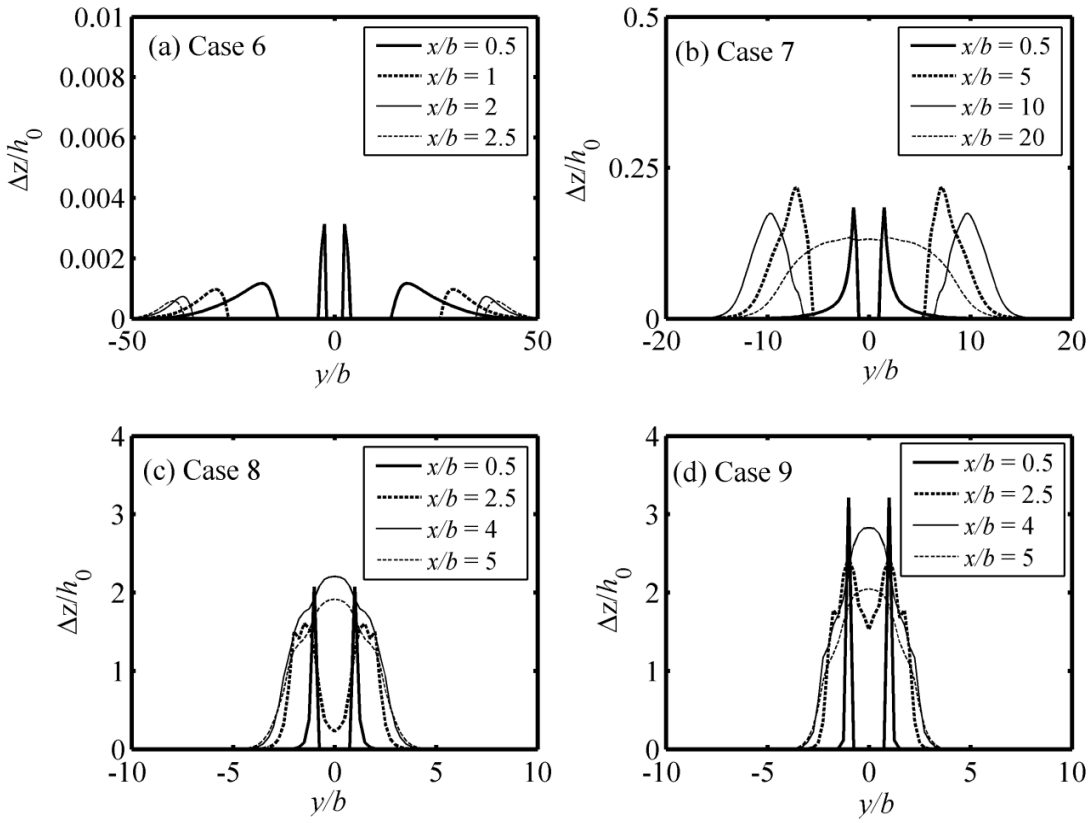

Figure 5. 17 Transverse non-dimensional levee height at cross sections from (a) Case 6, (b) Case 7, (c) Case 8 and (d) Case 9, showing the impacts of sediment particle size.

5.2.5 Feedback impacts of bed deformation

Characterised by intermediate particle size and large inlet Richardson number, Cases 1 and 3 are deployed to examine the feedback impact of bed deformation. Figure 5.18 shows the non-dimensional difference in bed elevation at t = 5 hrs between the PCM and the FCM for (a) Case 1 and (b) Case 3. Negative values indicate that bed elevation by the FCM is lower than that by the PCM. For Case 1, the maximum difference is below 0.002 (Figure 5.18a) and negligible compared to the corresponding levee height (0.02-0.1, see Figure 5.12). This implies that the feedback impacts of bed deformation for Case 1 are negligible. This is because Case 1 is characterised by mild bed aggradation (maximum non-dimensional deposition depth: about 0.1, Figure 5.12). In contrast, the feedback impacts of bed deformation are considerable for Case 3 featuring substantial bed aggradation (Figure 5.15), as implied by the considerable difference in bed morphology (Figure 5.18b). The difference

attains about 0.04 around $x/b = 20$, which is comparable to the corresponding levee height (about 0.1, see Figure 5.15c). While PCM is approximately applicable for turbidity current with mild bed deformation (say, Case 1), fully coupled modelling is critical for turbidity currents featuring rapid bed deformation (say, Case 3). For refined quality of turbidity current modelling, fully coupled modelling is generally suggested as it incurs negligible increase of computational cost as compared to partially coupled modelling.

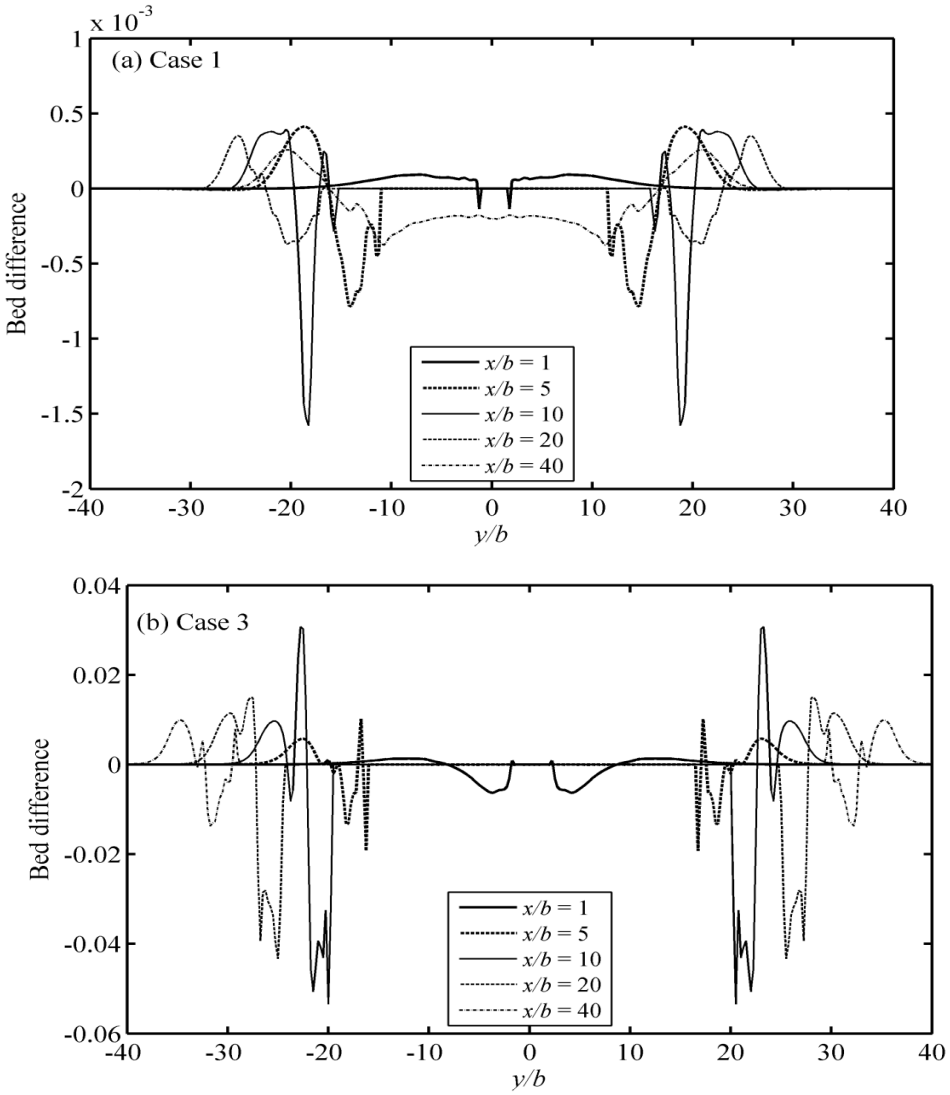

Figure 5. 18 Non-dimensional difference in bed elevation at $t = 5$ hrs between the fully and partially coupled models for (a) Case 1 and (b) Case 3.

5.3 Conclusion

In this chapter, the fully coupled model has been applied to investigate turbidity currents near a submarine canyon-fan transition and over submarine fans. Comparisons of the fully coupled and partially coupled models demonstrate that the feedback impacts of bed deformation are considerable and deserve full consideration. Therefore physically coupled modelling is essential to achieve refined resolution of turbidity currents featuring active sediment transport. Computational case studies show that bed slope, sediment particle size and upstream boundary condition are the key factors dictating submarine channel-levee morphology. Appropriate bed slope and sediment particle size may favour the formation of submarine channel-levee morphology, as does a larger Richardson number. The present findings are qualitatively correct. Quantitative uncertainty is inevitable as empirical parameters and relationships are involved, as is the single-sized description of sediment transport. The values of the empirical parameters in the present study are based on previous numerical case studies.

Chapter 6. MODELLING OF TURBIDITY CURRENTS AND RESERVOIR SEDIMENT MANAGEMENT

Summary

- Turbidity currents in a real reservoir characterized by severe sedimentation are numerically simulated
- Current front location and transport rates compare favourably with measured data
- The present work provides a useful tool for effective reservoir sediment management using turbidity currents

This chapter presents a computational study of turbidity currents in the Xiaolangdi reservoir of the Yellow River. The Xiaolangdi reservoir controls 92.3% of the total basin area of the Yellow River and almost 100% of the sediment load. Severe sedimentation has occurred in the Xiaolangdi reservoir since its completion in 2001. Field scale water sediment regulation experiments have been undertaken to generate and make use of turbidity currents to flush sediment and accordingly reduce sedimentation (e.g., Li 2004; Li *et al*. 2006; Qu *et al*. 2006; Xu *et al*. 2007; YRCC 2007). Consequently, a large volume of hydrological data on turbidity currents has been obtained. Despite their large volume, the data are insufficient for a comprehensive and systematic understanding of turbidity current propagation in the reservoir, because they are event-specific and not complete for each event. Furthermore, most of the post-experimental analyses are based on simple empirical relations developed using limited information (e.g., Li 2004; Li *et al*. 2006; Qu *et al*. 2006; Xu *et al*. 2007; YRCC 2007). Nevertheless, if these hydrologic data can be reproduced numerically by a physically-based model, it should be possible to determine information that is not measured

and thus provide support for design of future experiments, and the development of appropriate sediment management measures.

Two events of turbidity currents were observed in the Xiaolangdi reservoir during the water-sediment regulation experiment between the 19th June and the 13th July 2004 (Li 2004; YRCC 2007), just before the flood season. The experiment aimed to make full use of the extra water storage (stored above the flood control water level) to reduce sedimentation. Two phases are involved. In the first phase (19th - 29th June), water level in the Xiaolangdi reservoir was lowered by releasing clear water. In the second phase (2nd - 13th July), two sediment-laden flood processes were formed in the Xiaolangdi reservoir due to water releasing from the Sanmenxia and Wanjiazhai reservoirs respectively, which plunged and formed the two turbidity current events. The first event is investigated systematically with a series of numerical cases, through which model parameters are calibrated. Then the calibrated model is applied to the second event.

Figure 6. 1 Flushing of sediment by turbidity current in the Xiaolangdi reservoir.

Before proceeding, it is important to point out that earlier efforts using an imbalanced model (based on DGM version of the SLIC scheme, see Chapter 2 for details) have been made to resolve numerically the turbidity currents in the Xiaolangdi reservoir, which unfortunately failed due to physically unrealistic results: oscillations in current velocity

close to the river bank being produced, and the computations collapsed before completion). Numerical results presented in this chapter are obtained from the well-balanced fully coupled model (based on the WSDGM version of the SLIC scheme, see Chapter 2 for details).

6.1 Modelling the First Event of Turbidity Currents

6.1.1 Data preparation and summary of numerical cases

The first event occurred from about 18:00 5th July to 19:00 6th July when the flow discharge at Sanmenxia was about 2000 m^3/s. By scouring the depositional delta of the Xiaolangdi reservoir, a sediment-laden flood was formed and plunged around the cross section HH35 (about 58.5 km upstream of the Xiaolangdi dam). Note that there are 56 control cross sections in the 130 km long reach between the Sanmenxia and Xiaolangdi dams, termed as HH56-HH01 in a descending order from the Sanmenxia dam to the Xiaolangdi dam. The turbidity currents from this event dissipated around HH05 (Li 2004; YRCC 2007). Measurements were made at positions with different distances from the river bank at HH32, HH29, HH17, HH13 and HH09. Thus the time-series of the measurements presented below are position-specific at each cross section. At each position, vertical profiles of velocity and sediment concentration were measured. The upper current surface position is determined with a threshold sediment concentration of 0.002 (about 5.0 kg/m^3 if ρ_s = 2650 kg/m^3), and the current thickness is obtained by subtracting the bed elevation from the upper current surface elevation (YRCC 2007). Then the current velocity and the sediment concentration are averaged over the current thickness. Figure 6.2 shows the measured current thickness and the layer-averaged current velocity and sediment concentration in the measurement. The time t = 0 hr corresponds to 20:24 5th July when the current arrived at HH32. Although there are only three data points at HH32 (Figure 6.2), they provide a good representation of the process of this event (YRCC 2007). Thus HH32 is considered as the upstream boundary in the computation. Current variables at the upstream boundary are linearly interpolated from the measurements with two assumptions. First, the current surface elevation is assumed to be the same across the cross section. Second, the current velocity and the sediment concentration are scaled to the current

thickness. No downstream boundary conditions are needed because the current did not reach the dam (Li 2004; YRCC 2007). Yet, in the computation, the current front may arrive at the downstream boundary if the parameters in Table 6.1 are not specified sensibly. In this case, the simulation will be ended automatically in the computation. Furthermore, the assumptions made in the implementation of the upstream boundary conditions will be examined later.

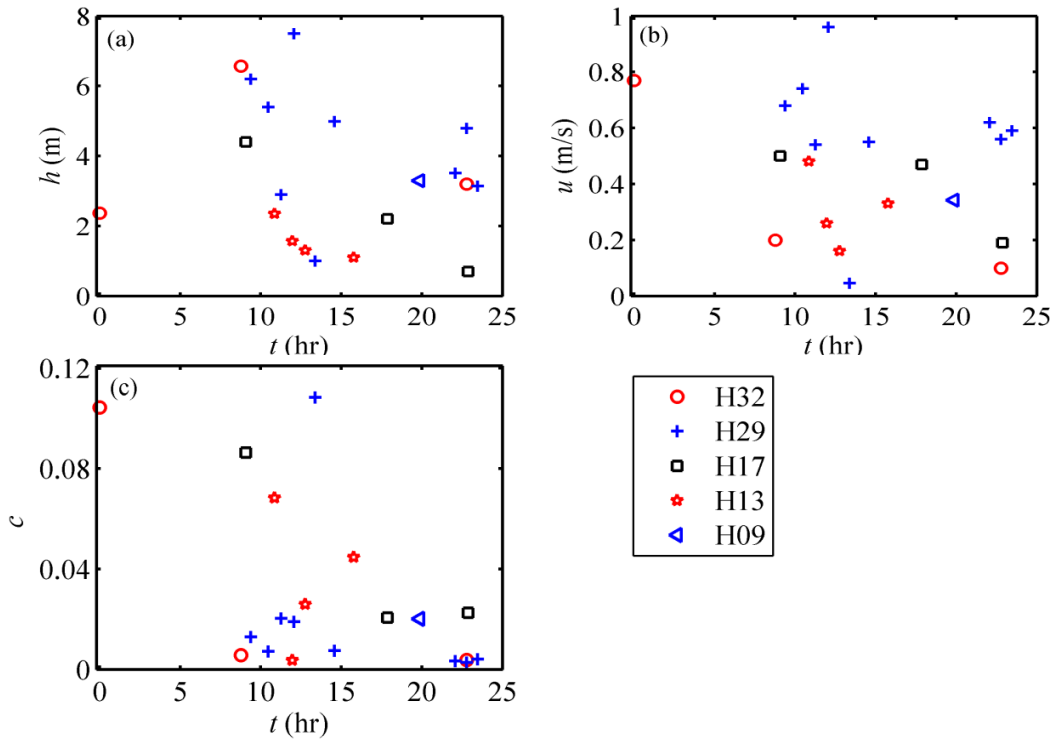

Figure 6. 2 Observations of the first event. Time t = 0 hr corresponds to 20:24 on 5 July 2004.

The initial bed topography is linearly interpolated from the 32 cross sectional profiles (HH32-HH01) surveyed in May 2004, as shown in Figure 6.3 in a contour format. Also included in Figure 6.3 are the details of the five cross sections (HH29, HH25, HH17, HH13 and HH09). Four positions (P1, P2, P3 and P4: from top to bottom) across each cross section are highlighted, at which numerical solutions are presented later. There are no turbidity currents initially on the river bed. The following parameters are specified with reference to the background of the Xiaolangdi reservoir: p = 0.4, ρ_s = 2650 kg/m^3. Based on grid convergence tests $Cr = 0.9$ and a spatial step of 12 m are used.

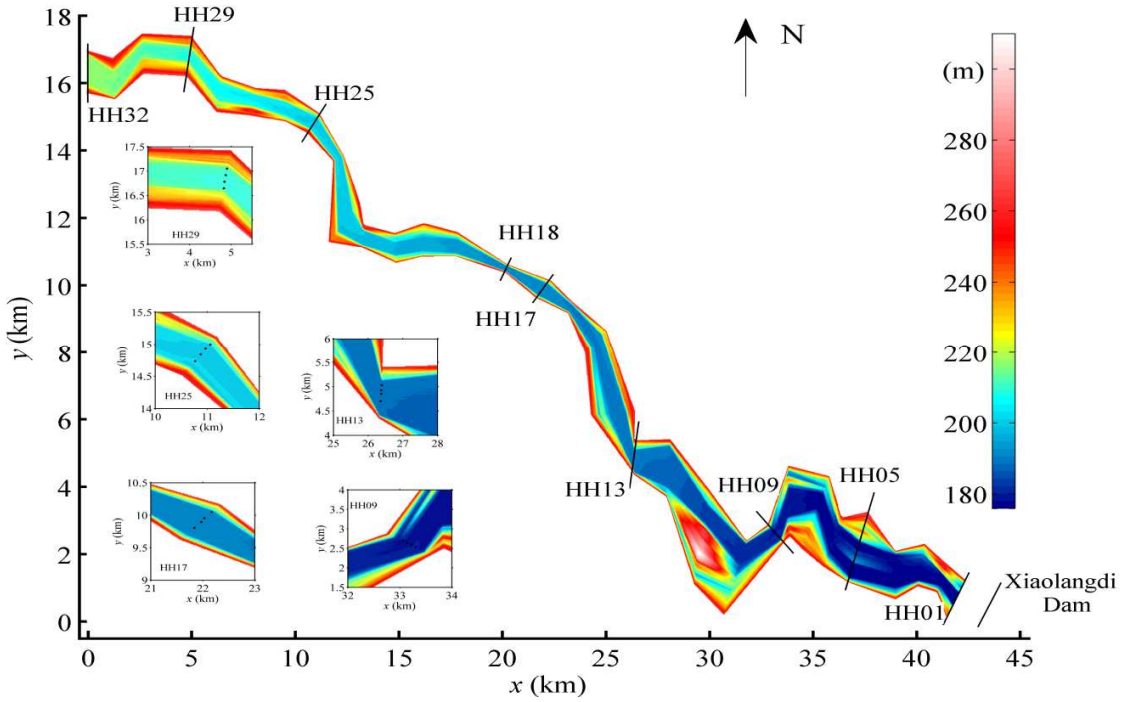

Figure 6. 3 Contour of initial bed topography based on the survey in May 2004.

As presented in Table 6.1, the range of c_D is based on the suggestion that lower values of the potential range [0.002-0.05] are suitable for large scale turbidity current (Bradford and Katopodes 1999a). The correction coefficient $\psi_p \leq 1$ follows Fildani *et al*. (2006). The large values of ψ_z is based on the observation by Han and Xiang (1981) that sediment concentration of turbidity currents can attain as high as about 34.5 times that computed by capacity formulae of open channel flow. The sediment diameter $d = 20$ μm for Runs ZF1-ZF5 and Runs PF1-PF3 is based on the median diameter measured at the upstream cross section HH32. In Run ZF6, a slightly finer $d = 15$ μm is used for comparison due to the potential of downstream sediment fining.

Table 6. 1 Numerical runs for the first turbidity current in the Xiaolangdi reservoir

Run no.	ZF1	ZF2	ZF3	ZF4	ZF5	ZF6	PF1	PF2	PF3
c_D	0.008	0.008	0.008	0.006	0.010	0.008	0.008	0.008	0.008
ψ_z or ψ_p	50	60	40	50	50	50	1.0	0.2	0.1
d (μm)	20	20	20	20	20	15	20	20	20

6.1.2 Advance of the turbidity currents

A well informed advance of the turbidity current may facilitate a timely operation of the bottom outlets and thus flushing of sediment through the reservoir (Fan and Morris 1992a, b; Toniolo *et al*. 2007). If the bottom outlets are closed upon the arrival of the turbidity current, ponded turbidity currents may lead to severe sedimentation (Toniolo *et al*. 2007), or, alternatively, if the bottom outlets are opened too early, stored water may be wasted. The current advance for the first event has been well documented (Li 2004; YRCC 2007) and provides a good data set to calibrate against the model. The comparison of the computed and measured current front location, measured through the distance along the *x*-direction is presented in Figure 6.4(a) for Runs ZF1-ZF6 and Figure 6.4(b) for Runs PF1-PF3. Also included in Figure 6.4(a, b) are the measured data at HH17, HH13, HH09 and HH05. A parameter R_t, defined as $R_t = (t_c - t_m)/t_m$, is introduced to measure the relative discrepancy between the computed and measured current arrival time at any cross section, where t_c and t_m are the computed and measured arrival times respectively. The estimated R_t is shown in Figure 6.4(c). R_t = 0 means the computed and measured current propagation speeds are identical. R_t < 0 means the model underestimates the current propagation, and vice versa. If the computed current does not reach a given cross section within 24 hrs, R_t has no value at such cross section, see Run ZF3, Run ZF5 and Run PF3. The following observations are made from Figure 4.

In the first few hours (about 3-5 hrs depending on the specific case) when turbidity currents are within the vicinity of the upstream boundary (x < 12 km), the speed of the current advance along the *x*-direction seems approximately constant. Afterwards, the current advance experiences an abrupt reduction in speed at around x = 12 km where there is a sharp bend (Figure 6.3). A similar abrupt reduction in speed is observed around x = 25 km. From Figure 6.4(a, b), the advance of the current front is considerably affected by the two parameters to be calibrated (c_D; ψ_z or ψ_p), as well as the sediment diameter d. Faster advance of the current front is generally observed for larger correction coefficients ψ_z or ψ_p, smaller bed drag coefficient c_D, as well as finer sediment. More rapid advance results from finer sediment being easier to entrain, which leads to higher sediment concentrations

and thus larger driving forces. A larger correction coefficient of the sediment entrainment formula also leads to a higher sediment concentration. Thus it is understandable to see faster current advance for larger correction coefficient (ψ_z or ψ_p) and finer sediment. The larger the bed resistance, as represented by c_D, the more energy the current expends during its propagation and thus the lower the propagation speed.

From Figure 6.4(c), the computed current propagation from Run ZF1 (the Zhang and Xie formula Eq. 2.19b, Figure 6.4a) and Run PF2 (the Parker formula Eq. 2.19a, Figure 6.4b) compare best with the observed data: the values of R_t for Run ZF1 and Run PF2 essentially vanish, whereas those from other cases either deviate significantly from zero or have no value at all at some cross sections. The difference between Run ZF1 and Run PF2 lies in that a deceleration phase is computed for Run ZF1 when the current front approaches HH05, whereas no signal of deceleration is seen for Run PF2 (Figure 6.4a, b). Around HH05, the river channel is aligned essentially with the *x*-direction (Figure 6.3), precluding the effects of bend-similar reach as occurred at around x = 12 km and x = 25 km. The location of the current front for Run ZF1 appears to be stable at around HH05, reflecting the observation that the first event did not reach the dam (Li 2004; YRCC 2007). In this connection, the ability of the model to capture the current front location appears satisfactory as the Zhang and Xie formula is used (Run ZF1, Figure 6.4a), whereas Run PF2 essentially fails to model the deceleration adequately (Figure 6.4b).

The failure of the Parker formula to capture the deceleration may result from the fact that it is derived from experimental turbidity current with coarse sand and gravel (Parker *et al*. 1987). Although the magnitudes of sediment entrainment using the Parker formula can be adjusted to be similar to those from the Zhang formula, the sensitivity of the former may not be well represented for fine sediment. Sediment entrainment estimated using the Parker formula would asymptotically approach a maximum if Z_m is sufficiently large ≥ 30: E_s would vary in a narrow band between $0.276\psi_p$ and $0.303\psi_p$. For the present field case, it is sensible to assume c_D = 0.008 and d = 20 μm. Accordingly, Z_m = 30 corresponds to a very small current velocity of about 0.1 m/s. This suggests that the estimated sediment entrainment by the Parker formula is almost independent of current intensity.

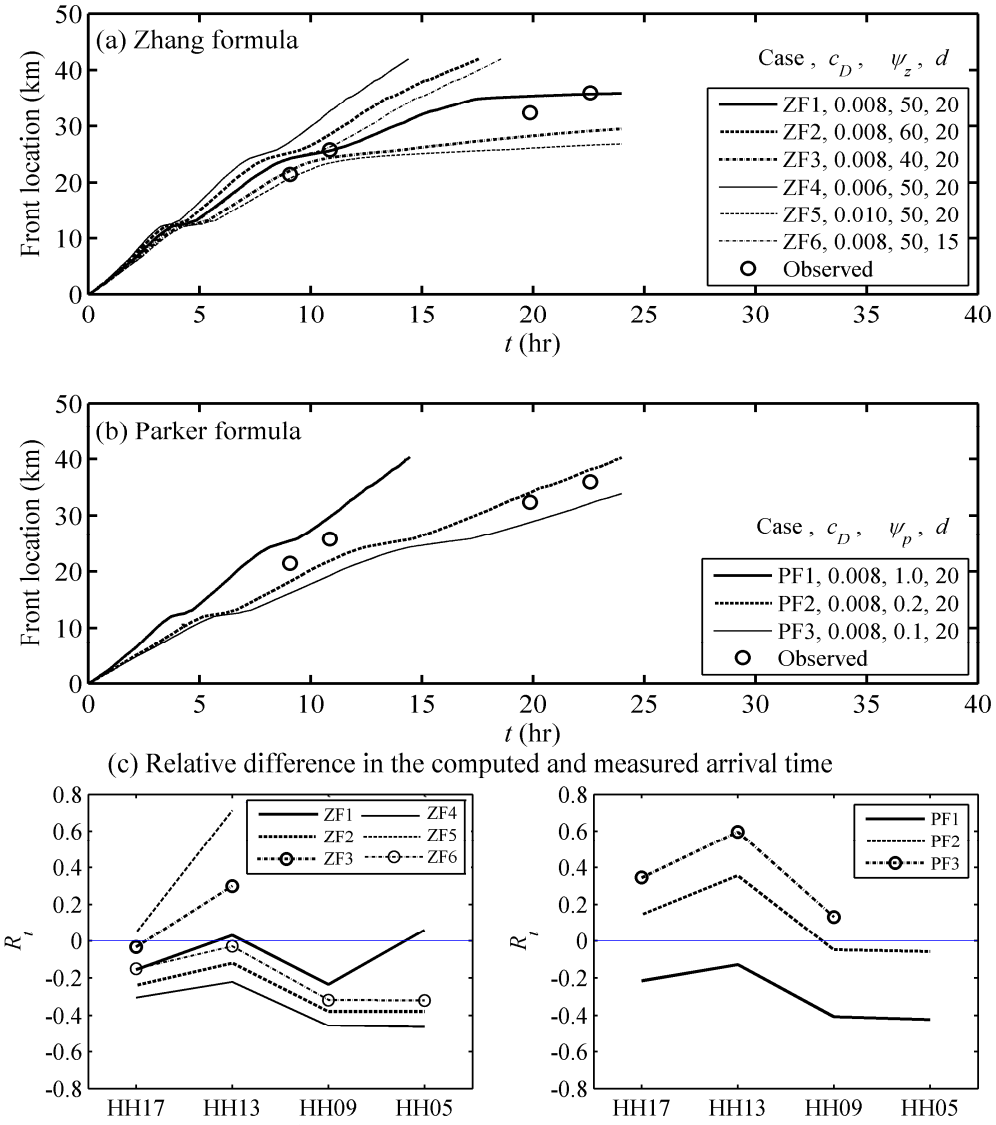

Figure 6. 4 Comparison of the computed and measured current propagation: current front location measured through the distance along the x-direction for (a) Runs with the Zhang formula, (b) Runs with the Parker formula; and (c) the relative time discrepancy between the computed and measured current arrival times.

6.1.2 Time series of the sediment transport rate

Figure 6.5 illustrates the computed (Run ZF1) and measured sediment transport rates ($=h\overline{Uc}$) at four cross sections: HH29, HH17, HH13 and HH09. As the measured values are position-specific, four positions (P1, P2, P3 and P4) at each cross section (see the black dots in the details of the five cross sections in Figure 6.3) that envelop all sampling positions are selected to present numerical solutions and thus provide a sensible comparison.

From Figure 6.5, the computed arrival of the current front at HH29 is much earlier than the time of the first measured value. This is because measurement did not start when the current front arrived at HH29 (YRCC 2007). The computed local transport rates always peak immediately upon the arrival of the current front, and then decrease with time. This trend can also be seen in the measured transport rates at HH17 and HH13 (Figure 6.5b, c), though somewhat obscure at HH29 (Figure 6.5a) and cannot be identified at HH09 (Figure 6.5d). A general downstream decreasing trend in the computed peak sediment transport rate is noted, reflecting the observation that the turbidity currents decelerate and finally dissipate at around HH05 (Li 2004; YRCC 2007). From above and Figure 6.5, the overall magnitude and the variation trend for the computed and measured sediment transport rates compare reasonably well for Case ZF1, though appreciable quantitative differences are seen (for example, the measured maximum sediment transport rates at HH29 and HH13 are missed). These differences are understandable as firstly the evaluation of model parameters is always difficult and approximate for field applications, and secondly the field data may also contain errors that make successful modelling difficult.

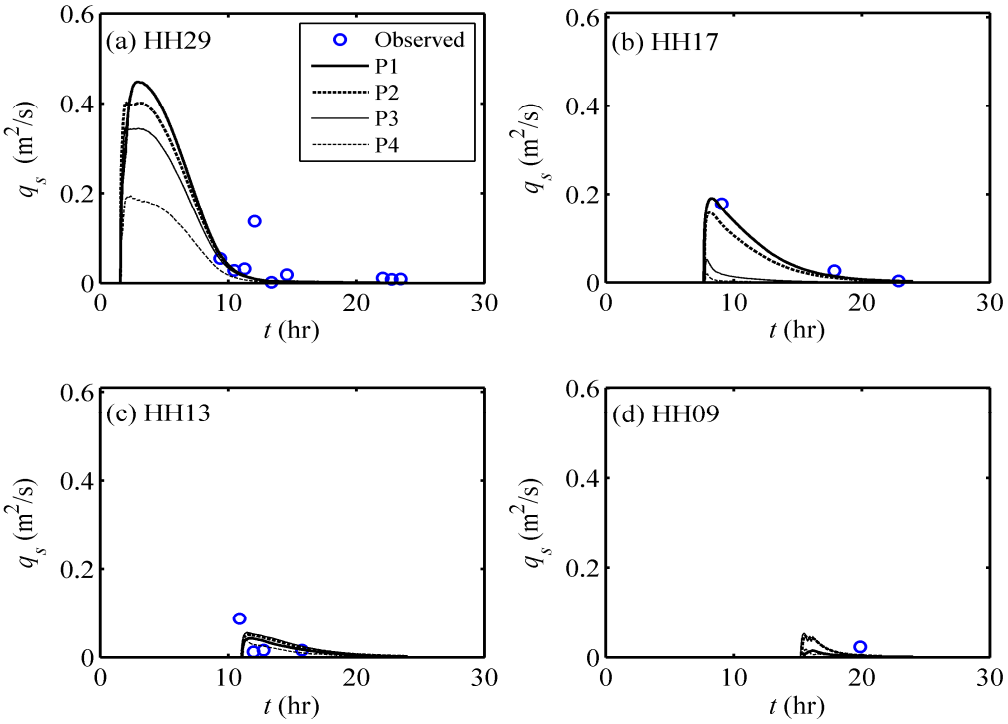

Figure 6. 5 Computed (Run ZF1) and observed time series of sediment transport rates at four cross sections.

In contrast to the comparison for Run ZF1 in Figure 6.5, the comparison of the sediment transport rates for Run PF2 is less convincing (Figure 6.6). Although the decreasing trend with time in the transport rate is predicted at HH29 (Figure 6.6a), it is missed for all other cross sections (Figure 6.6b, c, d). Furthermore, the downstream decreasing trend in the transport rates is also not captured (comparing Figure 6.6b, c, d).

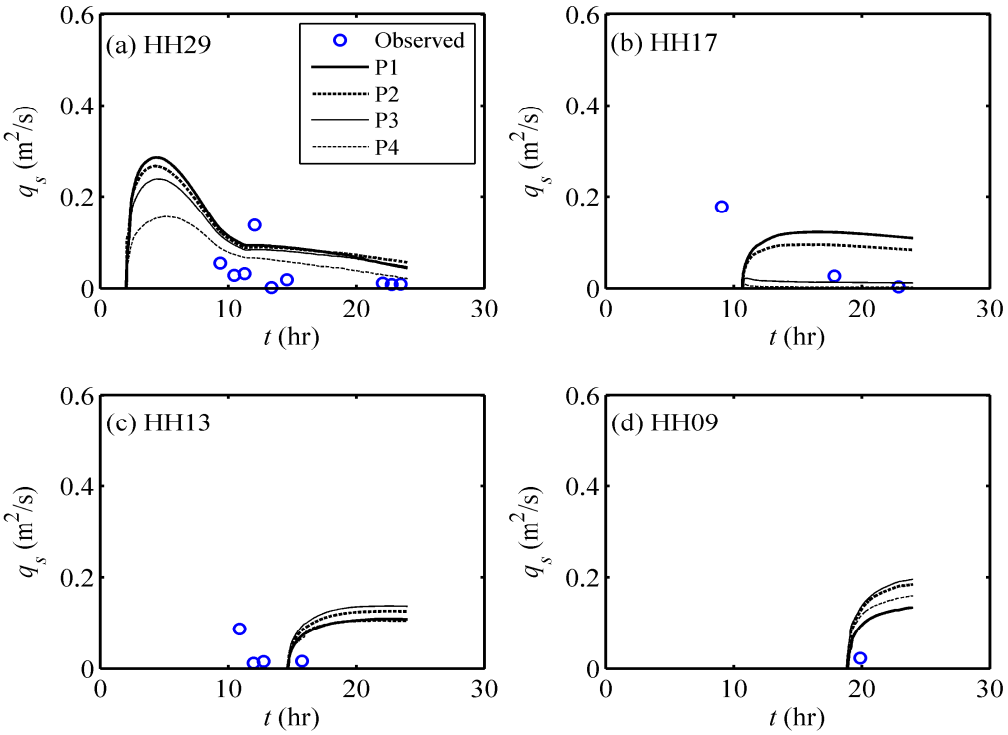

Figure 6. 6 Computed (Run PF2) and observed time series of sediment transport rates at four cross sections.

6.2.3 Time series of the current thickness

Comparisons of the computed and measured current thickness at the four cross sections are presented in Figure 6.7 for Run ZF1 and Figure 6.8 for Run PF2. In contrast to the contrasting performances in reproducing the sediment transport rate for the Zhang formula and the Parker formula respectively (Figs. 6.5 and 6.6), computations of the current thickness using both formulae compare unfavourably with the measurements, as seen in Figs. 6.7 and 6.8, where considerable differences exist between the computation and the measurements. This seems to suggest a poor performance of the present model to reproduce turbidity current thickness. However, it is premature to conclude so at present, because the

measured current thickness is actually derived from raw measured data of sediment concentration along the vertical, and inevitably suffers from much more uncertainty than other current variables such as the transport rate.

Unlike subaerial open channel flows, in which there is a clear water surface and the water depth can be measured directly, it is always impossible to directly measure the thickness of turbidity current, except in a few laboratory experiments using coloured turbid water. In the laboratory, the vertical profiles of current velocity can be measured in detail and the current thickness is usually computed from the following relation using the vertical integral of the velocity profile (Parker *et al*. 1987; Garcia and Parker 1993)

$$h = \left(\int_{z}^{z+H} u d\xi \right)^2 / \int_{z}^{z+H} u^2 d\xi \tag{6.1}$$

where H = total thickness of the turbidity current layer and the ambient fluid layer, ξ = vertical coordinate. In full 3D direct numerical simulations, there have also been other definitions of the current thickness using the vertical integral of the density profiles. These definitions, however, are not useful for the computation of the current thickness of turbidity current in the field, as the measured vertical information is usually very limited in the field especially for subaqueous turbidity currents in deep water (Xu *et al*. 2004).

In processing the field data on turbidity currents of the Xiaolangdi reservoir, threshold sediment concentration of 2.65 kg/m^3 or 5 kg/m^3 were used by YRCC (5 kg/m^3 for the 2004 measurement). Given this technique, a modest change of the threshold value (say, 1 kg/m^3 - 5 kg/m^3) would result in a substantial variation in the estimated current surface position and thus the current thickness, because the vertical concentration distribution is probably very smooth near the upper surface of the current (Kneller and Buckee 2000). The lack of detailed vertical data precludes an evaluation of its effects of this issue. Nevertheless, this speculation is supported by Dykstra and Kneller (2008), in which higher estimates of current thickness were obtained by assuming lower sediment concentrations.

Other factors also contribute to the uncertainty of the measured current thickness, such as the very long sampling time (as long as 1-2 hours, see YRCC 2008), as well as the use of

an intrusive hydrometric boat in measurements (Gonzalez-Castro and Muste 2007; Jamieson *et al.* 2011). Uncertainties related to the model parameters may also account for some discrepancy of the comparison, yet they are secondary as compared to those related the measured current thickness. Fortunately, these uncertainties can be minimized when sediment transport rate ($=h\overline{U}c$) are concerned (see Figure 6.5), as sediment concentration and current velocity around the threshold value would be comparatively very small and thus hardly affect the magnitude of sediment transport rate.

The above observations suggest that for the modelling of turbidity currents in the field, the current thickness may not be a proper variable to be targeted as an evaluation parameter in determining the performance of numerical models. Nevertheless, it does not follow that the current thickness computed by layer-averaged models is insufficiently accurate. Computed current thickness can be used as a guide for effective reservoir sediment management; for example, in determining the height of bottom outlets.

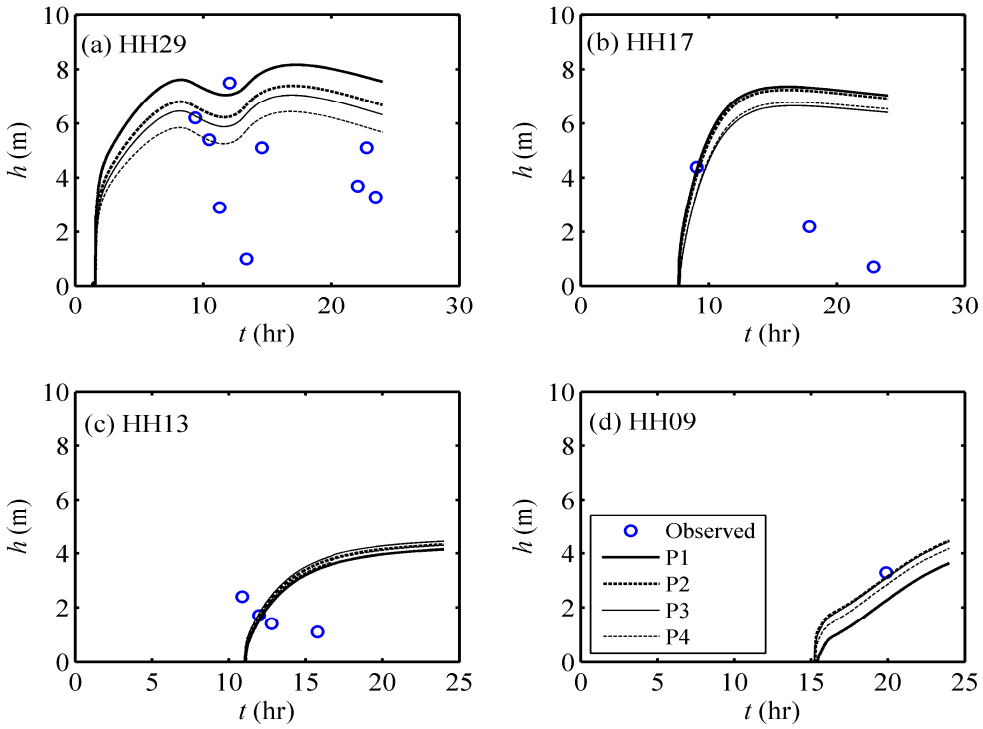

Figure 6. 7 Computed (ZF1) and observed time variation of current thickness at four cross sections.

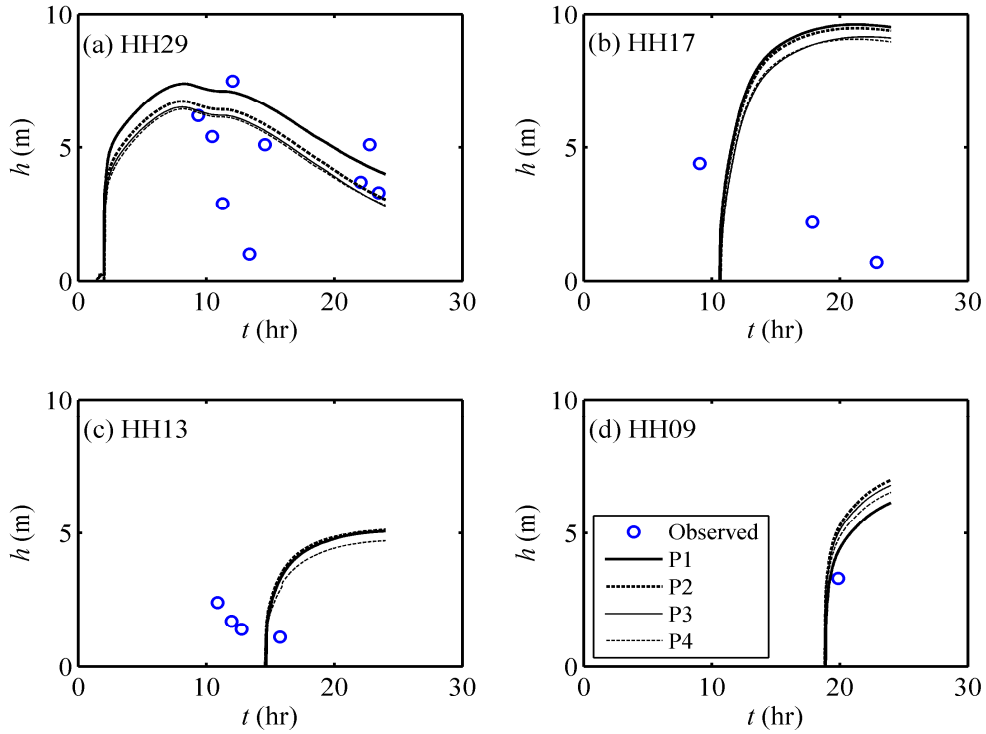

Figure 6. 8 Computed (PF2) and observed time variation of current thickness at four cross sections.

6.1.4 Distributions of current thickness, velocity, concentration and bed deformation

Cross sectional distributions at cross sections (x = 5 km in Figure 6.9 and x = 11 km in Figure 6.10) are examined including (a) current velocity u , (b) current velocity v, (c) bed and current surface elevation and (d) concentration. The data used are from Run ZF1.

First, at both cross sections, the values of u are greater than zero at both cross sections, those of v are below zero at both cross sections. This indicates a southeast direction of the current propagation, consistent with the channel direction (see Figure 6.3). Second, the current surface elevations appear the same across a given cross section (Figs. 6.9c and 6.10c). This indicates that in the implementation of the upstream boundary condition, the assumption of the same current surface position across the channel is reasonable. Third, the maximum of the absolute values of the current velocities are consistently at the central part of the cross sections (Figs. 6.9a, b and 6.10a, b), which are characterized by the lowest bed elevation and thus the maximum current thickness. The current velocities decrease towards the channel bank. This suggests that the assumed linear relationship between the current

thickness and the current velocity is reasonable. This also applies to the relation between the current thickness and the sediment concentration (Figs. 6.9d and 6.10d). Finally, for the four selected times (4 hrs, 8 hrs, 16 hrs and 24 hrs) in Figs. 6.9 and 6.10, the current velocity and sediment concentration decrease with time, and become infinitely small at t = 24 hrs. This is in accordance with the fact that this event dies out before it reaches the dam.

Figs. 6.11-6.13 show the computed (Run ZF1) distributions of the current variables in the whole reservoir at selected times, Figure 6.11 shows the current thickness, Fig 6.12 the sediment concentration and Figure 6.13 the bed deformation depth: $z(x,y,t)-z(x,y,0)$. Figure 6.14 illustrates the distributions of the current velocity at t = 24 hr for x < 15 km. From Figs. 6.11-6.14, the following are observed. When the current front has passed through HH18 (see Figure 6.3), the narrowest cross section, the largest current thickness appears to occur here (Figure 6.11c, d). The appearance of the largest current thickness around HH18 is also described in YRCC (2007). This is because the narrow cross section virtually plays a role of channel constriction. As the current propagates into the downstream reach (Figure 6.11a, b, c), a current front with relatively higher sediment concentration is formed (Figure 6.12a, b, c). The highest sediment concentration occurs always at the current front (Figure 6.12a, b, c), except when the current approaches HH05 (Figure 6.12d), where the current vanishes gradually. When the current front approaches HH05 ($x \approx 35$ km, see Figure 6.3), sediment concentration at the current front decreases (comparing Figure 6.12c and Figure 6.12d). Accordingly, the current advance slows down, progressing only about 2 km from t = 16 hrs to 24 hrs (Figure 6.11c, d and Figure 6.4a). Finally, the current front position becomes stable around HH05, consistent with the field observation (YRCC 2007). This is also reflected by the bed deformation distributions (Figure 6.13). The currents are mainly erosive when $t \leq 8$ hrs and the river bed degrade continuously (Figure 6.13a, b). Then, patchy depositions appear as the current propagates further downstream (t = 16 hrs, Figure 6.13c, d). Also, as can be seen from the current velocity in Figure 6.14, the turbidity current evolution is well resolved.

These observations, along with the good agreement for the current front and sediment transport rate, suggest that turbidity currents in the Xiaolangdi reservoir are well resolved by the fully coupled model using the parameters specified in Case ZF1.

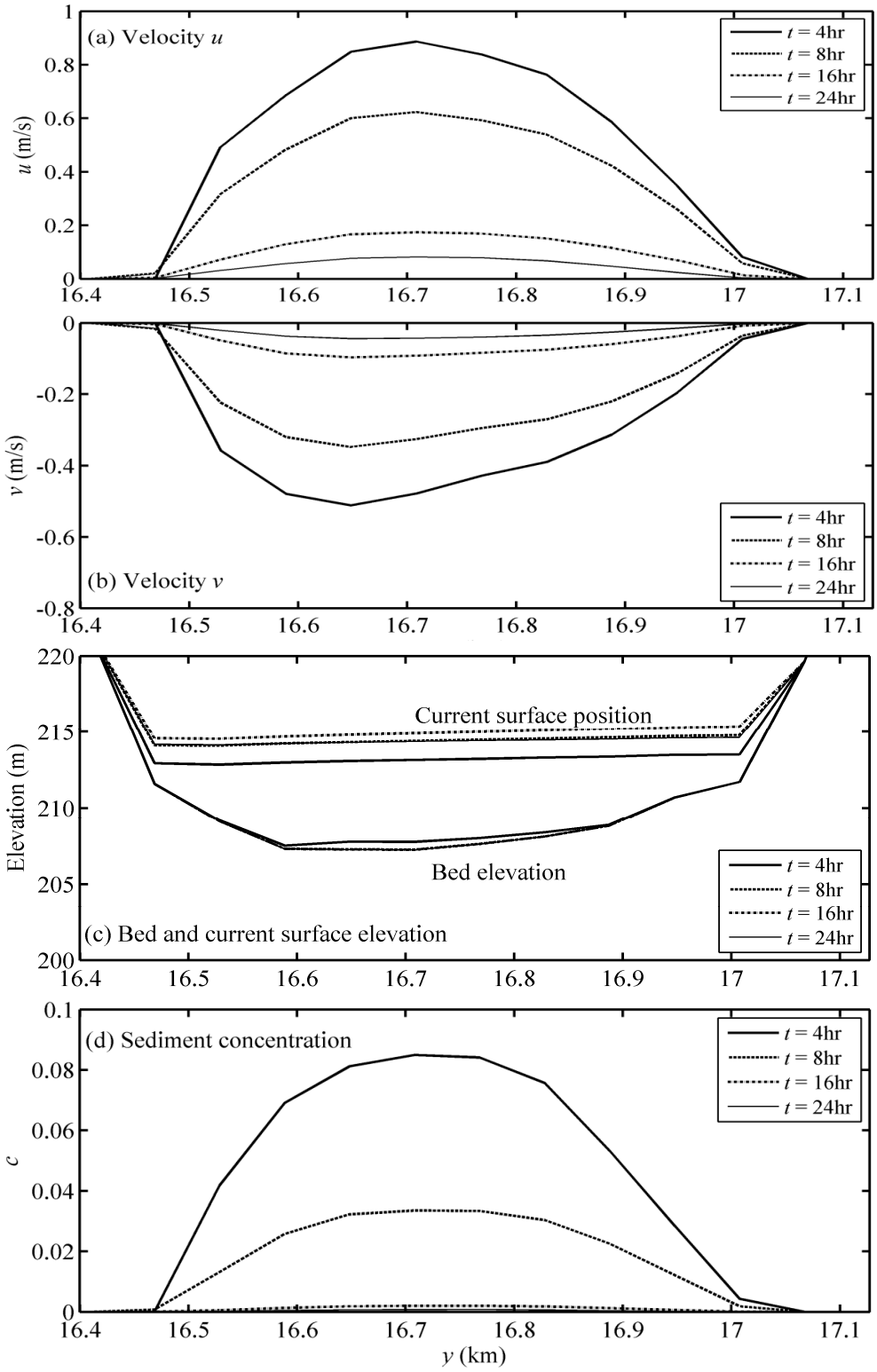

Figure 6. 9 Cross sectional distributions of (a) current velocity u, (b) current velocity v, (c) bed and current surface and (d) sediment concentration at x = 5 km from Run ZF1.

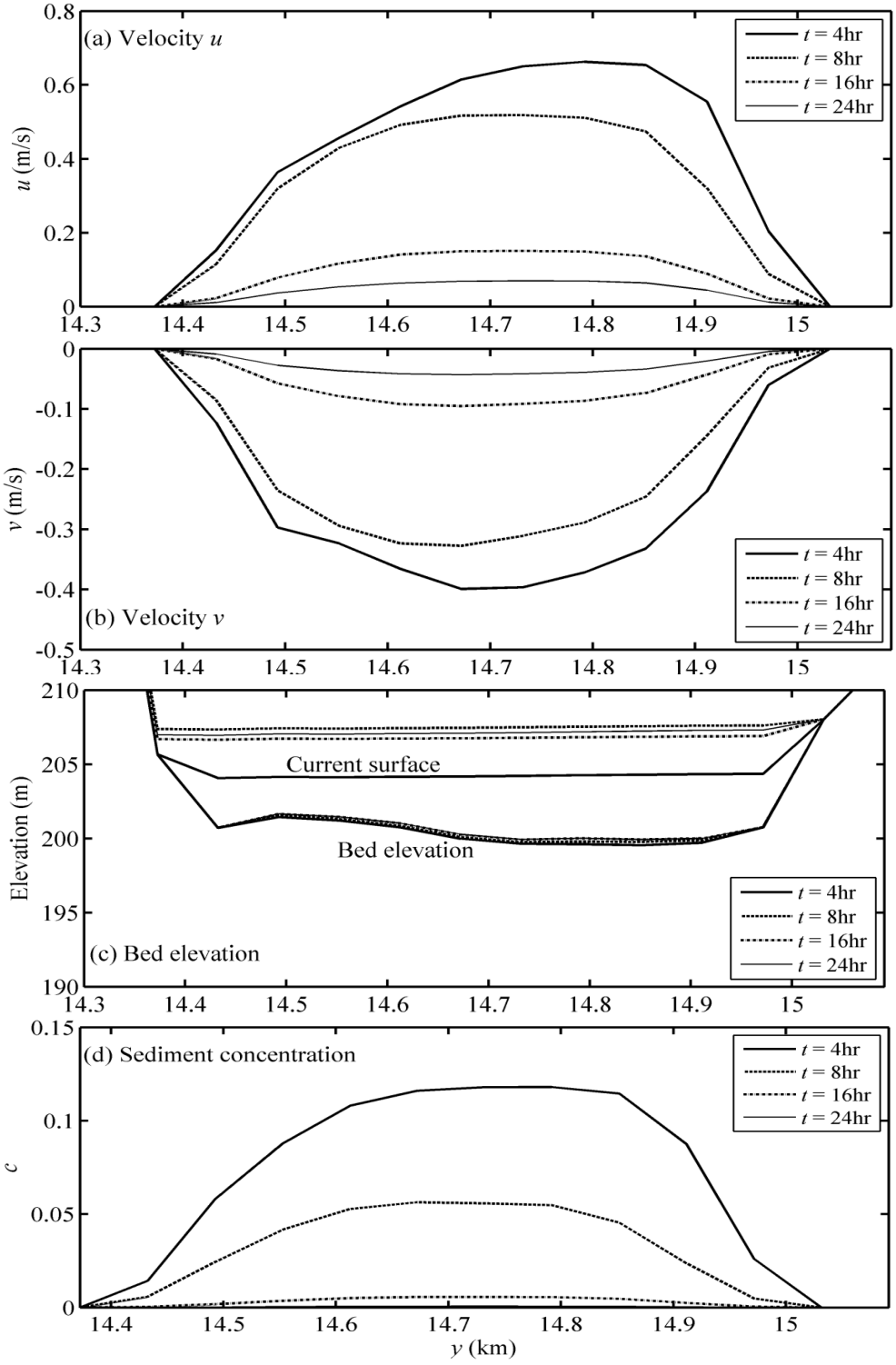

Figure 6. 10 Cross sectional distributions of (a) current velocity u, (b) current velocity v, (c) bed and current surface and (d) sediment concentration at x = 11 km from Run ZF1.

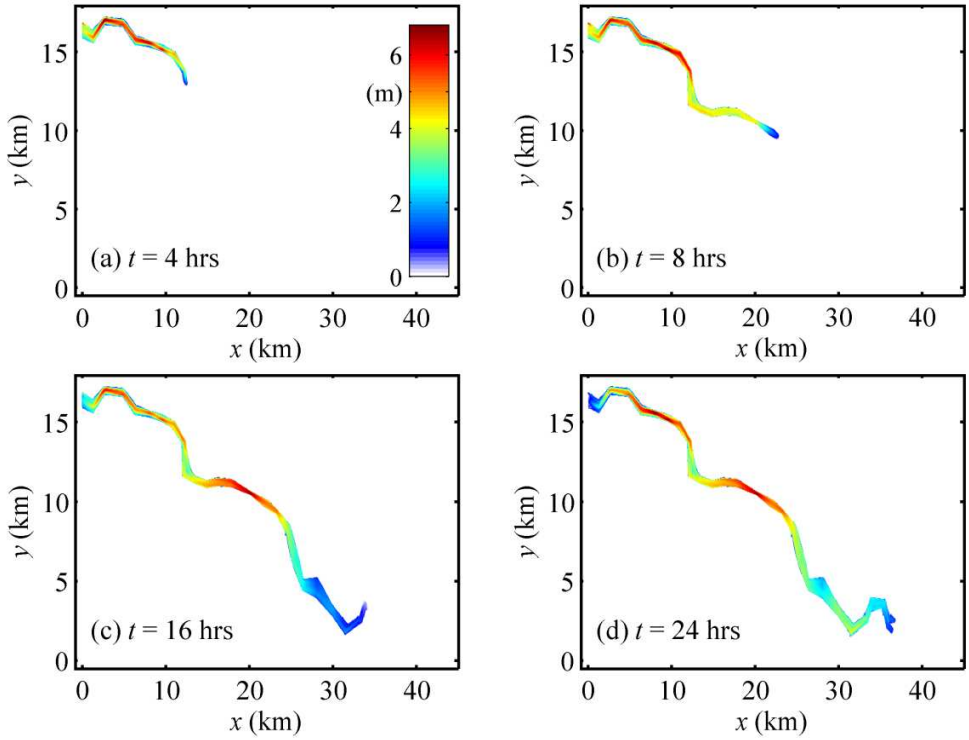

Figure 6. 11 Turbidity current thickness distributions from Run ZF1 at four times.

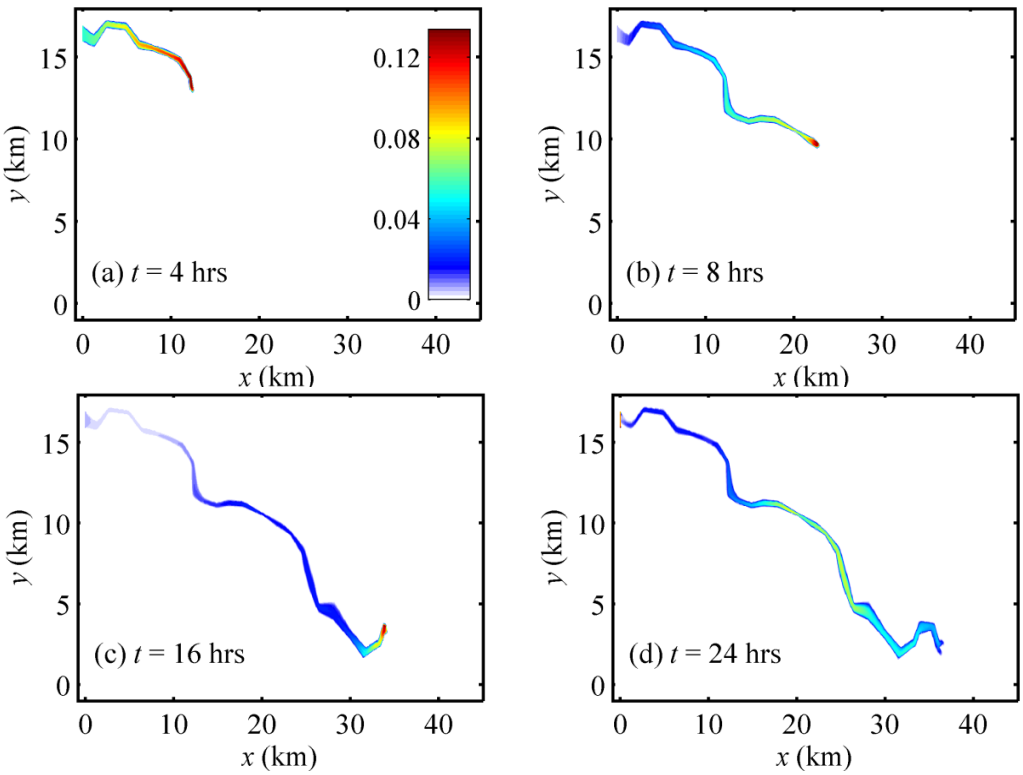

Figure 6. 12 Sediment concentration distributions from Run ZF1 at four times.

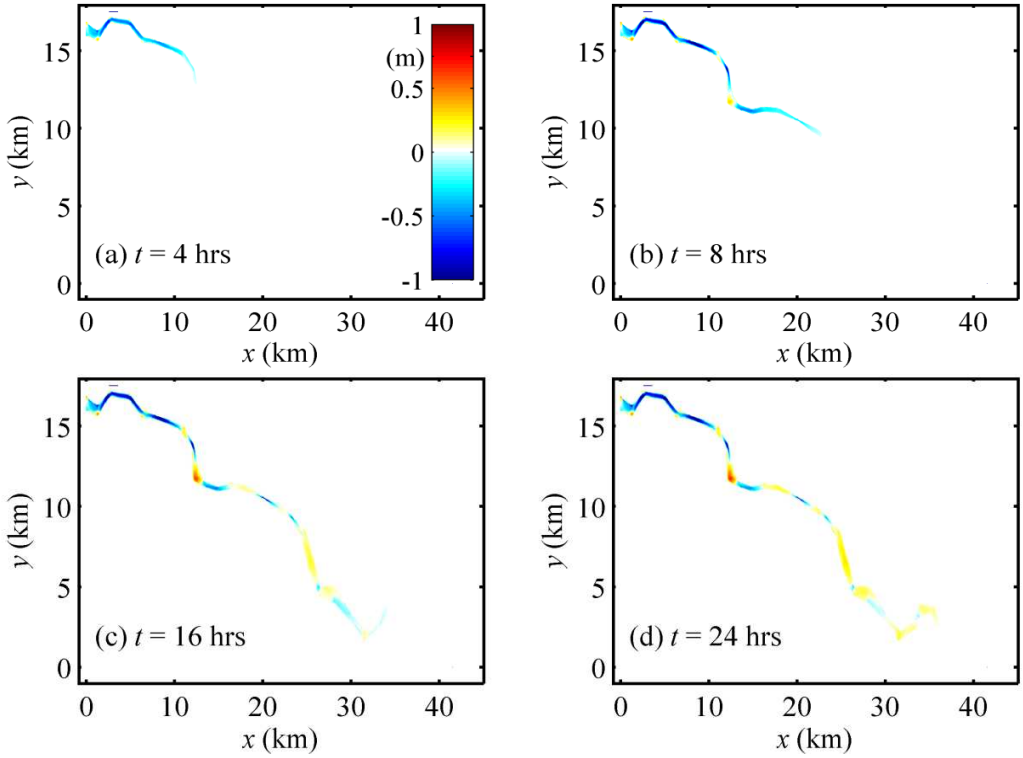

Figure 6. 13 Bed deformation depth distributions from Run ZF1 at four times.

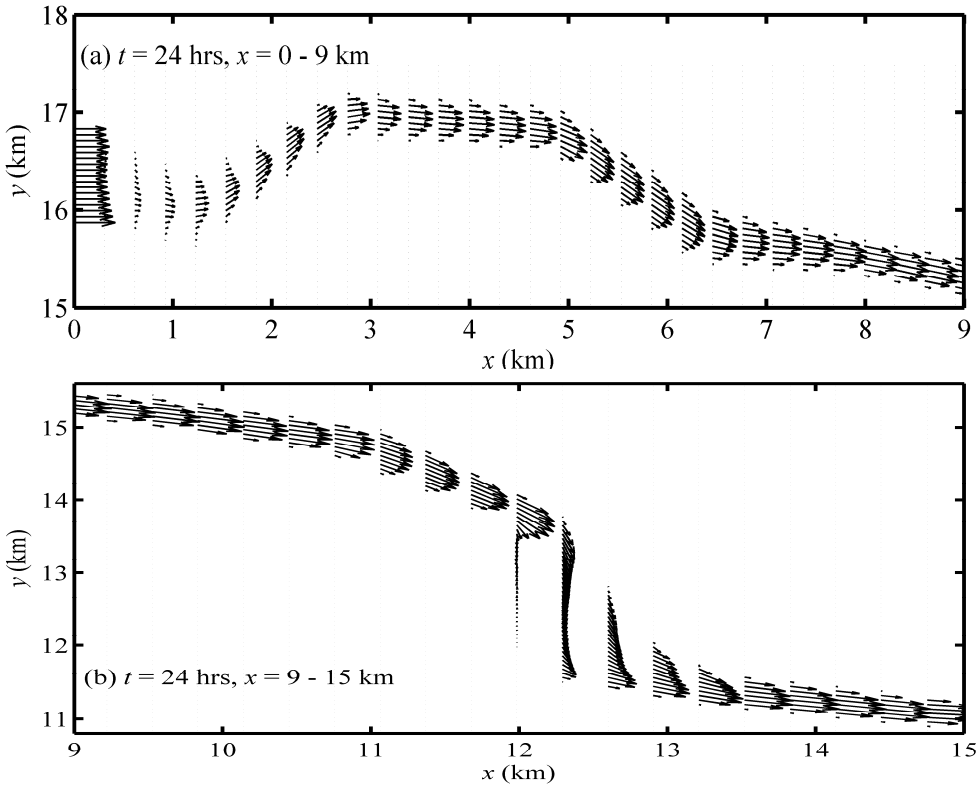

Figure 6. 14 Current velocity distributions from Run ZF1 at t = 24 hr with $x \leq$ 15 m.

6.2.5 Feedback Impacts of Bed Deformation

It is interesting to investigate if the feedback impacts of bed deformation could appreciably affect the evolution of turbidity currents in the Xiaolangdi reservoir. The most important factor, i.e. the current front location against time, is chosen for comparison. Figure 6.15 illustrates the difference in the front location along the x-direction between the FCM and PCM for Run ZF1, showing considerable difference. The positive values denote that the computed current advance by the PCM is faster than that by the FCM. As seen in Figure 6.15, the PCM consistently overestimate the current front propagation speed by about 200 m – 800 m. This reinforces the conclusion that a fully coupled modelling approach should be applied.

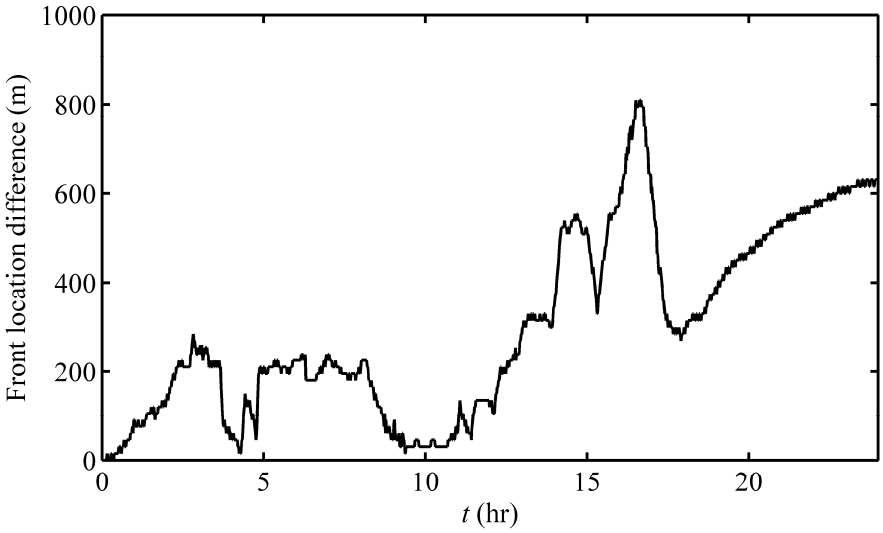

Figure 6. 15 The difference in the front location along the x-direction between the FCM and PCM for Run ZF1. The positive values denote that the computed current advance by the PCM is faster than that by the FCM.

6.2 Modelling the Second Event of Turbidity currents

To further validate the calibrated model (with parameters specified in Run ZF1), the second event is investigated numerically in this section. The second event occurred during the afternoon of 7th July, about one day after the end of the first event. Though indirectly, it has been attributed to water released from the Wanjiazhai reservoir between the 2nd and the 7th July. When this water flow entered the Sanmenxia reservoir and thus increased its water

storage, flow discharge at Sanmenxia rose to approximately 4500 m^3/s, which induced a second sediment-laden flood event and second event of turbidity currents.

Measurements were taken at five cross sections: HH29, HH25, HH17, HH13 and HH09. At each cross section, measurements commenced only when the sediment transport rate had approximately peaked. Figure 6.16 illustrates the observed current thickness, layer-averaged current velocity and sediment concentration, determined by the same procedure as that for the first event. The time t = 0 hr corresponds to 17:00 7th July, about 1 hour before the arrival of the current peak at HH29. The measured data at HH29 is most uniformly distributed over the 48 hours, serving as reliable indication of upstream conditions. Therefore, the computational reach is HH29-HH01.

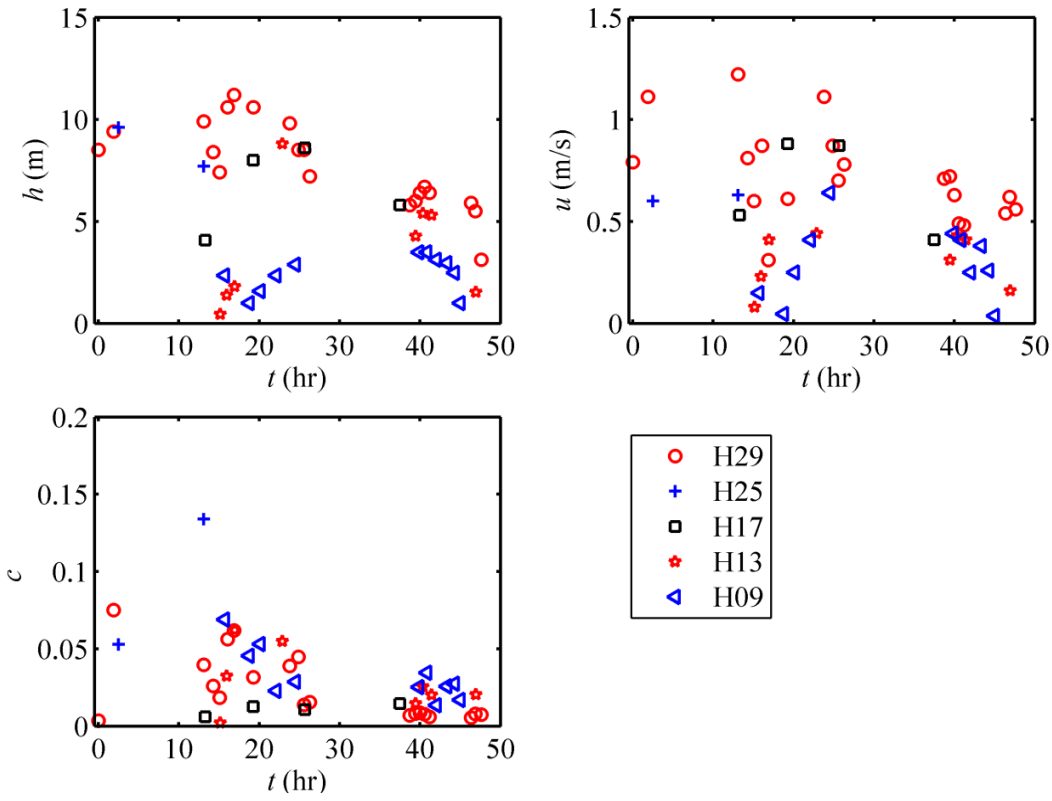

Figure 6. 16 Observations of the second event. t **= 0 hr indicates 16:30 on 7th July.**

The topography surveyed in May 2004 is used as the initial bed topography. The bed morphology resulting from the first event is not used because there was no measurement of bed topography after the first event. Much effort is required in the future to collect

comprehensive field data of turbidity currents and the associated bed morphological changes, so that uncertainties in the mathematical modelling can be reduced to the minimum. The computational time is 48 hours (7th July 17:00 to 9th July 17:00). It is assumed that there is no turbidity current initially on the river bed, because prior to the peak of the current very low sediment concentrations were observed, and the first turbidity currents had almost dissipated when the second turbidity current started. At the downstream boundary the current upper surface level is specified (185 m, see YRCC 2007) if $Ri > 1$ (subcritical current), and free current conditions are specified if $Ri < 1$.

Figure 6.17 shows the location of the current peak in the *x*-direction against time from the computation and the observation. In addition to ψ_z = 50 as in the calibrated model (Run ZF1), three smaller values (ψ_z = 40, 45 and 47) are also applied for comparison. The location of the current peak is approximately *x* = 5 km when *t* = 0 hr. It is because the origin of the coordinate (0, 0) is set at HH32 (see Figure 6.3), which is the same as that for the first event for consistency. It is seen that the calibrated model (ψ_z = 50) slightly overestimates the advance of the current by about 1 hr (Figure 6.17). Within the considered range of ψ_z, it takes the current peak approximately 13-15 hours to arrive at the downstream end, which compares with the observed value of 14.5 hours fairly well.

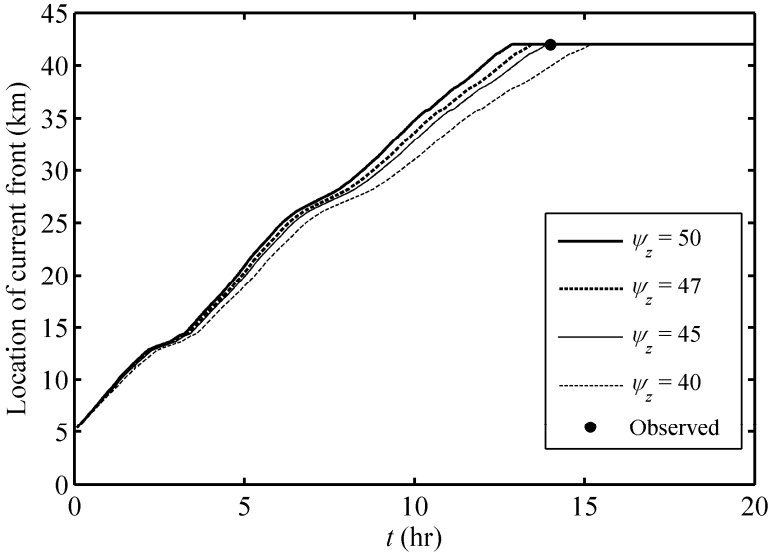

Figure 6. 17 Advance of the current for the second event.

Figure 6.18 shows the computed (from the calibrated model) and observed sediment transport rates. The selection of the four positions (P1, P2, P3 and P4) follows the same procedure as that for the first event. As a first approximation, the computation generally agrees with the observed magnitude and the variation trend of the sediment transport rates at HH25, HH17 and HH13 (Figure 6.18a, b, c), though the number of measured data points is limited at some cross sections (say, only two measured data at HH25). The comparison is rather poor at HH09 (Figure 6.18d). In contrast to the decreasing trend upstream of HH13 (see Figure 6.18a, b, c: 0.4 m^2/s at HH25, 0.3 m^2/s at HH17 and 0.25 m^2/s at HH13), the computed peak transport rate at HH09 attains a value as high as 0.45 m^2/s, whereas the measured maximum discharge at HH09 is below 0.1 m^2/s. This may be attributed to the fact that peak values are not easily captured in the measurements. More likely, this should be ascribed to the detachment of the current from the bed and consequently the current evolves into a turbidity plume at around HH09 (YRCC 2007). However this aspect of behaviour is not the focus of the present work.

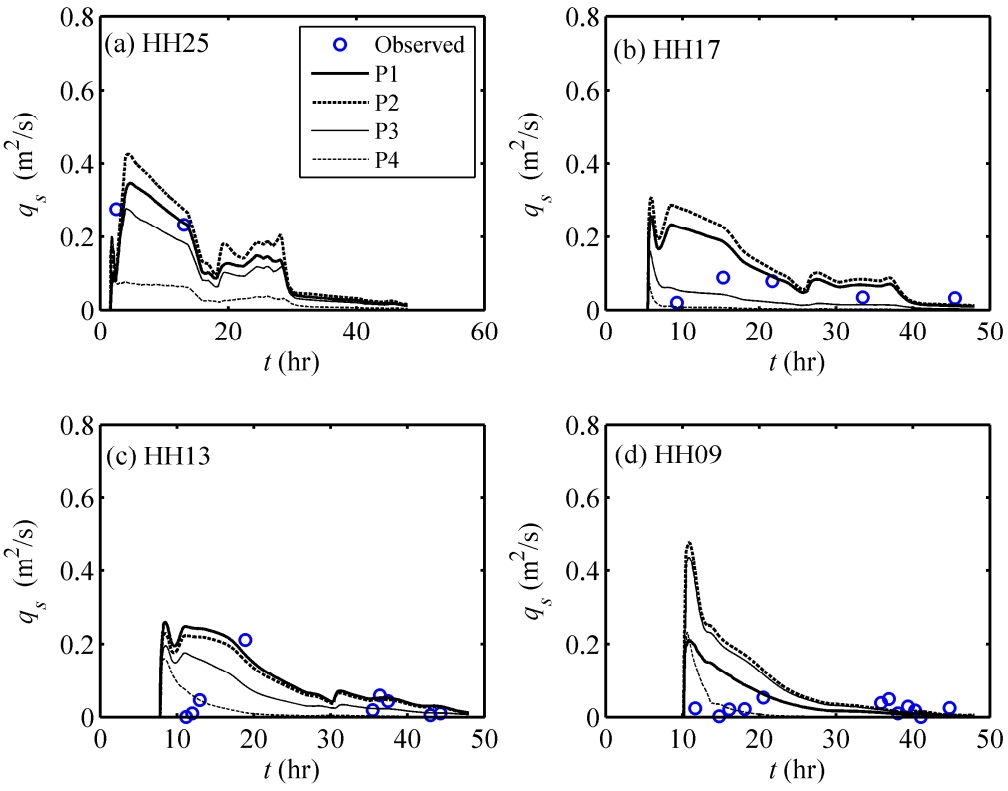

Figure 6. 18 Computed and observed sediment transport rate for the second event.

The reasonable good fit of the advance of the current peak and the sediment transport rate further underpins the ability of the present model to resolve the turbidity currents in the Xiaolangdi reservoir.

6.3 Discussions

One of the main differences for the occurrences of the two events lies in the magnitude (roughly, 2000 m^3/s vs. 4500 m^3/s) and duration (approximately, 24 hrs vs. 48 hrs) of the flood processes before plunging. This fact dictates their contrasting behaviour: the first event dissipated around HH05, whilst the second managed to reach the dam and flush an amount of sediment downstream. Yet, the numerical case studies indicate that there was also the possibility for the first event to flush sediment if there had been sufficient finer sediments for entrainment or less resistance from the bed (Figure 6.4). This leads to a suggestion that the location to generate artificial sediment disturbance (e.g., Li 2004; YRCC 2007; Sequeiros *et al*. 2009a) might be preferably selected at places rich in fine sediment, and if possible feeding fine sediment to the currents at the upstream might also be a good strategy. The present work has created a useful tool for effective sediment and reservoir management by turbidity currents in alluvial rivers.

Chapter 7. CONCLUSIONS, PERSPECTIVES AND FUTURE WORKS

7.1 Conclusions

Based on simplified governing equations, existing mathematical models of turbidity currents are mostly partially coupled or decoupled, ignoring partly or completely the interactions between the turbidity current, sediment transport, bed topography and deformation. Uncertainties arising from those simplified mathematical models remain unclear. This study aims to achieve an improved understanding of the effects of these interactions on turbidity current development and morphological changes. A fully coupled model, which incorporates explicitly the interactions, is developed, tested and applied to turbidity currents in two typical environments. The multiple-time-scale theory is developed for turbidity currents, by which the feedback impacts of bed deformation and the significance of fully coupled modelling are investigated theoretically. The theoretical analysis is further complemented by numerical comparisons of the fully coupled model with previous simplified mathematical models. The following conclusions are obtained.

Fully coupled modelling is critical for refined quality of turbidity current modelling, especially for those cases featuring active sediment transport and rapid bed deformation. The fully coupled modelling approach induces only marginal increase in computational cost, as compared to previous decoupled or partially coupled models. For erosional turbidity currents, partially coupled models may overestimate the sediment concentration, the current velocity, the speed of current front propagation, and underestimate the current thickness. In contrast, the sediment concentration, the current velocity, the speed of current front propagation may be underestimated and the current thickness overestimated for depositional turbidity currents, if a partially coupled model is used.

The performance of the fully coupled model is demonstrated against a series of idealized and experimental turbidity currents. The well-balanced property and accordingly the applicability to irregular topographies are demonstrated through successful numerical

simulation for an initially static turbidity current over an irregular hump. The reasonable agreement between the experimental data of turbidity currents with an internal hydraulic jump and the numerical results indicates the ability of the model to capture automatically shock waves. The computed current front location and bed deformation depth agree well with the experimental data, suggesting a high accuracy. Nevertheless, quantitative uncertainty is inevitable as empirical parameters and relationships are involved in the model. For different applications, the values of empirical parameters need to be calibrated.

The incipient formation processes of submarine morphological features, including canyons, channel-levees and lobes by turbidity currents, are resolved by the fully coupled model. It is shown that appropriate bed slope and sediment particle size may favour the formation of submarine channel-levee morphology, as larger Richardson number does. This facilitates an improved understanding of the formation of submarine morphological features by turbidity currents.

Two events of turbidity currents in the Xiaolangdi Reservoir are investigated numerically, which demonstrate that with appropriate estimates of boundary resistance and bed sediment entrainment, the turbidity current in Xiaolangdi reservoir can be fairly well resolved by the fully coupled model. The advance of turbidity currents and the sediment transport rate are reproduced rather well when compared against field observations. The fully coupled model provides a useful tool for effective sediment and reservoir management by turbidity currents in alluvial rivers.

7.2 Perspectives and future works

The present layer-averaged modelling approach is in general viable for turbidity currents, which features a sensible balance between theoretical rigour and applicability. Depth-resolving modelling approach is useful to obtain the vertical current and sediment structure, which might be necessary under certain circumstances. Yet the applicability of the depth-resolving approach is currently limited to small-scale turbidity currents with mild morphological changes and weak sediment transport in laboratories, because large-scale events may feature rapid morphological evolution, and the computing cost may be

prohibitively high. The main theoretical limitation of vertical 2D and full 3D models arise from the poorly understood physics of turbulence, as modified by sediment transport. Further research on the interaction of turbulence and sediment transport is required to improve credibility of vertical 2D and full 3D models. Many other theories, such as the kinetic theory by Wang, Ni and their collaborators (Wang and Ni 1990; Zhong *et al*. 2011) and the Smoothed particle hydrodynamics (Violeau 2012), have been used in sediment-laden open channel flow modelling, yet applications are rarely reported for turbidity current modelling. It will be interesting to extend these theories to turbidity currents in the future. Comparisons of different mathematical models will always be useful as the number of mathematical models for turbidity currents continue to increase rapidly.

Field observations and laboratory experiments will continue to improve understanding of turbidity currents. Much effort will be required to develop more reliable underwater sampling techniques so that complete measurements of turbidity currents are more achievable. Presently, laboratory experiments on turbidity currents mostly focus on steady inflow conditions. Experiments with unsteady inflow conditions warrant investigation. These are also critical for the calibration and validation of mathematical modelling of turbidity currents.

The sediment entrainment flux and resistance are shown to be the two key factors determining the turbidity current evolution and morphological changes. The quantification of resistance applied to turbidity currents has been commonly approximated by a constant bed drag coefficient, which may give rise to uncertainty to an unknown extent. There has been only one group of empirical relations for the quantification of sediment entrainment flux by turbidity currents [Parker *et al.* (1987) and its variants]. Fundamentally, the mechanism of sediment entrainment by turbulent flow has so far remained poorly understood, even for open channel sediment-laden flows. Systematic experimental and theoretical studies of the mechanism and quantification of sediment entrainment and bed resistance are warranted.

Current thickness is one of the most important physical variables for turbidity currents, yet its determination is subject to much uncertainty. It is because the upper interface of turbidity currents are usually unclear. Different methods using threshold sediment

concentration, threshold current velocity, vertical integrals of density or velocity, have been used to define the upper interface and the current thickness. It will be useful to compare the effects of these difference methods on the obtained current thickness.

In this study, uniform sediment transport by turbidity currents is considered. Further extension of the present work to graded sediment transport will be essential because heterogeneous sediment transport is much more typical in the field (Paola *et al*. 1992).

The plunging process by which sediment-laden open channel flow becomes turbidity currents is not accounted for in the present model. It would be useful to pursue an integrated modelling approach connecting the turbidity current and the open channel flow.

Only suspended sediment transport by turbidity currents is considered in the present work, and it will be useful to include bed load in future studies (Sequeiros *et al*. 2010b)

REFERENCES

Adduce, C., Sciortino, G., and Proietti, S. (2011). "Gravity currents produced by lock exchanges: experiments and simulations with a two layer shallow water model with entrainment." *Journal of Hydraulic Engineering*, ASCE, DOI: 10.1061/(ASCE)HY.1943-7900.0000484.

Alavian, V., Jirka, G., Denton, R., Johnson, M., and Stefan, H. (1992). "Density currents entering lakes and reservoirs." *Journal of Hydraulic Engineering*, ASCE, 118(11), 1464-1489.

Alexander, J., Mclelland, S., Gray, T., Vincent, C., Leeder, M., and Ellett, S. (2008). "Laboratory sustained turbidity currents form elongate ridges at channel mouths." *Sedimentology*, 55, 845-868.

Alexander, J., and Morris, S. (1994). "Observations on experimental, nonchannelized, high-concentration turbidity currents and variations in deposits around obstacles." *Journal of Sedimentary Research*, 64(4), 899-909.

Alexander, J., and Mulder, T. (2002). "Experimental quasi-steady density currents." *Marine Geology*, 186, 195-210.

Allen, J. (1991). "The bouma division a and the possible duration of turbidity currents." *Journal of Sedimentary Research, SEPM*, 61(2), 291-295.

Altinakar, M., Graf, W., and Hopfinger, E. (1990). "Weakly depositing turbidity current on a small slope." *Journal of Hydraulic Research*, IAHR, 28(1), 55-80.

Altinakar, M., Graf, W., and Hopfinger, E. (1996). "Flow structure of turbidity currents." *Journal of Hydraulic Research*, IAHR, 34(5), 713-718.

Amy, L., Hogg, A., Peakall, J., and Talling, P. (2005a), Abrupt transitions in gravity currents, *Journal of Geophysical Research*, AGU, 110(F03001), 1-19.

Amy, L., and Talling, P. (2006). "Anatomy of turbidites and linked debrites based on long distance (120*30 km) bed correlation, Marnoso-Arenacea formation, northern Appennines, Italy." *Sedimentology*, 53, 161-212.

Amy, L., Talling, T., Peakall, J., Wynn, R., and Arzola Thynne, R. (2005b). "Bed geometry used to test recognition criteria of turbidites and (sandy) debrites." *Sedimentary Geology*, 179, 163-174.

Aureli, F., Maranzoni, A., Mignosa, P., and Ziveri, C. (2008). "A weighted surface-depth gradient method for the numerical integration of the 2D shallow water equations with topography." *Advances in Water Resources*, Elsevier, 31, 962-974.

Baas, J., McCaffrey, W. D., Haughton, P. D. W., and Choux, C. (2005). "Coupling between suspended sediment distribution and turbulence structure in a laboratory turbidity current." *Journal of Geophysical Research-Oceans*, 110(C11), DOI: 10.1029/2004JC002668.

Baas, J., van Kesteren, W., and Postma, G. (2004). "Deposits of depletive high-density turbidity currents: a flume analogue of bed geometry, structure and texture." *Sedimentology*, 51, 1053-1088.

Bermudez, A., and Vazquez, M. E. (1994). “Upwind methods for hyperbolic conservation laws with source terms.” Computers & Fluids, 23(8), 1049-1071.

Birman, V., Meiburg, E., and Kneller, B. (2009). The shape of submarine levees: exponential or power law? *Journal of Fluid Mechanics*, 619, 367-376.

Blanchette, F., Strauss, M., Meiburg, E., Kneller, B., and Glinsky, M. (2005). "High-resolution numerical simulations of resuspending gravity currents: conditions for self-sustainment." *Journal of Geophysical Research*, 110(C12022), DOI: 10.1029/2005JC002927.

Bonnecaze, R., Hallworth, M., Huppert, H., and Lister, J. (1995), Axisymmetric particle-driven gravity currents, *Journal of Fluid Mechanics*, 294, pp. 93-121.

Bonnecaze, R., Huppert, H., and Lister, J. (1993), Particle-driven gravity currents, *Journal of Fluid Mechanics*, 250, pp. 339-369.

Bowen, A. J., Normark, W. R., and Piper, D. J. W. (1984). "Modelling of turbidity currents on Navy submarine fan, California continental borderland." *Sedimentology*, 31, 169-185.

Bradford, S., and Katopodes, N. (1999a). Hydrodynamics of turbid underflows. I: Formulation and numerical analysis. *Journal of Hydraulic Engineering*, ASCE,

125(10), 1016-1028.

Bradford, S., and Katopodes, N. (1999b). Hydrodynamics of turbid underflows. II: Aggradation, avulsion, and channelization. *Journal of Hydraulic Engineering*, ASCE, 125(10), 1016-1028.

Bradford, S., Katopodes, N., and Parker, G. (1997). "Characteristic analysis of turbid underflows." *Journal of Hydraulic Engineering*, ASCE, 123(5), 420-431.

Brunt, R. L., McCaffrey, W. D., and Kneller, B. C. (2004). "Experimental modelling of the spatial distribution of grain size developed in a fill-and-spill mini-basin setting." *Journal of Sedimentary Research*, SEPM, 74(3), 438-446.

Cantelli, A., Pirmez, C., Johnson, S., and Parker, G. (2011). "Morphodynamic and stratigraphic evolution of self-channelized subaqueous fans emplaced by turbidity currents." *Journal of Sedimentary Research*, SEPM, 81(3), 233-247.

Cantero, M., Balachandar, S., and Garcia, M. (2007). "On the front velocity of gravity currents." *Journal of Fluid Mechanics*, 586, 1-39.

Cao, Z., Egashira, S., Carling, P.A. 2003. "Role of suspended-sediment particle size in modifying velocity profiles in open channel flows." *Water Resources Research*, AGU, 39(2), DOI: 10.1029/2001WR000934.

Cao, Z., Hu, P., and Pender, G. (2010). "Reconciled bedload sediment transport rates in ephemeral and perennial rivers." *Earth Surface Processes and Landforms*, 35(14), 1655-1665.

Cao, Z., Hu, P., and Pender, G. (2011). "Multiple time scales of fluvial processes with bed load sediment and implications for mathematical modelling." *Journal of Hydraulic Engineering*, ASCE, 137(3), 267-276.

Cao, Z., Li, Y., and Yue, Z. (2007). "Multiple time scales of alluvial rivers carrying suspended sediment and their implications for mathematical modelling." *Advances in Water Resources*, 30(4), 715-729.

Cao, Z., Pender, G., and Carling, P. (2006). "Shallow water hydrodynamic models for hyperconcentrated sediment-laden floods over erodible bed." *Advances in Water Resources*, 29, 546-557.

Choi, S. (1998). Layer-averaged modelling of two-dimensional turbidity currents with a

dissipative-Galerkin finite element method. Part I: Formulation and application example. *Journal of Hydraulic Research*, IAHR, 36(3), 339-362.

Choi, S. 1999. "Layer-averaged modelling of two-dimensional turbidity currents with a dissipative-Galerkin finite element method. II: sensitivity analysis and experimental verification." *Journal of Hydraulic Research*, IAHR, 37(2), 257-271.

Choi, S., and Garcia, M. (2002a)."Modelling of one dimensional turbidity currents with a dissipative-Galerkin finite element method." *Journal of Hydraulic Research*, 33(5), 623-648.

Choi, S., and Garcia, M. (2002b). "k-e turbulence modelling of density currents developing two dimensionally on a slope." *Journal of Hydraulic Engineering*, ASCE, 128(1), 55-63.

Choux, C., Baas, J., McCaffrey, W. D., and Haughton, P. D. W. (2005). "Comparison of spatio-temporal evolution of experimental particulate gravity flows at two different initial concentrations, based on velocity, grain size and density data." *Sedimentary Geology*, 179(1-2), 49-69.

Chowdhury, M., Testik, F. (2010). "Laboratory testing of mathematical models for high-concentration fluid mud turbidity currents." *Ocean Engineering*, DOI: 10.1016/j.oceaneng.2010.10.020.

Cofaigh, C., Dowdeswell, J., and Kenyon, N. (2006). Geophysical investigations of a high latitude submarine channel system and associated channel-mouth lobe in the Lofoten Basin, Polar North Atlantic. *Marine Geology*, 226, 41-50.

Cossu, R., and Wells, M. G. (2010). "Coriolis forces influence the secondary circulation of gravity currents flowing in large scale sinuous submarine channel systems." *Geophysical Research Letters*, 37(L17603), DOI: 10.1029/2010GL044296.

Cossu, R., and Wells, M. G. (2011). "A comparison of the shear stress distribution in the bottom boundary layer of experimental density and turbidity currents." *European Journal of Mechanics B/Fluids*, DOI: 10.1016/j.euromechflu.2011.09.006.

Cossu, R., Wells, M. G., and Wahlin, A. K. (2010). "Influence of the Coriolis force on the velocity structure of gravity currents in straight submarine channel systems." *Journal of Geophysical Research*, 115(C11016), DOI: 10.1029/2010JC006208.

Cunge, J., Holly, F., Jr., and Verwey, A. (1980). *Practical aspects of computational river*

hydraulics, Pitman, London.

Dade, W. and Huppert, H. (1995), Runout and fine-sediment deposits of axisymmetric gravity currents, *Journal of Geophysical Research*, AGU, 100(C9), pp. 18597-18609.

De Cesare, G., Boillat, J., and Schleiss, A. (2006). "Circulation in stratified lakes due to flood-induced turbidity currents." *Journal of Hydraulic Engineering*, ASCE, 132(11), 1508-1517.

De Cesare, G., Schleiss, A., and Hermann, F. (2001). "Impact of turbidity currents on reservoir sedimentation." *Journal of Hydraulic Engineering*, ASCE, 127(1), 6-16.

De Rooij, F., and Dalziel, S. B. (2001). "Time and space-resolved measurements of deposition under turbidity currents." *Spec. Publs. int. Ass. Sediment*, 31, 207-215.

Dykstra, M., and Kneller, B. C. (2008). "Lateral accretion in a deep-marine channel complex: implications for channellized flow processes in turbidity currents." *Sedimentology*, 56(5), 1411-1432.

Eggenhuisen, J., and McCaffrey, W. D. (2011). "The vertical turbulence structure of experimental turbidity currents encountering basal obstructions: implications for vertical suspended sediment distribution in non-equilibrium currents." *Sedimentology*, DOI: 10.1111/j.1365-3091.2011.01297.x.

Eidsvik, K.J., Brors, B. 1989. "Self-accelerated turbidity current prediction based upon $k-\varepsilon$ turbulence." *Continental Shelf Research*, 9, 617-627.

Fan, J. (1986). "Turbid density currents in reservoirs." *Water International*, 11(3), 107-116.

Fan, J., and Morris, G. (1992a). "Reservoir sedimentation. I: Delta and density currents deposits." *Journal of Hydraulic Engineering*, ASCE, 118(3), 354-369.

Fan, J., and Morris, G. (1992b). "Reservoir sedimentation. II: Reservoir desiltation and long-term storage capacity." *Journal of Hydraulic Engineering*, ASCE, 118(3), 370-384.

Farrell, G.J., Stefan, H.G. (1988). "Mathematical modelling of plunging reservoir flows." *Journal of Hydraulic Research*, IAHR, 26(5), 525-537.

Fasolato, G., Ronco, P., and Di Silvio, G. (2009). How fast and how far do variable boundary conditions affect river morphodynamics. *Journal of Hydraulic Research*,

IAHR, 47(3), 329-339.

Felix, M. (2002). “Flow structure of turbidity currents.” *Sedimentology*, 49, 397-419.

Felix, M., Sturton, S., and Peakall, J. (2005). "Combined measurements of velocity and concentration in experimental turbidity currents." *Sedimentary Geology*, 179, 31-47.

Fildani, A., Normark, W., Kostic, S., and Parker, G. (2006). Channel formation by flow stripping: large-scale scour features along the Monterey East Channel and their relation to sediment waves. *Sedimentology*, 53(6), 1265-1287.

Firoozabadi, B., Afshin, H., and Aram, E. (2009). "Three-dimensional modelling of density current in a straight channel." *Journal of Hydraulic Engineering*, ASCE, 135(5), 393-402.

Fukushima, Y., Parker, G., and Pantin H. (1985). Prediction of ignitive turbidity currents in Scripps Submarine Canyon. *Marine Geology*, 67, 55-81.

Garcia, M. (1992). "Turbidity currents." In *Encyclopedia of Earth System Science*, Academic Press, San Diego, Calif., 399-408.

Garcia, M. (1993). Hydraulic jumps in sediment-driven bottom currents. *Journal of Hydraulic Engineering*, ASCE, 119(10), 1094-1117.

Garcia, M. (1994). "Depositional turbidity currents laden with poorly sorted sediment." *Journal of Hydraulic Engineering*, ASCE, 120(11), 1240-1263.

Garcia, M., and Parker, G. (1989). Experiments on hydraulic jumps in turbidity currents near a canyon-fan transition. *Science*, 245, 393-396.

Garcia, M., and Parker, G. (1993). "Experiments on the entrainment of sediment into suspension by a dense bottom current." *Journal of Geophysical Research*, 98(C3), 4793-4807.

Gladstone, C., and Pritchard, D. (2010). "Patterns of deposition from experimental turbidity currents with reversing buoyancy." *Sedimentology*, 57, 53-84.

Gladstone, C., and Woods, A. (2000). "On the application of box models to particle-driven gravity currents." *Journal of Fluid Mechanics*, 416, 187-195.

Gonzalez-Castro, J.A., Muste, M. 2007. "Framework for estimating uncertainty of ADCP measurements from a moving boat by standardized uncertainty analysis." *Journal of Hydraulic Engineering*, ASCE, 133(12), 1390-1410.

Gray, T. E., Alexander, J., and Leeder, M. R. (2005). "Quantifying velocity and turbulence

structure in depositing sustained turbidity currents across breaks in slope." *Sedimentology*, 52, 467-488.

Guo, J. (2002). "Logarithmic matching and its application in computational hydraulics and sediment transport." *Journal of Hydraulic Research*, IAHR, 40(5), 555-565.

Hall, B., Meiburg, E., and Kneller, B. (2008). Channel formation by turbidity currents: Navier-Stokes-based linear stability analysis. *Journal of Fluid Mechanics*, 615, 185-210.

Hallworth, M. and Huppert, H. (1998). Abrupt transitions in high-concentration, particle-driven gravity currents. *Physics of Fluid*, 10(5), 1083-1087.

Hallworth, M., Phillips, J., Huppert, H., and Sparks, S. (1993). "Entrainment in turbulent gravity currents." *Nature*, 362, 829-831.

Han, Q.W., Xiang, X.L. 1981. "Sediment transport characteristics of turbidity currents." *People's Yangtze River*, 4, 76-81. (in Chinese).

Hiscott, R. N., Hall, F. R., and Pirmez, C. (1997). "Turbidity current overspill from the Amazon channel: texture of the silt/sand load, paleoflow from anisotropy of magnetic susceptibility and implications for flow processes." *Proceedings of the Ocean Drilling Program, Scientific Results*, 155, 53-78.

Huang, H., Imran, J., and Pirmez, C. (2005). "Numerical model of turbidity currents with a deforming bottom boundary." *Journal of Hydraulic Engineering*, ASCE, 131(4), 283-293.

Huang, H., Imran, J., and Pirmez, C. (2007). "Numerical modelling of poorly sorted depositional turbidity currents." *Journal of Geophysical Research*, 112(C01014), DOI: 10.1029/2006JC003778.

Huang, H., Imran, J., and Pirmez, C. (2008). "Numerical study of turbidity currents with sudden-release and sustained-inflow mechanisms." *Journal of Hydraulic Engineering*, ASCE, 134(9), 1199-1209.

Hubbard, M., and Garcia-Navarro, P. (2000). "Flux difference splitting and the balancing of source terms and flux gradients." *Journal of Computational Physics*, 165(1), 89-125.

Huppert, H. (1998). "Quantitative modelling of granular suspension flows." *Phil. Trans. R. Soc. Lond. A.*, 356, 2471-2496.

Huppert, H. (2006), "Gravity currents: a personal perspective." *Journal of Fluid Mechanics*, 554, pp. 299-322.

Huppert, H. and Simpson, J. (1980), The slumping of gravity currents, *Journal of Fluid Mechanics*, 99, pp. 785-799.

Imran, J., Parker, G., and Harff, P. (2002). Experiments on incipient channelization of submarine fans. *Journal of Hydraulic Research*, IAHR, 40(1), 21-32.

Imran, J., Parker, G., and Katopodes, N. (1998). A numerical model of channel inception on submarine fans. *Journal of Geophysical Research*, AGU, 103(C1), 1219-1238.

Inman, D. L., Nordstorm, C. E., and Flick, R. E. (1976). Currents in submarine canyons: an air-sea-land interaction. *Annual Review of Fluid Mechanics*, 8, 275-310.

Izumi, N. (2004). "The formation of submarine gullies by turbidity currents." *Journal of Geophysical Research*, 109(C03048), DOI: 10.1029/2003JC001898.

Jamieson, E.C., Rennie, C.D., Jacobson, R.B., Townsend, R.D. 2011. "Evaluation of ADCP apparent bed load velocity in a large sand-bed river: moving versus stationary boat conditions." *Journal of Hydraulic Engineering*, ASCE, 137(9), 1064-1071.

Kane, I. A., Dykstra, M., Kneller, B. C., Tremblay, S., and McCaffrey, W. D. (2009). "Architecture of a coarse-grained channel-levee system: the Rosario Formation, Baja California, Mexico." *Sedimentology*, 56(7), 2207-2234.

Kane, I. A., Kneller, B., Dykstra, M., Kassem, A., and McCaffrey, W. D. (2007). Anatomy of a submarine channel-levee: An example from Upper Cretaceous slope sediments, Rosario Formation, Baja California, Mexico. *Marine and Petroleum*, 24, 540-563.

Kane, I. A., McCaffrey, W. D., and Peakall, J. (2008). "Controls on sinuosity evolution within submarine channels." *Geology*, 36(4), 287-290.

Kane, I. A., McCaffrey, W. D., Peakall, J., and Kneller, B. C. (2010). "Submarine channel levee shape and sediment waves from physical experiments." *Sedimentary Geology*, 223, 75-85.

Keevil, G. M., Peakall, J., Best, J. L., and Amos, K. J. (2006). "Flow structure in sinuous submarine channels: velocity and turbulence structure of an experimental submarine channel." *Marine Geology*, 229, 241-257.

Keevil, G. M., Peakall, J., and Best, J. L. (2007). "The influence of scale, slope and channel

geometry on the flow dynamics of submarine channels." *Marine and Petroleum Geology*, 24, 487-503.

Khan, S. M., and Imran, J. (2008). "Numerical investigation of turbidity currents flowing through minibasins on the Continental slope." *Journal of Sedimentary Research*, SEPM, 78(4), 245-257.

Khripounoff, A., Vangriesheim, A., Babonneau, N., Crassous, P., Dennielou, B., and Savoye, B. (2003). Direct observation of intense turbidity current activity in the Zaire submarine valley at 4000 m water depth. *Marine Geology*, 194, 151-158.

Kneller, B. C., Bennett, S. J., and McCaffrey, W. D. (1997). "Velocity and turbulence structure of density currents and internal solitary waves: potential sediment transport and the formation of wave ripples in deep water." *Sedimentary Geology*, 112(3-4), 235-250.

Kneller, B. C., Bennett, S. J., and McCaffrey, W. D. (1999). "Velocity structure, turbulence and fluid stresses in experimental gravity currents." *Journal of Geophysical Research-Oceans*, 104(C3), 5381-5391.

Kneller, B. C., and Buckee, C. (2000). "The structure and fluid mechanics of turbidity currents: a review of some recent studies and their geological implications." *Sedimentology*, 47, 62-94.

Kneller, B. C., Edwards, D., McCaffrey, W., and Moore, R. (1991). "Oblique reflection of turbidity currents." *Geology*, 19(3), 250-252.

Kneller, B. C., and McCaffrey, W. D. (1999). "Depositional effects of flow nonuniformity and stratification within turbidity currents approaching a bounding slope: deflection, reflection, and facies variation." *Journal of Sedimentary Research*, SEPM, 69(5), 980-991.

Kneller, B. C., and McCaffrey, W. D. (2003). "The interpretation of vertical sequences in turbidite beds: the influence of longitudinal flow structure." *Journal of Sedimentary Research*, SEPM, 73(5), 706-713.

Komar, P. D. (1969). "The channelized flow of turbidity currents with application to Monterey deep-sea fan channel." *Journal of Geophysical Research*, 74(18), 4544-4558.

Komar, P. D. (1971). "Hydraulic jumps in turbidity currents." *Geological Society of America Bulletin*, 82(6), 1477-1488.

Kostic, S., and Parker, G. (2003a). "Progradational sand-mud deltas in lakes and reservoirs. I: Theory and numerical modelling." *Journal of Hydraulic Research*, IAHR, 41(2), 127-140.

Kostic, S., and Parker, G. (2003b). "Progradational sand-mud deltas in lakes and reservoirs. II: Experiment and numerical simulation." *Journal of Hydraulic Research*, IAHR, 41(2), 141-152.

Kostic, S., and Parker, G. (2006). The response of turbidity currents to a canyon-fan transition: internal hydraulic jumps and depositional signatures. *Journal of Hydraulic Research*, IAHR, 44(5), 631-653.

Kostic, S., and Parker, G. (2007). Conditions under which a supercritical turbidity current traverses an abrupt transition to vanishing bed slope without a hydraulic jump. *Journal of Fluid Mechanics*, 586, 119-145.

Kostic, S., Parker, G., and Marr, J. (2002). "Role of turbidity currents in setting the foreset slope of Clinoforms prograding into standing fresh water." *Journal of Sedimentary Research*, SEPM, 72(3), 353-362.

Kubo, Y., and Nakajima, T. (2002). "Laboratory experiments and numerical simulation of sediment wave formation by turbidity currents." *Marine Geology*, 192, 102-121.

Lamb, M., Hickson, T., Marr, J., Sheets, B., Paola, C., and Parker, G. (2004). "Surging versus continuous turbidity currents: flow dynamics and deposits in an experimental intraslope minibasin." *Journal of Sedimentary Research*, SEPM, 74, 148-155.

Lamb, M., Myrow, P. M., Lukens, C., Houck, K., and Strauss, J. (2008). "Deposits from wave-influenced turbidity currents: Pennsylvanian minturn formation, Colorado, U.S.A." *Journal of Sedimentary Research*, SEPM, 78(7), 480-498.

Lamb, M., Toniolo, H., and Parker, G. (2006). "Trapping of sustained turbidity currents by intraslope minibasins." *Sedimentology*, 53, 147-160.

Lee, H., and Yu, W. (1997). "Experimental study of reservoir turbidity current." *Journal of Hydraulic Engineering*, ASCE, 123(6), 520-528.

Li, G. Y. (2004). "The third test of water and sediment regulation conducted on the Yellow River." *Yellow River*, 26(10), 1-8. (in Chinese).

Li., S. X., Zhang, J. H., Chen, S. K., and Ma, H. B. (2006). "Formation of density current by means of reasonable operation of reservoir in Xiaolangdi project". *Journal of Hydraulic Engineering*, 37(5), 567-572. (in Chinese).

Liang, Q. H., Marche, F. (2009). "Numerical resolution of well-balanced shallow water equations with complex source terms." *Advances in Water Resources*, 32, 873-884.

Lowe, D. (1982). "Sediment gravity flows. II: depositional models with special reference to the deposits of high-density turbidity currents." *Journal of Sedimentary Research*, SEPM, 52(1), 279-297.

Lu, H., Raupach, M. R., and Richards, K. S. (2005). "Modelling entrainment of sedimentary particles by wind and water: a generalized approach." *Journal of Geophysical Research*, 110(D24114), DOI: 10.1029/2005JD006418.

Mahdinia, M., Firoozabadi, B., Farshchi, M., Varnamkhasti, A. G., and Afshin, H. (2011). "Large eddy simulation of lock-exchange flow in a curved channel." *Journal of Hydraulic Engineering*, ASCE, DOI: 10.1061/(ASCE)HY.1943-7900.0000482.

McCaffrey, W. D., Choux, C. M., Baas, J. H., and Haughton, P. D. W. (2003). "Spatio-temporal evolution of velocity structure, concentration and grain size stratification within experimental particulate gravity currents." *Marine and Petroleum Geology*, 20(6-8), 851-860.

McCave, I., and Jones, K. (1988). "Deposition of ungraded muds from high-density non-turbulent turbidity currents." *Nature*, 333, 250-252.

Meiburg, E., and Kneller, B. (2010). "Turbidity currents and their deposits." *Annual Review of Fluid Mechanics*, 42, 135-156.

Middleton, G. V. (1966). "Small-scale models of turbidity currents and the criterion for auto-suspension." *Journal of Sedimentary Research, SEPM*, 36(1), 202-208.

Middleton, G. V. (1993). "Sediment deposition from turbidity currents." *Annual Review of Earth and Planetary Sciences*, 21, 89-114.

Mulder, T., Alexander, J. (2001). "Abrupt change in slope causes variation in the deposit thickness of concentrated particle-driven density currents." *Marine Geology*, 175, 221-235.

Mulder, T., and Cochonat, P. (1996). "Classification of offshore mass movements." *Journal of Sedimentary Research*, SEPM, 66(1), 43-57.

Mulder, T., and Syvitsski, J. P. M. (1995). "Turbidity currents generated at river mouths during exceptional discharges to the world oceans." *Journal of Geology*, 103(3), 285-299.

Mulder, T., Syvitsski, J. P. M., Migeon, S., Faugeres, J., and Savoye, B. (2003). Marine Hyperpycnal flows: initiation, behavior and related deposits. A review. *Marine and Petroleum Geology*, 20, 861-882.

Mulder, T., Syvitsski, J. P. M., and Skene, K. I. (1998). "Modelling of erosion and deposition by turbidity currents generated by river mouths." *Journal of Sedimentary Research*, SEPM, 68(1), 124-137.

Nakajima, T., and Satoh, M. (2001). "The formation of large mudwaves by turbidity currents on the levees of the Toyama deep-sea channel, Japan sea." *Sedimentology*, 48, 435-463.

Nakajima, T., Satoh, M., and Okamura, Y. (1998). "Channel-levee complexes, terminal deep-sea fan and sediment wave fields associated with the Toyama deep-sea channel system in the Japan sea." *Marine Geology*, 147, 25-41.

Necker, F., Hartel, C., Kleiser, L., and Meiburg, E. (2002). High-resolution simulations of particle-driven gravity currents. *International Journal of Multiphase Flow*, 28, 279-300.

Necker, F., Hartel, C., Kleiser, L., and Meiburg, E. (2005). "Mixing and dissipation in particle-driven gravity currents." *Journal of Fluid Mechanics*, 545, 339-372.

Nokes, R., Davidson, M., Stepien, C., Veale, W., and Oliver, R. (2008). "The front condition for intrusive gravity currents." *Journal of Hydraulic Research*, IAHR, 46(6), 788-801.

Normark, W. R. (1999). "Late Pleistocene channel-levee development on Monterey submarine fan, central California." *Geo-Marine Letters*, 18, 179-188.

Nourmohammadi, Z., Afshin, H., and Firoozabadi, B. (2011). "Experimental observation of the flow structure of turbidity currents." *Journal of Hydraulic Research*, IAHR, 49(2), 168-177.

Oehy, C. D., and Schleiss, A. J. (2007). "Control of turbidity currents in reservoirs by solid and permeable obstacles." *Journal of Hydraulic Engineering*, ASCE, 133(6), 637-648.

Paola, C., Parker, G., Seal, R., Sinha, S. K., Southard, J. B., and Wilcock, P. R. (1992). “Downstream fining by selective deposition in a laboratory flume.” *Science*, 258(5089), 1757-1760.

Parker, G., Fukushima, Y., and Pantin, H. M. (1986). Self-accelerating turbidity currents.

Journal of Fluid Mechanics, 171, 145-181.

Parker, G., Garcia, M., Fukushima, Y., and Yu, W. (1987). "Experiments on turbidity currents over an erodible bed." *Journal of Hydraulic Research*, IAHR, 25(1), 123-147.

Parker, G., and Toniolo, H. (2007). "Note on the analysis of plunging of density flows." *Journal of Hydraulic Engineering*, ASCE, 133(6), 690-694.

Parsons, J., Friedrichs, C., Traykovski, P., Mohrig, D., Imran, J., Syvitski, J., Parker, G., Puig P., Buttles, J., and Garcia, M. (2007). "The mechanics of marine sediment gravity flows." *From Continental Margin Sedimentation: from sediment transport to sequence stratigrap*hy. Wiley.

Peakall, J., Amos, K. J., Keevil, G. M., Bradbury, P. W., and Gupta, S. (2007). "Flow processes and sedimentation in submarine channel bends." *Marine Petroleum Geology*, 24, 470-486.

Piper, D., Cochonat, P., and Morrison, M. L. (1999). "The sequence of events around the epicentre of the 1929 Grand Banks earthquake: initiation of the debris flow and turbidity current inferred from side scan sonar." *Sedimentology*, 46, 79-97.

Piper, D., Cochonat, P., Ollier, G., Ledrezen, E., Morrison, M., and Baltzer, A. (1992). "Noncatastrophic evolution of a turbidity current from a slump-evidence from the 1929 Grand-banks earthquake."

Pirmez, C., and Imran, J. (2003). Reconstruction of turbidity currents in Amazon Channel. *Marine and Petroleum Geology*, 20, 823-849.

Pratson, L, Imran, J., Hutton, W., Parker, G., and Syvitski, J. (2001). "BANG1D: a one-dimensional, lagrangian model of subaqueous turbid surges." *Computers & Geosciences*, 27(6), 701-716.

Qian, N. and Wan, Z. (1983), *Mechanics of sediment transport*, Beijing: Science Press, China.

Qu, S., Han, Q., Sun, Z., and Wang, D. (2006). "Analysis on the regulation mode of density current in the initial operation peried of Xiaolangdi Reservoir." *Journal of Sediment Research*, 6, 24-29. (in Chinese).

Rogers, B. D., Borthwick, A. G. L., and Taylor, P. H. (2001). “Adaptive Q-tree Godunov-type scheme for shallow water equations.” *International Journal for Numerical Methods in Fluids*, 35, 247-280.

Rogers, B. D., Borthwick, A. G. L., and Taylor, P. H. (2003). "Mathematical balancing of flux gradient and source terms prior to using Roe's approximate Riemann solver." *Journal of Computational Physics*, 192, 422-451.

Rosatti, G., and Fraccarollo, L. (2006). "A well-balanced approach for flows over mobile bed with high sediment transport." *Journal of Computational Physics*, 220, 312-338.

Rowland, J., Hilley, G., Fildani, A. (2010). "A test of initiation of submarine leveed channels by deposition alone." *Journal of Sedimentary Research*, SEPM, 80(8), 710-727.

Salles, T., Lopez, S., Cacas, M., and Mulder, T. (2007). "Cellular automata model of density currents." *Geomorphology*, 88, 1-20.

Sangster, T., Friedrich, H., and Strachan, L. J. (2010). "Evolution of unconfined turbidity current deposits: an experimental study." *The 17th Australasian Fluid Mechanics Conference*, Auckland, New Zealand, 5-9 December 2010.

Sequeiros, O., Cantero, M. I., and Garcia, M. (2009a). Sediment management by jets and turbidity currents with application to a reservoir for flood and pollution control in Chicago, Illinois. *Journal of Hydraulic Research*, IAHR, 47(3), 340-348.

Sequeiros, O., Cantero, M., Viparelli, E., White, J., Garcia, M., and Parker, G. (2009b). "Modelling turbidity currents with nonuniform sediment and reverse buoyancy." *Water Resources Research*, 45(W06408), DOI: 10.1029/2008WR007422.

Sequeiros, O., Naruse, H., Endo, N., Garcia, M., Parker, G. (2009c). "Experimental study on self-accelerating turbidity currents." *Journal of Geophysical Research*, AGU, 114(C05025), DOI: 10.1029/2008JC005149.

Sequeiros, O., Spinewine, B., Beaubouef, R., Sun, T., Garcia, M., Parker, G. (2010a). "Characteristics of velocity and excess density profiles of saline underflows and turbidity currents flowing over a mobile bed." *Journal of Hydraulic Engineering*, ASCE, 136(7), 412-433.

Sequeiros, O., Spinewine, B., Beaubouef, R., Sun, T., Garcia, M., Parker, G. (2010b). "Bedload transport and bed resistance associated with density and turbidity currents." *Sedimentology*, 57(6), 1463-1490.

Serrano-Pacheco, A., Murillo, J., and Garcia-Navarro, P. (2009). "A finite volume method for the simulation of the waves generated by landslides." *Journal of Hydrology*, 373(3-4), 273-289.

Shanmugam, G. (1996). "High-density turbidity currents: are they sandy debris flows?" *Journal of Sedimentary Research,* SEPM, 66(1), 2-10.

Shanmugam, G. (2002). "Ten turbidite myths." *Earth-Science Reviews,* 58, 311-341.

Simpson, J. E. (1997). *Gravity currents in the environment and laboratory*. Cambridge University Press, Cambridge, England.

Skene, K. I., & Piper, D. J. W. (2006). Late cenozoic evolution of Laurentian Fan: development of a glacially-fed submarine fan. *Marine Geology*, 227, 67-92.

Skene, K. I., Piper, D. J. W., and Hill, P. S. (2002). Quantitative analysis of variations in depositional sequence thickness from submarine channel levees. *Sedimentology,* 49, 1411-1430.

Stow, D. A. V., Hernandez-Molina, F. J., LIave, E., Sayago-Gil, M., Diaz del Rio, V., and Branson, A. (2009). "Bedform-velocity matrix: the estimation of bottom current velocity from bedform observations." *Geology*, 37(4), 327-330.

Straub, K., and Mohrig, D. (2008). "Quantifying the morphology and growth of levees in aggrading submarine channels." *Journal of Geophysical Research,* 113(F03012), DOI: 10.1029/2007JF000896.

Straub, K., Mohrig, D., Buttles, J., McElroy, B., and Pirmez, C. (2011). "Quantifying the influence of channel sinuosity on the depositional mechanics of channelized turbidity currents: a laboratory study." *Marine and Petroleum Geology*, 28(3), 744-760.

Straub, K., Mohrig, D., McElroy, B., Buttles, J., and Pirmez, C. (2008). "Interactions between turbidity currents and topography in aggrading sinuous submarine channels: a laboratory study." *Geological Society of America Bulletin*, 120, 368-385.

Talling, P., Wynn, R., Masson, D., Frenz, M., Cronin, B., Schiebel, R., Akhmetzhanov, A., Dallmeier-Tiessen, S., Benetti, S., Weaver, P., Georgiopoulou, A., Zuhlsdorff, C., and Amy, A. (2007). "Onset of submarine debris flow deposition far from original giant landslide." *Nature*, 450(22), 541-544.

Toniolo, H. (2009). "Numerical simulation of sedimentation processes in reservoirs as a function of outlet location." *International Journal of Sediment Research*, 24, 339-351.

Toniolo, H., Harff, P., Marr, J., Paola, C., and Parker, G. (2004). "Experiments on reworking by successive unconfined subaqueous and subaerial muddy debris flows." *Journal*

of Hydraulic Engineering, ASCE, 130(1), 38-48.

Toniolo, H., Lamb, M., and Parker, G. (2006a). "Depositional turbidity currents in diapiric minibasins on the continental slope: formulation and theory." *Journal of Sedimentary Research*, SEPM, 76(5), 783-797.

Toniolo, H., Parker, G., and Voller, V. (2007). "Role of ponded turbidity currents in reservoir trap efficiency." *Journal of Hydraulic Engineering*, ASCE, 133(6), 579-595.

Toniolo, H., Parker, G., Voller, V., and Beaubouef, R. (2006b). "Depositional turbidity currents in diapiric minibasins on the continental slope: experiments-numerical simulation and upscaling." *Journal of Sedimentary Research*, SEPM, 76(5), 798-818.

Toro, E. (2001). *Shock-Capturing Methods for Free-Surface Shallow Flows*. Wiley, Chichester, England.

Toro, E., Hidalgo, A., and Dumbser, M. (2009). "FORCE schemes on unstructured meshes I: conservative hyperbolic systems." *Journal of Computational Physics*, 228, 3368-3389.

Violeau, D. (2012). *Fluid Mechanics and the SPH method: theory and applications*. Oxford University Press, USA.

Violet, J., Sheets, B., Pratson, L., Paola, C., Beaubouef, R., and Parker, G. (2005). "Experiment on turbidity currents and their deposits in a model 3D subsiding minibasin." *Journal of Sedimentary Research*, SEPM, 75(5), 820-843.

Wang, G. Q., and Ni, J. R. (1990). “Kinetic theory for particle concentration distribution in two-phase flow.” *Journal of Engineering Mechanics*, 116(2), http://dx.doi.org/10.1061/(ASCE)0733-9399(1990)116:12(2738).

Weimer, P., and Link, M. H. (1991). "Global petroleum occurrences in submarine fans and turbidite system." In Seismic facies and sedimentary process of submarine fans and turbidite systems. Springer-Verlag, New York, 9-67.

Weirich, F. (1988). "Field evidence for hydraulic jumps in subaqueous sediment gravity flows." *Nature*, 332(4), 626-629.

Wright, L. D., Wiseman, W. J., Bornhold, B. D., Prior, D. B., Suhayda, J. N., Keller, G. H., Yang, L. S., and Fan, Y. B. (1988). "Marine dispersal and deposition of Yellow River silts by gravity-driven underflows." *Nature*, 332, 629-632.

Wu, W. M. (2007). *Computational River Dynamics*. Taylor & Francis, Leiden, The Netherlands.

Wynn, R., Masson, D., Stow, D., and Weaver, P. (2000). "Turbidity current sediment waves on the submarine slopes of the western Canary islands." *Marine Geology*, 163, 185-198.

Wynn, R., and Stow, D. (2002). "Recognition and interpretation of deep-water sediment waves: implications for palaeoceanography, hydrocarbon exploration and flow process interpretation." *Marine Geology*, 192, 1-3.

Xu, J. P. (2010). "Normalized velocity profiles of field measured turbidity currents." *Geology*, 38(6), 563-566.

Xu, J. P., Noble, M. A., and Rosenfeld, L. K. (2004). "In-situ measurements of velocity structure within turbidity currents." *Geophysical Research Letters*, 31(L09311), DOI: 10.1029/2004GL019718.

Xu, J. P., Dong, M., Li, X., and Hu, Y. (2007). "Analysis on density current in Xiaolangdi reservoir area occurred during a regulated discharge regime of the Yellow River in 2006" *Yellow River*, 29(6), 17-20. (in Chinese).

Yam, K., McCaffrey, W. D., Ingham, D. B., and Burns, A. (2011). "CFD modelling of selected laboratory turbidity currents." *Journal of Hydraulic Research*, IAHR, 49(5), 657-666.

Yellow River Conservancy Commission (YRCC). (2007). *The third test of water and sediment regulation conducted on the Yellow River*. Yellow River Conservancy Press, Zhengzhou, China. (in Chinese).

Yu, W., Lee, H., Hsu, S. (2000). "Experiments on deposition behavior of fine sediment in a reservoir." *Journal of Hydraulic Engineering*, ASCE, 126(12), 912-920.

Zeng, J., and Lowe, D. (1997a). "Numerical simulation of turbidity current flow and sedimentation. I: theory." *Sedimentology*, 44, 67-84..

Zeng, J., and Lowe, D. (1997b). "Numerical simulation of turbidity current flow and sedimentation. II: results and geological applications." *Sedimentology*, 44, 85-104.

Zhang, R., and Xie, J. (1993). *Sedimentation Research in China – systematic selections.* China Water and Power Press, Beijing.

Zhao, D. H., Shen, H. W., Tabios III, G. Q., Lai, J. S., and Tan, W. Y. (1994). "Finite-volume two-dimensional unsteady-flow model for river basins." *Journal of*

Hydraulic Engineering, ASCE, 120(7), 863-883.

Zhong, D.Y., Wang, G. Q., and Ding, Y. (2011). “Bed sediment entrainment function based on kinetic theory.” *Journal of Hydraulic Engineering*, 137(2), 222-233.

Zhou, J., Causon, D., Mingham, C., and Ingram, D. (2001). "The surface gradient method for the treatment of source terms in the shallow water equations." *Journal of Computational physics*, 168, 1-25.